# Challenges of Offshore LNG Transfer

vorgelegt von
Diplom-Ingenieur Florian Sprenger
aus Berlin

von der Fakultät V — Verkehrs- und Maschinensysteme
der Technischen Universität Berlin
zur Erlangung des akademischen Grades

Doktor der Ingenieurwissenschaften
– Dr.-Ing. –

genehmigte Dissertation

Promotionsausschuss:

| | |
|---|---|
| Vorsitzender: | Prof. Dr.-Ing. Andrés Cura Hochbaum |
| Berichter: | Prof. Dr.-Ing. Günther F. Clauss |
| Berichter: | Prof. Dr.-Ing. Paul Uwe Thamsen |

Tag der wissenschaftlichen Aussprache: 05.12.2012

Berlin 2012

D 83

# Acknowledgement

This thesis was inspired by my research work for the project *MPLS20 – Maritime Pipe Loading System 20"* at the Ocean Engineering Division of Technical University of Berlin. I wish to express my gratitude to all the people that encouraged me to work on this topic and supported me over the last years.

First of all, I would like to thank Prof. Dr.-Ing. Günther Clauss for his excellent technical and personal support. With his enthusiasm, experience in ocean engineering and faith in me he always provided pathbreaking advice, valuable motivation and great freedom for my research work. Many thanks also to my second promoter Prof. Dr.-Ing. Paul Uwe Thamsen who took time and interest in my work despite his immense work load as vice president of the Technical University of Berlin as well as to the chairman of the doctorial committee, Prof. Dr.-Ing. Andrés Cura Hochbaum.

I would like to thank my colleagues from the Ocean Engineering Division, namely Daniel Testa, Matthias Dudek and Marco Klein, for a uniquely cooperative, pleasant and entertaining working atmosphere. Special thanks go to my friend, room mate and research partner Sascha Kosleck, who was always receptive for working related as well as private issues and who shared creative, productive, stressful and relaxing phases with me during the last six years. During my time in the team, Kornelia Tietze was always a cheerful and irreplaceable support for all the administrative issues — I am greatly indebted to her. From the technical staff that built and equipped the ship models, I would like to thank namely Manfred Berndt and Haiko de Vries. Special thanks of course also to the team of graduate assistants for their persistent and reliable support during the model testing series.

Since I would not have been able to work on this exciting topic without the funding of the research project MPLS20, I want to express my gratitude to the German Federal Ministry of Economics and Technology and also to Project Management Jülich. Furthermore, I want to thank the involved project partners IMPaC Offshore Engineering, Nexans Deutschland and Brugg Pipe Systems for their support.

But I owe the greatest debt of gratitude to my beloved wife Miriam, who encouraged me and supported me with patience and sympathy through the entire working process of this thesis. I appreciate the energy she committed

to compensate my mental and physical absence in the daily family life with our two wonderful daughters Paula and Mia. Last but not least I would like to thank my parents Lieselotte and Bernhard Sprenger who always stood behind me and believed in me.

Florian Sprenger

Berlin, Dezember 2012

# Abstract

Developing maritime gas fields in deep water by *Floating Liquefied Natural Gas* (FLNG) concepts poses demanding technical challenges. So far, no systems are in operation but projects in the design or construction phase are characterized by a floating terminal barge that produces, liquefies and stores natural gas at the offshore location. Frequently operating shuttle tankers are moored either alongside (side-by-side) or at the stern of the terminal (tandem) to receive the cryogenic liquefied cargo.

During the offloading procedure, which takes 18 to 24 hours in changing environmental conditions, the transfer system has to tolerate the occurring relative motions between the terminal and the tanker. Gradually changing filling levels and free surface effects inside the tanks significantly influence the seakeeping behavior of the LNG carrier.

Methods and research results published so far encompass experimental and numerical analyses of individual aspects of the complex hydrodynamic problem related to offshore LNG transfer. Well known work includes the determination of pressure peaks on tank walls caused by violent sloshing or exemplary reproductions of coupling effects between resonant internal fluid motions and wave-induced vessel motions. However, available results are mostly based on idealized conditions (two-dimensional setups, model testing with fresh water instead of LNG) where relevant hydrodynamic effects are observed to some extend but their consequences on the extrapolation of data to full scale operations is not fully comprehended. Due to these restrictions, most of the results obtained by current standard approaches are defective or at least incomplete.

In this thesis, the first validated holistic numerical method, which captures all hydrodynamic aspects that are relevant during offloading operations is presented. By in-depth studies on the basis of this approach, the background of the occurring phenomena can be fully comprehended, which allows accurate extrapolation of results from model scale to full scale. Combining the introduced method and the gained background knowledge is a critical prerequisite for the conduction of trustworthy feasibility studies and the determination of operational ranges for FLNG projects. The selected linear potential theory based procedure is capable to excellently reproduce seakeeping characteristics as well as internal fluid motions. The entire cal-

culation process is exemplarily demonstrated for the MPLS20 system in the *Haltenbanken* region.

By detailed numerical investigations, it is revealed for the first time that the differences between natural tank modes and sloshing-related maximum values in the respective motion response amplitude operators (RAO) are attributed to the ratio of rigid body mass to added mass. Here, hydrodynamic coupling of different degrees of freedom are a crucial factor. The most important consequence from this finding is that — in contrast to the well-established practice — results obtained from model tests with fresh water filling inside the tanks cannot be extrapolated to full scale operations with LNG.

Comprehensive three-dimensional analyses reveal for the first time that for LNG carriers, significant fluid sloshing and body motions occur perpendicular to the direction of excitation. This phenomenon is caused by asymmetries of the submerged hull geometry as well as asymmetric mass distribution. This observation leads to the conclusion that commonly published idealized two-dimensional approaches are inadequate for the prediction of the motion behavior of vessels with partially filled tanks.

# Kurzfassung

Die Erschließung maritimer Gaslagerstätten in großen Wassertiefen durch sogenannte *Floating Liquefied Natural Gas* (FLNG) Konzepte stellt eine anspruchsvolle technische Herausforderung dar. Derzeit sind noch keine derartigen Systeme in Betrieb, verschiedene in der Planungs- oder Bauphase befindliche Projekte zeichnen sich jedoch stets durch eine schwimmende Terminalbarge aus, die das Gas von der Lagerstätte fördert, verflüssigt und zwischenspeichert. Regelmäßig verkehrende Flüssiggastanker machen entweder längsseits (side-by-side) oder am Heck des Terminals (tandem) fest und übernehmen das tiefkalte, verflüssigte Gas.

Während dieser 18 bis 24 Stunden dauernden Verladeprozedur muss das Transfersystem den aus den vorherrschenden Umweltbedingungen resultierenden Relativbewegungen zwischen Terminal und Tanker standhalten. Insbesondere das Bewegungsverhalten des Tankers wird hierbei durch die sich kontinuierlich ändernden Füllstände und freien Flüssigkeitsoberflächen in den Ladetanks signifikant beeinflusst.

Bisher veröffentlichte Forschungsergebnisse und Methoden umfassen die experimentelle und numerische Analyse von Teilaspekten der komplexen hydrodynamischen Gesamtproblematik einer Offshore LNG-Verladeprozedur, z.B. die Ermittlung von Druckspitzen auf Tankwände durch Sloshing-Effekte oder die exemplarische Reproduktion von Kopplungseffekten zwischen resonanten Fluidbewegungen in den Ladetanks und den seegangsinduzierten Schiffsbewegungen. Hierbei werden jedoch stets idealisierte Bedingungen angenommen (zweidimensionale Betrachtungen, Modellversuche mit Wasser anstelle von LNG) und relevante hydrodynamische Phänomene zwar teilweise beobachtet, ohne jedoch deren Einfluss auf die Extrapolation von Ergebnissen auf die Großausführung vollständig zu verstehen. Dadurch sind viele der durch heutige Standardverfahren ermittelten Resultate unbrauchbar bzw. unvollständig.

Mit dieser Arbeit liegt erstmals ein validiertes, ganzheitliches numerisches Verfahren vor, welches die relevanten hydrodynamischen Aspekte, die während des Verladevorgangs auftreten, vollständig berücksichtigt. Vertiefende Untersuchungen auf Basis dieses Verfahrens tragen zum grundlegenden Verständnis der auftretenden Effekte bei, wodurch eine fehlerfreie Ergebnisextrapolation vom Modell auf die Großausführung ermöglicht wird. Die

vorgestellte Methode in Kombination mit dem erlangten Hintergrundwissen kann als vertrauenswürdige Ausgangsbasis für Machbarkeitsstudien und Einsatzgrenzenbestimmungen von FLNG-Projekten herangezogen werden. Es zeigt sich, dass das gewählte lineare, auf Potentialtheorie beruhende Verfahren sowohl im Hinblick auf die Bewegungscharakteristika unter Einfluss von freien Flüssigkeitsoberflächen als auch auf die Fluidauslenkungen in den Tanks hervorragende Ergebnisse liefert. Der gesamte Analysevorgang wird exemplarisch für das MPLS20-System in der *Haltenbanken*-Region durchgeführt.

Vertiefende numerische Untersuchungen zeigen erstmals, dass die Differenzen zwischen Tankresonanzfrequenzen und den durch internes Sloshing verursachten Maxima der entsprechenden Bewegungsübertragungsfunktionen vom Verhältnis der Festkörpermasse zur hydrodynamischen Masse des Schiffes abhängen. Hierbei ist die hydrodynamische Kopplung zwischen Bewegungsfreiheitsgraden ein ausschlaggebender Faktor. Die wichtigste Schlussfolgerung aus dieser Beobachtung ist, dass Ergebnisse aus Modellversuchen oder Simulationen mit Wasser in den Ladetanks aufgrund unterschiedlicher Verhältnisse von fester zu flüssiger Masse — und damit unterschiedlichen Verschiebungen der Maxima — entgegen des oftmals praktizierten Vorgehens nicht auf den realen Betrieb mit LNG extrapoliert werden können.

Durch umfassende dreidimensionale Analysen kann außerdem erstmals gezeigt werden, dass bei Flüssiggastankern aufgrund von Asymmetrien in der Geometrie des Unterwasserschiffes sowie in der Massenverteilung Tanksloshing und dadurch induzierte, nicht zu vernachlässigende Starrkörperbewegungen senkrecht zur Angriffsrichtung der erregenden Wellenkräfte auftreten. Diese Beobachtung lässt den Schluss zu, dass durch eine — oftmals in der Literatur anzutreffende — idealisierte, zweidimensionale Betrachtung der Problemstellung keine vollständigen Aussagen über das Bewegungsverhalten von Schiffen mit teilgefüllten Tanks zu treffen sind.

# Contents

**Acknowledgement** **iii**

**Abstract** **v**

**Kurzfassung** **vii**

**List of Figures** **xiii**

**List of Tables** **xv**

**1 Introduction** **1**
1.1 Outline . . . . . 1
1.2 Marine Natural Gas Exploitation . . . . . 2
1.2.1 Liquefaction Facilities . . . . . 4
1.2.2 Reception Facilities . . . . . 5
1.2.3 Cryogenic Transfer Technologies . . . . . 8
1.3 The MPLS20 Project . . . . . 9
1.4 State-of-the-Art . . . . . 11
1.4.1 Sloshing . . . . . 11
1.4.2 Multi-Body Effects . . . . . 17
1.4.3 Summary . . . . . 17

**2 Description of the Numerical Method** **21**
2.1 Potential Theory . . . . . 21
2.2 Hydrodynamic Forces and Motions . . . . . 25
2.3 Internal Tank Effects . . . . . 26
2.4 Operational Limitations . . . . . 31
2.5 Damping . . . . . 35

**3 Hydrodynamic Challenges** **37**
3.1 Initial Stability . . . . . 38
3.2 Sloshing . . . . . 40
3.3 Coupling of Sloshing and Ship Motions . . . . . 45
3.3.1 Validation of the Numerical Method . . . . . 47

3.3.2 Discussion I: Frequency Shifts . . . . . 51
3.3.3 Discussion II: Asymmetries . . . . . 62
3.4 Multi-Body Analysis . . . . . 68
3.5 Stochastic Analysis . . . . . 80
3.5.1 Worst Case Identification . . . . . 81
3.5.2 Determination of the Operational Range . . . . . 84
3.6 Excursion I: Exemplary Variations . . . . . 89
3.7 Excursion II: Mooring Analysis . . . . . 93

**4 Conclusions & Consequences 99**

**Bibliography 110**

**Nomenclature 111**

**A Input Data for Numerical Calculations 119**

**B The Dynamic Magnification Factor 125**

# List of Figures


1.1 World energy demand (*source: International Energy Agency, 2008*) and capital expenditure on FLNG facilities (*source: Douglas Westwood Limited, 2009*) . . . . . 2
1.2 Current concepts for marine natural gas liquefaction (*source: Shell, 2009 and Flex LNG, 2009*) . . . . . 4
1.3 Current concepts for marine LNG reception and regasification (*source: Business Wire, 2009, Excelerate Energy, 2009, www.marinelog.com, 2008 and TORP LNG, 2010*) . . . . . 6
1.4 Cryogenic transfer technologies (*source: FMC Technologies, 2010 and Bluewater, 2010*) . . . . . 8
1.5 Loading procedure with the MPLS20 system in tandem configuration (*source: IMPaC Offshore Engineering, 2010*) . . . 9
1.6 Prismatic tank with characteristic dimensions . . . . . 11

2.1 Cuboid tank restoring coefficients . . . . . 27
2.2 Cuboid tank added mass . . . . . 29
2.3 Tank surface deflections for odd and even modes . . . . . 30
2.4 Pierson-Moskowitz versus JONSWAP spectra . . . . . 32
2.5 Probability density distribution of the maximum wave height 34
2.6 Exemplary roll decay measurement . . . . . 36

3.1 Discretization of the FLNG terminal and the LNGC . . . . . 37
3.2 Decrease of initial stability due to free fluid surfaces . . . . . 39
3.3 Example of numerical sloshing mode determination from absolute values of $a_{22,T}$ . . . . . 40
3.4 Cuboid tank with characteristic dimensions . . . . . 41
3.5 Comparison of numerical and analytical cuboid tank resonance frequencies . . . . . 42
3.6 Comparison of numerical and analytical prismatic tank resonance frequencies . . . . . 44
3.7 Coupling of sloshing and ship motions: motivation . . . . . 45
3.8 Onboard camera captures of sloshing motions . . . . . 46
3.9 Equipment of the LNGC model for validation tests . . . . . 47

3.10 Validation of the numerical method: Body motions with 30% filling height . . . . . 48
3.11 Validation of the numerical method: Internal fluid motions for $\beta = 90°$ . . . . . 49
3.12 Validation of the numerical method: Internal fluid motions for $\beta = 180°$ . . . . . 50
3.13 Comparison of roll motion and internal tank surface elevations 52
3.14 Schematic backtracing of the first transverse sloshing peak shift 54
3.15 Comparison of surge motion and internal tank surface elevations 56
3.16 Schematic backtracing of the first longitudinal sloshing peak shift . . . . . 58
3.17 Comparison of the roll and surge motion RAOs for 30% fresh water and LNG filling . . . . . 59
3.18 Comparison of the first sloshing mode and the motion response peaks . . . . . 60
3.19 Comparison of the first sloshing mode and the yaw response peaks . . . . . 61
3.20 Internal surface elevations in tank 4 . . . . . 63
3.21 Internal surface elevations in all four tanks . . . . . 64
3.22 Elimination of the asymmetries of the original LNGC hull in two steps . . . . . 65
3.23 Comparison of surge, roll and fluid motions for three geometry variants . . . . . 66
3.24 Validation of the numerical method: Further body motions with 30% filling height . . . . . 67
3.25 Approach of the LNGC to the 'Mooring Bay' of the FLNG terminal in three steps (*source: IMPaC Offshore Engineering, 2010*) . . . . . 69
3.26 Relevant motion RAOs of LNGC and FLNG terminal for the approach phases ($\beta = 180°$) . . . . . 71
3.27 Convention for the relative motions of the coupling points of the LNG transfer pipe (*source: IMPaC Offshore Engineering, 2010*) . . . . . 73
3.28 Translatory relative motions of the coupling points of the LNG transfer pipe for 30% LNG filling height and all incident wave angles . . . . . 74
3.29 Rotatory relative motions of the coupling points of the LNG transfer pipe for 30% LNG filling height and all incident wave angles . . . . . 76
3.30 Translatory relative motions of the coupling points of the LNG transfer pipe for selected incident wave angles and all LNG filling heights . . . . . 78

3.31 Rotatory relative motions of the coupling points of the LNG transfer pipe for selected incident wave angles and all LNG filling heights . . . . . 79
3.32 Relative $x$-motion amplitudes from the worst case analysis with respect to the filling height . . . . . 82
3.33 Relative $z$-motion amplitudes from the worst case analysis with respect to the filling height . . . . . 83
3.34 Relative $x$- and $z$-motion amplitudes from the worst case analysis with respect to the filling height and the incident wave angle . . . . . 85
3.35 Scheme for the determination of the tolerable sea states for the worst case relative $x$- and $z$-motion . . . . . 86
3.36 Determination of the resulting limiting parameter and feasible sea states . . . . . 87
3.37 Exemplary annual downtime for the Haltenbanken region . . 88
3.38 Discretization of the LNGC with MOSS type tanks . . . . . 89
3.39 Comparison of selected LNGC motion RAOs for prismatic and spherical tanks . . . . . 90
3.40 Relative motions between the coupling points of the LNG transfer pipe for side-by-side and tandem configuration . . . . 91
3.41 Surface elevation in the gap between FLNG terminal and LNGC in side-by-side configuration (*image source: Capt. Mark Scholma*) . . . . . 92
3.42 Illustration of the FLNG turret mooring layout . . . . . 93
3.43 Static configuration of a single mooring line . . . . . 94
3.44 Excursion vs. exciting forces and stiffness depending on pretension . . . . . 95
3.45 Mean drift forces on the FLNG terminal in regular waves . . 96
3.46 Slowly-varying wave drift forces and surge drift motions of the FLNG terminal . . . . . 97

# List of Tables


1.1 Countries participating in the worldwide natural gas trade . . 3
1.2 Main dimensions of the MPLS20 vessels . . . . . 10
1.3 Dimensions of the LNGC's prismatic tanks . . . . . 11

3.1 Dimensions of the cuboid tank . . . . . 41
3.2 Turret mooring line characteristics of the FLNG terminal . . 94
3.3 Mean excursion and stiffness characteristics for the FLNG terminal . . . . . 96
3.4 Significant and maximum slow-drift excursions of the terminal in surge direction . . . . . 98

A.1 Input data for calculations with one detached cuboid tank . . 121
A.2 Input data for calculations with one detached prismatic tank 122
A.3 Input data for single-body calculations . . . . . 123
A.4 Input data for multi-body calculations . . . . . 124

# Chapter 1

# Introduction

## 1.1 Outline

This thesis provides a holistic numerical approach covering and explaining all relevant hydrodynamic challenges related to offshore LNG transfer.

At first, an overview on the LNG market, operating and proposed liquefaction and reception facilities as well as cryogenic transfer technologies is provided in section 1.2. The MPLS20 concept, which is characterized by a LNG carrier moored to a 'Mooring Bay' at the stern of a FLNG in tandem configuration is introduced in section 1.3. All exemplary investigations are based of this concept and the involved vessels. In the literature review section 1.4, an overview on published approaches and methods to investigate sloshing-induced structural loads, coupling effects between internal tank sloshing and vessel motions in waves as well as hydrodynamic effects of multi-body arrangements for two vessels at close proximity is given. It is pointed out which issues of offshore LNG transfer are covered by these methods and which aspects require the research work that is presented in this thesis.

The theoretical background to the numerical approach that is chosen for the investigation of the identified aspects is provided in chapter 2. Here, a brief summary on the basics of linear potential theory — including internal tank effects — and the forces and motions in waves given. In addition, the basic concept of the classical spectral stochastic analysis and some aspects of modeling nonlinear viscous damping effects in a linear numerical model complete this chapter.

In the main part of this thesis, the hydrodynamic challenges of offshore LNG transfer are presented. The impact of free fluid surfaces on the initial stability of a vessel is discussed in section 3.1, followed by a description of resonant sloshing in detached rectangular and prismatic tanks in section 3.2. In the next step, a vessel equipped with four equivolumetric prismatic tanks is considered in section 3.3. Subsequent to the validation of the numerical

method by model test data, it is analyzed in detail how the presence of liquid cargo of variable filling height influences the seakeeping behavior of the vessel. Two phenomena are investigated in detail: The frequency shift of the sloshing peak (cf. section 3.3.2) and the occurrence of asymmetric effects (cf. section 3.3.3). From now on, the LNGC is not considered alone, but the MPLS20 offloading procedure including the presence of the FLNG terminal is taken into account in section 3.4, where the approach and transfer phase are analyzed, including the relative motions between the coupling points of the cryogenic transfer pipe for various incident wave angles and tank filling heights. On the basis of this four-dimensional data, an exemplary determination of the operational range of the system for the *Haltenbanken* region is conducted with given limiting relative motions between the two vessels (cf. section 3.5). Finally, two excursions indicate further aspects that should be considered in the analysis of offshore LNG transfer systems.

Conclusions of the presented work along with consequences for the investigation of offshore LNG transfer systems are provided in chapter 4.

## 1.2 Marine Natural Gas Exploitation

For several decades, natural gas was merely a byproduct of oil production or was even combusted through flare booms. Today, its importance as energy source is undoubted and the demand for natural gas is continuously growing (see Fig 1.1, left and International Energy Agency (2010)). Currently, there are 26 onshore export or liquefaction facilities worldwide for natural gas, situated in 15 countries while 18 countries worldwide are importing LNG (Liquefied Natural Gas) by 60 on- and offshore regasification facilities (cf. Tab. 1.1). Approximately 65 marine liquefaction terminal projects and 181 regasification terminal projects have currently been either proposed or are under construction (The California Energy Commission (2012)). More

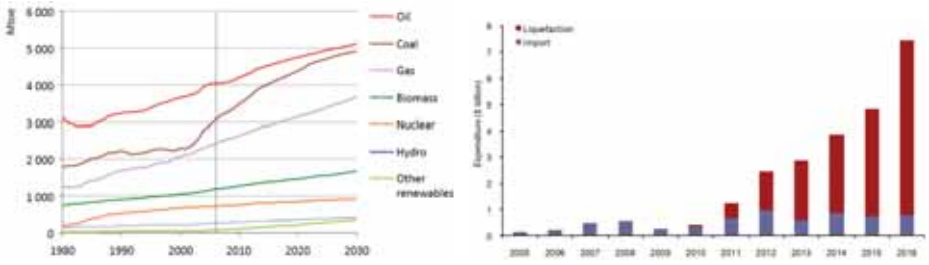


Figure 1.1: *World energy demand from 1980 – 2030 by source (left) and capital expenditure on import and liquefaction FLNG facilities from 2005 – 2016 (right)*

Table 1.1: *Countries participating in the worldwide natural gas trade with the respective start up dates (The California Energy Commission (2012))*

| country | status | start up date |
|---|---|---|
| Algeria | exporting | 1971 |
| Australia | exporting | 1989 |
| Belgium | importing | 1972 |
| Brunei | exporting | 1987 |
| China | importing | 2006 |
| Dominican Republic | importing | 2003 |
| Equatorial Guinea | exporting | 2007 |
| Egypt | exporting | 2004 |
| France | importing | 1972 |
| Greece | importing | 2000 |
| India | importing | 2004 |
| Indonesia | exporting | 1977 |
| Italy | importing | 1971 |
| Japan | importing | 1969 |
| Malaysia | exporting | 1983 |
| Mexico | importing | 2006 |
| Nigeria | exporting | 1999 |
| Norway | exporting | 2007 |
| Oman | exporting | 2000 |
| Portugal | importing | 2003 |
| Puerto Rico | importing | 2000 |
| Qatar | exporting | 1997 |
| South Korea | importing | 1986 |
| Spain | importing | 1969 |
| Taiwan | importing | 1990 |
| Trinidad & Tobago | exporting | 1999 |
| Turkey | importing | 1992 |
| United Arab Emirates | exporting | 1977 |
| United Kingdom | importing | 2005 |
| United States of America | im-/exporting | 1971/1969 |

and more large natural gas fields in remote offshore locations are planned to be exploited. Until a few years ago, the challenge to develop these resources was not accepted and no technology — i.e. floating processing and liquefaction plants — was available. This attitude has changed and today, more and more companies attempt to participate in this rapidly growing market (see also Fig. 1.1, right).

Since the transport of natural gas via pipelines is not economic with increasing distance, different *Floating Liquefied Natural Gas* (FLNG) solutions have been developed: Most of these concepts comprise of an offshore terminal that produces, stores and periodically transfers the liquefied gas to shuttle tankers which call at special deepwater ports or other regasification facilities close to or on-shore. Liquefaction of natural gas requires cryogenic conditions of -162°C and reduces the volume to $1/600^{\text{th}}$. Since the energy density increases by the factor 600 at the same time, LNG is a hazardous cargo. In the following, an overview on currently existing and proposed concepts for marine natural gas liquefaction and regasification concepts and techniques is provided (without this survey being claimed to be exhaustive).

### 1.2.1 Liquefaction Facilities

Until today, no offshore liquefaction facilities are operating, but the progress of several projects is considerable (see Douglas Westwood Limited (2010)). All concepts feature large turret-moored terminal barges.

In July 2009, *Shell Gas & Power Developments BV* signed a contract with *Technip* and *Samsung Heavy Industries*, forming a consortium to develop, construct and install several floating liquefaction terminals (referred to as FLNG terminals in the following) within the next 15 years (Gilmour and Deveney (2010)). An impression of the 480 m long and 75 m wide terminal vessel, which is designed for side-by-side offloading is shown in Fig. 1.2

Figure 1.2: *Current concepts for marine natural gas liquefaction by Shell/Technip (left) and Flex LNG (right)*

(left). The first application for this concept will be off the coast of Western Australia, where Shell's *Prelude* and *Concerto* gas fields are situated. Further potential FLNG projects in this region are the *Sunrise* and *Browse* fields.

Founded in 2006, *Flex LNG* is specialized in developing solutions for offshore LNG production. In co-operation with *Samsung Heavy Industries*, the *Flex LNG Producer* (LNGP) was developed (see Fig. 1.2, right and Pastoor et al. (2009)). This 336 m long and 50 m wide liquefaction terminal vessel is connected to the gas field via a turret buoy system by *APL AS*. Shuttle carriers can be loaded either in side-by-side or in tandem configuration. In April 2011, *Flex LNG* had signed agreements with *InterOil Corporation* (IOC), *Pacific LNG Operations Ltd.* (PacLNG), *Liquid Niugini Gas* (LNGL) and *Samsung Heavy Industries* for the Gulf LNG project in Papua New Guinea. From mid 2014 on, LNGP1 is scheduled to be moored alongside a jetty and produce natural gas from the *Elk* and *Antelope* onshore gas fields in the Eastern Papuan Basin northwest of Port Moresby.

Further efforts in offshore liquefaction development are made by *SBM Offshore*, who propose a LNG FPSO (LNG Floating Production, Storage and Offloading) terminal for side-by-side as well as tandem offloading. Having signed a contract with *Petrobras*, *SBM* plans to install a LNG FPSO in the Campos Basin off the Brazilian coast. Due to the sea conditions in this region, it will be operating in tandem configuration. In July 2011, *SBM Offshore* signed a contract with *PTT FLNG Ltd.* and *PTTEP Australasia* to develop an FLNG terminal for the exploitation of the *Cash/Maple*, *Oliver* and *Southern* gas fields off the Australian north coast in the Timor Sea from 2016 on.

Norwegian *Höegh LNG* also developed a LNG FPSO terminal for tandem offloading with flexible hoses and side-by-side offloading with three rigid arms — two for LNG and one for LPG (Liquefied Petroleum Gas) — which received an approval in principle from *DNV* in June 2009.

### 1.2.2 Reception Facilities

In contrast to the liquefaction facilities, there is already some progress visible in floating LNG reception facilities.

The first solution that was realized is the *Energy Bridge™* principle, developed by the Texas based company *Excelerate Energy*. Until today, a total of eight Energy Bridge Regasification Vessels (EBRV) is in operation. The concept is suitable for both, ship-to-shore transfer (GasPort) as well as offshore transfer (Gateway). In both cases, a conventional LNG carrier is moored side-by-side to an EBRV which regasifies the LNG. In case of GasPorts, shore-based loading arms transfer the gas into the downstream delivery infrastructure, while for offshore Gateways, cone-shaped STL buoys (Submerged Turret Loading, see Fig. 1.3, top right) are applied to transfer

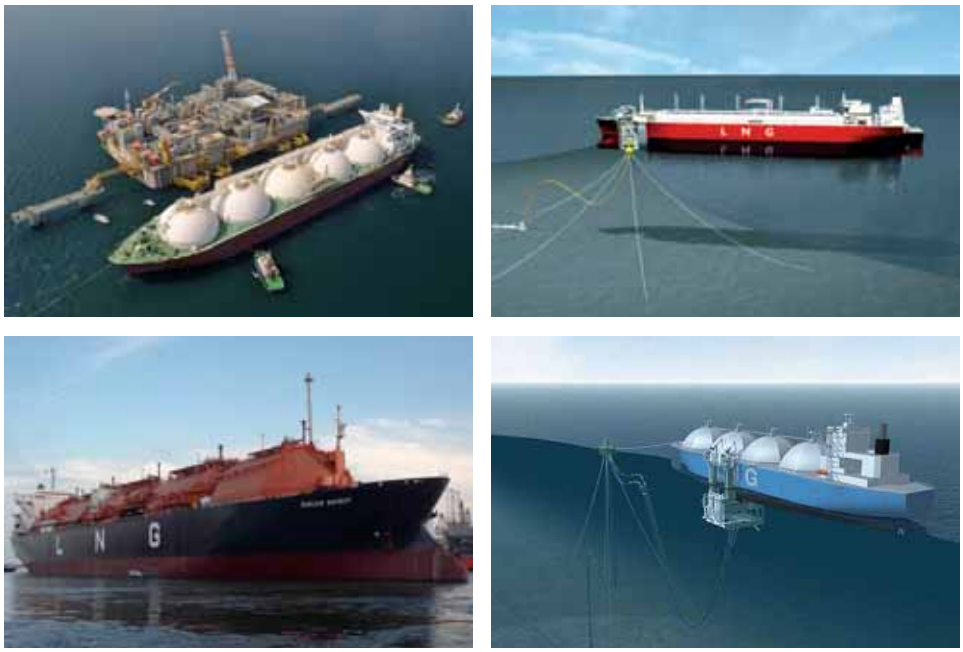


Figure 1.3: *Current concepts for marine LNG reception and regasification by Aker Solutions (Adriatic LNG, top left), Excelerate Energy (Excelerate Energy Bridge, top right), Golar LNG (Golar Spirit FSRU, bottom left) and TORP LNG (HiLoad System, bottom right)*

the gas via pipelines to the onshore infrastructure (Cook (2006)). Worldwide, *Excelerate* currently operates four GasPorts (Teesside/Great Britain since 2007, Bahía Blanca/Argentina since 2008, Mina Al-Ahmadi/Kuwait since 2009 and GNL Escobar/Argentina since 2011) as well as one Gateway (Northeast Gateway, since 2008 off the coast of Massachusetts) — the Gulf Gateway off the coast of Louisiana was in operation since 2005 but will be decommissioned in 2012.

The second type of marine LNG reception facility that is already operating is *Adriatic LNG*, built by *Aker Solutions* for *Exxon Mobil*. Since 2008, conventional LNG carriers are calling at this GBS terminal (Gravity Based Structure), situated 15 km off Porto Levante in the Adriatic Sea (see Fig. 1.3, top left). LNG is transferred in side-by-side configuration to the GBS, where the regasification process takes place. Subsequently, the gas is transferred to the Italian mainland via pipelines.

*Golar LNG* is specialized in converting former LNG carriers into so-called FSRUs (Floating Storage and Regasification Unit), which can either operate offshore or in harbours (see Fig. 1.3, bottom left). In both scenarios, LNG offloading is conducted in side-by-side configuration with rigid loading arms. Two harbour-based FSRUs are currently operating for *Petrobras* in

Brazil (*Golar Spirit* in Pecém and *Golar Winter* in Rio de Janeiro, both since 2009) and a third unit, *Golar Freeze* is in service for the *Dubai Supply Authority* (DUSUP) since late 2010 in Jebel Ali/Dubai. *Golar Frost*, the first offshore unit is currently under conversion for the *Toscana LNG* project and is scheduled to operate from late 2012 on off Livorno in the Mediterranean Sea. *Golar LNG's* second offshore FSRU *Khannur* is currently also under conversion and will operate for the *West Java LNG* project 15 km offshore in the Jakarta Bay in Indonesia.

Norwegian *Höegh LNG's* current portfolio in reception facilities comprises deepwater ports, FLNG units and FSRUs. Two deepwater ports in the U.S. — the already officially licensed *Neptune Deepwater Port* off the coast of Massachusetts and *Port Dolphin* off Florida — as well as *Port Meridian* off the English west coast are planned. Similar to the *Energy Bridge™* principle, these ports will feature SRVs (Shuttle Regasification Vessel) in combination with STL buoys. Together with *Gaz de France-Suez*, *Höegh LNG* is developing a FSRU for side-by-side offloading for the *Triton LNG* project in the Adriatic Sea. In June 2009, *Höegh's* LNG FPSO concept received an 'Approval in Principle' from *DNV*. This FLNG receiving facility is designed to transfer liquefied gas offshore to shuttle carriers in side-by-side (three rigid loading arms for LNG, two for LPG) as well as tandem configuration (flexible pipes).

While most of the technological solutions for offshore LNG offloading proposed so far are based on vessel-to-vessel transfer with rigid loading arms or flexible hoses, *Torp's HiLoad* system is a completely different approach. The problematic scenario of two large vessels interacting at close proximity in rough seas is avoided by a L-shaped frame mounted to the carrier vessel where it is held in position by friction forces (see Fig. 1.3, bottom right). *HiLoad* can be used in combination either with a regasification terminal at great distance (*Bienville Offshore Energy Terminal* in the Gulf of Mexico, currently under review) or alone (planned for the *Esperanza* project off the coast of California). In the latter case, the carrier is moored to a buoy and *HiLoad* itself regasifies and transfers the cargo to the mainland via pipelines. For sheltered shallow water regions, *Torp* has developed the *EasyLNG* system, which consists of a barge with regasification plants for offloading in side-by-side configuration.

Currently almost all oil and gas companies are trying to participate in this new, dynamic offshore LNG market with their own technologies and concepts. To name a few among them, *Bluewater*, *Sevan Marine*, *Moss Maritime* or *Saipem* are also proposing FLNG solutions. *ExxonMobil* plans to design a FLNG terminal for the *BlueOcean* project off the coast of New Jersey, and Norwegian *Framo Engineering* — part of the OCT consortium (Offshore Cryogenic Transfer) — proposes a FLNG system for tandem loading, which features an A-frame in combination with a crowfoot-mooring arrangement. Japanese *INPEX* have also developed large side-by-side oper-

ated FLNG units (length 500 m, breadth 82 m) for two projects off northern Australia — *Ichthys LNG* and *Abadi LNG*.

### 1.2.3 Cryogenic Transfer Technologies

The design of the cryogenic transfer system and the related motion capabilities are the central boundary condition for the operational range of the entire FLNG system. The two transfer configurations — tandem and side-by-side — are characterized by specific transfer technologies. For side-by-side transfer, *FMC Technologies'* rigid *Marine Loading Arms* are currently state-of-the art (see Fig. 1.4, left). They have been designed by *FMC* to handle relative motion amplitudes between the two vessels of ±1.0 m in longitudinal, ±2.0 m in transverse and ±1.2 m in vertical direction. Due to these limitations, side-by-side transfer with rigid loading arms is currently possible only for calm waters to moderate sea states — as for the Adriatic Sea, where the *Adriatic LNG* GBS is equipped with this technology.

In tandem configuration, the coupling points for the cryogenic transfer system are typically located at the bow of the carrier and the stern of the terminal, instead of midships as for the side-by-side configuration. Since this implies larger relative motions that have to be handled, aerial or floating flexible pipes instead of rigid arms have to be used. Dutch *Bluewater* developed a cryogenic transfer pipe of 8" to 16" inner diameter for aerial applications (see Fig. 1.4, right), but so far only a prototype was built. The *OCT* consortium (Offshore Cryogenic Transfer), led by Norwegian *Framo Engineering*, also developed an offshore transfer system for LNG in tandem configuration - which is not in operation until today (Frohne et al. (2008)).

In order to develop a save and efficient offshore LNG transfer system that exceeds the capabilities of the state-of-the-art technologies, the re-

Figure 1.4: *Cryogenic transfer technologies: rigid loading arms by FMC Technologies for side-by-side configuration (left), prototype of flexible cryogenic hoses by Bluewater for tandem offloading (right)*

search project *MPLS20 — Maritime Pipe Loading System 20"* was funded by the German Federal Ministry of Economics and Technology (BMWi) in 2007. The system developed by the MPLS20 consortium consisting of *Nexans Deutschland*, *Brugg Pipe Systems*, *IMPaC Offshore Engineering* and *Technical University of Berlin* (TU Berlin) is presented in the following section.

## 1.3 The MPLS20 Project

Within the framework of the joint research project MPLS20, an innovative offshore transfer system between a turret-moored FLNG terminal barge and a LNG shuttle carrier in tandem configuration has been developed and analyzed. The proposed transfer system consists of a generic FLNG terminal design with the new 'Mooring Bay' concept, a modified standard LNG carrier (LNGC) and the approach and handling system for the developed 16" transfer pipes (see Fig. 1.5, Hoog et al. (2009a) and Hoog et al. (2009b)). The FLNG terminal (for main dimensions see Tab. 1.2) features a wave flattening bow and provides a cargo loading capacity of up to 280,000 $m^3$ LNG in five independent SPB tanks (Self-supporting, Prismatic, IMO Type B) which are sloshing-proof and offer a flat deck. The LNGC (for main dimensions see Tab. 1.2) is equipped with four membrane tanks and is slightly modified compared to today's standards, as one additional and specially designed receiving manifold is placed at the bow deck area. This bow manifold completely enters the 'Mooring Bay' at the stern of the terminal when the LNGC is moored for cargo transfer, significantly reducing the free span lengths of the transfer pipes compared to crude oil transfer techniques. The distance between the bow of the LNGC and the stern of the FLNG is 10 m in this configuration. The bow deck area accommodates standard anchor

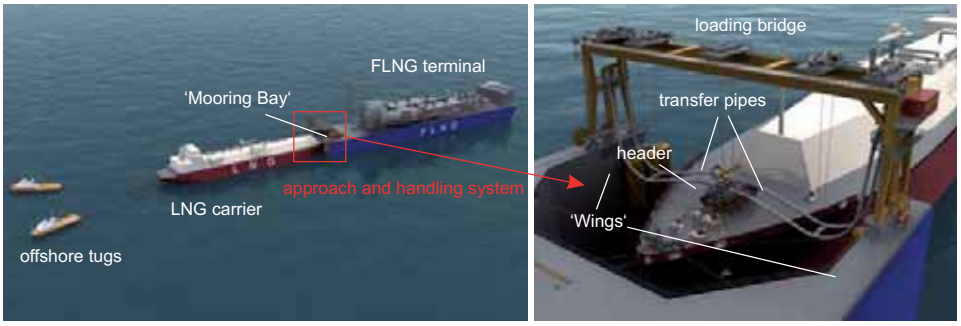


Figure 1.5: *Illustration of the loading procedure with the MPLS20 system in tandem configuration showing the overall arrangement (left) as well as the 'Mooring Bay' concept (right)*

Table 1.2: *Main dimensions of the MPLS20 vessels*

| Parameter | FLNG terminal | LNGC |
|---|---|---|
| Length over all, $L_{OA}$ [m] | 360 (+ 40 'Mooring Bay') | 282 |
| Breadth, $B_V$ [m] | 65 | 42 |
| Draft, $D_V$ [m] | 12 | 12 |
| Height, $H_V$ [m] | 33 | 26 |
| Displacement, $\forall_V$ [m$^3$] | 275,087 | 103,921 |
| Loading capacity, $V_L$ [m$^3$] | 280,000 | 133,880 |

winches and — if necessary — chain stoppers as well as Quick Release Hooks (QRH) for mooring. Due to active ballasting, the LNGC as well as the FLNG terminal operate at a constant draft of 12 m.

For safe and fast loading/offoading procedures, a corrugated, vacuum insulated transfer pipe of 16" inner diameter for cryogenic liquids has been developed — which significantly exceeds currently existing pipe diameters and hence transfer rates.

The mooring system features the patented 40 m long 'Mooring Bay', built of two 'Mooring Wings' which are fixed to the FLNG terminal stern at starboard and portside, respectively. This concept allows safe loading in harsh seas and even ice conditions (see Hoog et al. (2012)). The mooring of the LNGC results in a symmetrical arrangement of six moorings each operated by load adequate winches and heave compensation systems. The arrangement provides a unique solution to stop the incoming vessel in a controlled manner at the required position right below the loading bridge as the LNGC is actively pulled into the 'Mooring Bay'. A rail-mounted movable loading crane bridges the 'Mooring Bay' from one wing to the other allowing simultaneous handling of up to six transfer pipes by means of a header. In addition, the crane accommodates the cargo transfer flanges which are located high above the wings' weather decks so that handling, draining and purging of the flexible pipes can be carried out in a safe, efficient and reliable way. For coupling of the transfer pipes to the LNGC bow manifold, standard Quick Connect/Disconnect Couplers (QCDCs) and Emergency Release Couplers (ERCs) are used.

The MPLS20 vessels provide the basis for all investigations presented in this work and are denoted by the abbreviations LNGC and FLNG terminal in the following chapters. The LNGC features four equivolumetric prismatic tanks with a total capacity of 133,880 m$^3$ and the characteristic dimensions given in Fig. 1.6 and Tab. 1.3. The subsequent sloshing analyses are conducted with these tanks, where the standard case is 30% filling height. The key results of the MPLS20 project are published by Frohne et al. (2010).

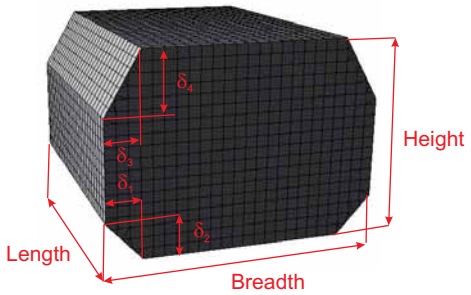


Figure 1.6: *Numerical discretization of the LNGC's prismatic tank with characteristic dimensions*

| | |
|---|---|
| Length, $L_T$ [m] | 38.3 |
| Breadth, $B_T$ [m] | 35.8 |
| Height, $H_T$ [m] | 26.1 |
| $\delta_1$ | 4.65 |
| $\delta_2$ | 5.0 |
| $\delta_3$ | 4.65 |
| $\delta_4$ | 8.0 |
| Volume, $V_T$ [m$^3$] | 33,470 |

Table 1.3: *Dimensions of the LNGC's prismatic tanks*

## 1.4 State-of-the-Art

Offshore offloading of LNG from a floating terminal vessel to a floating LNGC is a delicate and challenging procedure. Due to its high energy density, LNG is an extremely hazardous cargo and safe transfer operations require detailed knowledge on all involved hydrodynamic effects, which are

- Structural loads on tank walls caused by sloshing effects in partially filled tanks,
- Modified seakeeping behavior of the LNGC caused by sloshing in partially filled tanks and
- Modified seakeeping behavior due to multi-body effects.

In the subsequent paragraphs, methods and approaches to analyze these issues that have been published so far are compiled.

### 1.4.1 Sloshing

Free fluid surfaces in moving containers with related resonant sloshing phenomena pose a problem not only in marine applications. In fact, extensive research work on sloshing in aircraft and rocket fuel tanks has been published since the 1960s. After several accidents, especially NASA researchers have studied the influence of free fluid surfaces in fuel tanks on the dynamic stability of rockets. Among several publications, the important and pathbreaking report by Abramson (1966) should be mentioned.

In marine applications, sloshing may even be desired — specially designed antiroll tanks on ships act as liquid damping systems that help reducing roll motion amplitudes (see SNAME (1989a)). Similar system are installed in very tall buildings to decrease wind-induced oscillations.

Due to its dangerous impact, undesired or uncontrolled sloshing in marine applications is a field of extensive research work. Recently, Faltinsen and Timokha (2009) compiled a comprehensive book covering a wide range of issues related to marine sloshing. A comprehensive review of existing approaches to the sloshing problem was published by Ibrahim (2005).

Wave-induced vessel motions excite liquid motions inside large partially filled cargo tanks, as they are typical for cargo ships carrying oil, chemicals, liquid food, LNG or LPG. Unlike tanks for LNG transport, the large cargo tanks for LPG, oil, chemicals and liquid food transport are subdivided by bulkheads with openings to reduced the effective tank dimension for sloshing motions. LNG tanks are classified into non-freestanding tanks (membrane tanks, e.g. *Technigaz Mark III* and *Gaz Transport NO96*) and freestanding tanks (e.g. *MOSS* tanks or *IHI SPB*). Due to safety regulations, no welding is allowed on the internal tank barriers which have to withstand extreme temperatures and pressure. Therefore, all LNG tank types feature large, clean volumes without any subdividing internal structures like bulkheads and are particularly prone to violent sloshing effects.

The influence of these sloshing motions is extremely strong for excitations in the vicinity of the first natural frequency of the tank. In general two major issues are caused by marine sloshing effects: structural problems due to high pressure on the tank walls and altered seakeeping behavior of the vessel due coupling effects of sloshing and ship motions.

### Structural Loads

Local pressure peaks occur especially at discontinuous locations of the inner tank walls, i.e. corners, chamfers etc. In order to investigate structural loads due to sloshing, **model tests** can be conducted. Common setups consist of single small scale tanks (1:20 to 1:70) mounted to hexapods that allow motions in six degrees of freedom. Pressure sensor clusters are installed to measure loads at different positions on the tank walls. Apart from difficulties in measuring the pressure peaks that are extremely localized in space and time, scaling becomes an issue since hydroelastic effects may couple pressure and structural responses (see Graczyk and Moan (2009)).

Typical measurements of pressure distributions along vertical tank walls in space and time are shown by Repalle et al. (2010a) for a rectangular tank mounted to a hexapod. Further investigations by Repalle et al. (2010b) showed the influence of the sampling rate and model test duration on the impact pressure measurements. It is recommended to select a sample rate of 40 kHz and measure the impact pressure for 10 min under regular sinusoidal conditions.

Local impact loads due to sloshing can also be calculated by **numerical methods**. Some recommendations and comparisons between basic potential theory, RANSE solvers and experimental data regarding pressure and sur-

face elevation is provided by Thiagarajan et al. (2011). Since numerical analyses of these transient phenomena require an exact reproduction of the liquid free surface in combination with effects such as spray and entrapped air in the vicinity of the tank walls, RANSE-based (Reynolds-Averaged Navier-Stokes Equation) approaches provide an appropriate and popular method. Several well-known CFD solvers were proven to be capable of capturing pressure impacts on internal walls of moving tanks. Alternatively, Rafiee et al. (2009) presented a numerical approach to simulate two-dimensional sloshing flows by applying the SPH (Smooth Particle Hydrodynamics) method, a meshless, purely Lagrangian approach where the fluid is represented by randomly distributed 'particles'. This approach was also selected by Pákozdi (2008), who adapted the standard SPH method to a 'smoothed SPH method' by implementing various time integration approaches, a new definition for introducing density as well as a moving least square method in order to investigate the nonlinear effects of two-dimensional sloshing in box-shaped tanks. However, the vast majority of publications include analyses of separate tanks, that are not mounted to a vessel moving in waves, hence direct coupling is often not considered.

Sames et al. (2002) showed two-phase flow simulation results for rectangular and cylindrical tanks obtained with a finite volume method based on the commercial solver COMET, where the interphase was tracked with the High Resolution Interface Capturing scheme (HRIC). The predicted pressure at different tank wall positions showed good agreement with experimental data from the EUROSLOSH research project.

Schreier and Paschen (2008) investigated sloshing inside a prismatic tank with the commercial CFD solver ANSYS CFX. Two interesting phenomena were found: The occurrence of local high pressure peaks at low filling heights is related to flows along the tank walls towards discontinuities such as knuckles, leading to abrupt changes of the direction of the fluid momentum. At high filling levels, very low pressures may occur, that last significantly longer and affect larger tank wall areas. These observations are related to tank roof effects. Further studies by Schreier et al. (2009) revealed the importance of transient effects such as the sudden encounter of a LNGC with partially filled tanks with a steep wave. Pressure impacts were found to be several times higher as compared to harmonic excitation at resonance.

A RANSE/VOF (Volume of Fluid) method based on the commercial solver FLUENT was used by Rakshit et al. (2008) to conduct two-dimensional studies in order to investigate the influence of varying filling height and sway excitation frequency on the impact pressure. Three-dimensional simulations with FLUENT to predict sloshing pressure in a prismatic tank were presented by Rhee (2004). The comparison with experimental data showed good agreement on unstructured as well as structured grids at low filling levels. The implementation of a suitable turbulence model was considered to be critical in order to capture violent liquid motions correctly.

The capability of MARIN's volume of fluid (VOF) solver COMFLOW to simulate local, short-term pressure peaks was investigated by Huijsmans et al. (2004). Experimental pressure measurements and high-speed video captures are compared to numerical results for a rectangular tank exposed to forced harmonic roll motions. It was found that it is difficult to capture such extremely local (in space and time) impacts numerically with reasonable computational effort. But improvements to the code gave better results in the following years: The importance of taking into account two phases and furthermore of modeling the compressibility of the air phase correctly was shown by Wemmehove et al. (2007). The improved numerical code COMFLOW was validated by pressure measurements from sloshing model tests at a scale of 1:10. In order to track the free surface accurately, an improved volume of fluid method (iVOF) was applied. It was also shown that artificial viscous damping of the air phase related to first-order upwind discretization leads to underestimated wave heights especially close to tank walls if the cells are not fine enough.

Peric and Zorn (2005) and Peric et al. (2007) were among the first to present an integrated method based on the commercial solver STAR-CCM that is capable to simulate the entire process at once: In a transient three-dimensional simulation, the wave-induced motions of a LNG carrier with partially filled tanks are calculated, taking account of the bidirectional coupling effects between free fluid motions in the cargo tanks and vessel motions. In the same computational procedure, it is possible to obtain local pressures on the internal tank walls. However, due to the high computational effort of this method, only selected cases such as extreme wave encounters can be analyzed in time domain.

The importance of structural response analyses of internal tank walls and foundations under sloshing conditions is shown by Graczyk and Moan (2009). The insulation of a *Technigaz Mark III* tank typically consists of plywood and foam layers covered with a thin metallic membrane that are attached to the tank steel plates. A finite element method is developed to investigate the flexibility and resulting stresses in the insulation layers. It is shown that different layers contribute different modes to the overall response, e.g. plywood modes are relevant for short load durations whereas steel plate modes become relevant for longer load durations.

Local pressure impacts and their structural effects are not covered by the work presented in this thesis. Instead, the focus of research lies on coupling effects of internal tank sloshing and vessel motions. Individual parts of this aspect of the marine sloshing problem have also been studied by several researchers, and the discussion whether numerical methods for investigating sloshing have to be non-linear or a linear approach is sufficient is still vivid.

**Seakeeping**

In order to simulate the coupling process, Rognebakke and Faltinsen (2001) validated a numerical procedure where a linear strip theory approach for calculating ship motions is coupled to an adaptive nonlinear multimodal method as well as to a linear method to predict internal sloshing with 'two-dimensional model tests' using a rectangular ship section equipped with two box-shaped internal tanks. The model is allowed only to perform sway motions and is exposed to regular beam seas. It was found that for small to medium sloshing amplitudes linear theory shows good agreement with experiments while for stronger sloshing motions, the nonlinear multimodal approach is capable of predicting associated shiftings in the natural sloshing modes. In order to extend the applicability of the adaptive multimodal method for irregular waves Rognebakke and Faltinsen (2003) introduced a convolution formulation with a retardation function to the coupled equations of motion.

Molin et al. (2002) proposed a linear modal approach (except for quadratic viscous roll damping and internal tank damping formulations) based on *Pricipia's* code DIODORE to account for coupling effects between sloshing and ship motions. For validation purposes, a barge model was equipped with two rectangular tanks and was exposed to beam seas. Vessel motions as well as internal fluid motions were measured for altogether six different filling level combinations and wall roughnesses. Except for very low filling levels where nonlinear effects are dominant, good agreement of linear theory and model tests was achieved. Also, the first even sloshing mode, which was observed during experiments could not be reproduced by the linear theory since even modes are not directly coupled to the motion of the vessel. Further experiments by Molin et al. (2008) with the same barge model included the systematical analysis of roof impact for flat and chamfered tank roof geometries with different airgaps and wave heights. A general damping of sloshing effects on ship motions was observed for roof impacts, but varying airgaps lead to almost identical results despite different roof impact intensities. For moderate sloshing and roof impact good agreement of linear theory and model tests was observed.

A linear potential theory method that takes into account coupling of internal free fluid surface effects and ship motions is introduced by Malenica et al. (2003) and was found to give good results in comparison with Molin's barge model tests.

Bunnik and Veldman (2010) also used Molin's benchmark data to compare results obtained by a linear diffraction tool and a hybrid analysis method where the wave induced ship motions are determined by the linear tool which is coupled to MARIN's CFD solver COMFLOW. The results presented for the hybrid approach showed slightly better agreement with the experimental data than the purely linear calculations.

The description of the state-of-the-art in sloshing analyses at *Bureau Veritas* published by Zalar et al. (2006) and Zalar et al. (2007) reveals that the standard analysis procedure is based on the linear potential theory in-house code HYDROSTAR. When correct modeling of the free surface contour inside the tanks is required, a hybrid approach based on the coupling of HYDROSTAR for seakeeping and the CFD code FLOW-3D for internal fluid motions is applied.

*American Bureau of Shipping* (ABS) also published a number of papers related to the coupling of sloshing and seakeeping. Lee et al. (2005) presented a numerical approach where the ship motions are calculated by a potential theory approach based on MARIN's PRECAL and the fluid motions inside the tanks are computed by the finite-element method SLOFE2D in time domain. It was found that despite increasing LNGC and tank sizes with corresponding sloshing loads, current safety regulations are still conservative. Instead of SLOFE2D, Kim et al. (2006) and Lee et al. (2007) coupled a RANSE based solver with PRECAL to account for internal tank sloshing in time domain. Results are compared to model tests data as well as results obtained by a potential theory approach in frequency domain for both, external and internal flow computations. It was found that time domain results agree well with simulations and frequency domain results predict all effects at least qualitatively. Analyses of a LNGC and a FLNG terminal in side-by-side configuration obtained with the same hybrid approach were presented by Lee et al. (2008). Finally, Kim and Shin (2008) proposed a frequency domain approach to take account of coupled seakeeping for LNGC at forward speed. In all ABS publications, experimental results from the joint-industry project SALT (Seakeeping of structures Affected by Liquid Transient) obtained at MARIN have been used for validation.

In the framework of the project SALT, model tests with a moored FPSO and a free floating LNG carrier have been conducted. As reported by Gaillarde et al. (2004), comparison of roll motion RAOs obtained by the potential theory code DIODORE and model tests showed good agreement. Some discrepancies for internal fluid surface elevations and resulting tank forces are shown.

Chen (2005) and Chen et al. (2007) proposed a set of methods that is suitable for analyzing all hydrodynamic issues related to offshore FLNG terminal design. Apart from a newly introduced second-order middle-field formulation for drift load and low-frequency wave load analyses, it is stated that the majority of effects in coupled sloshing/vessel motion analyses is covered by linear theory (except for resonant phenomena) where modified coefficients for stiffness, added mass and — if dissipation is to be considered — for damping have to introduced to the equations of motion.

Finally, the method proposed by Newman (2005), which is based on the linear potential theory code WAMIT (Wave Analysis at Massachusetts Institute of Technology) is the basis for all analyses presented within this

work. A detailed description of the theoretical background for this method is given in the following chapter.

### 1.4.2 Multi-Body Effects

Two or more bodies floating in proximity in waves experience interactions, since each structure induces scattering (deflection and reflection of the incident wave field) and radiation (wave generation caused by the moving structure) wave fields. One of the first publications related to these effects is by Ohkusu (1976), who derived the coupled equations of motion and hydrodynamic coupling forces for a ship floating close to a simplified offshore structure and achieved good agreement of model test data and calculations. For larger structures that have to be discretized, van Oortmerssen (1979) extended the three-dimensional panel method to enable the investigation of multiple floating and hydrodynamically interacting bodies.

An alternative approach for axisymmetric structures is the multiple-scattering method, which solves the scattering problem for each body in the presence of other bodies by applying Graf's theorem to expand the respective potential of one body to the local coordinate systems of the other bodies. This method was applied by Chakrabarti (1999) to determine interactions between various structures in waves.

Newman (2001) presented the capabilities of the linear potential theory code WAMIT to take into account scattering and radiation effects leading to first and second order hydrodynamic interactions as well as resonant effects between two vessels. On the basis of WAMIT calculations, Clauss and Jacobsen (2004) investigated the hydrodynamic interaction between a large floating crane vessel and a barge during the lift-off procedure from the barge deck in frequency domain and proposed the F2T approach to transfer the relative motions between the two vessels to time domain.

In this thesis, the multi-body problem (interaction and relative motions between FLNG terminal and LNGC in tandem configuration) is also solved on basis of the linear potential theory code WAMIT.

### 1.4.3 Summary

For multi-body analyzes, reliable and validated methods such as potential theory or multiple-scattering theory for axisymmetric bodies are available. For all multi-body calculations in this thesis, WAMIT is used, which is based on linear potential theory.

Sloshing in partially filled internal tanks causes high pressure peaks with related structural loads on tank walls — especially in the region of geometrical discontinuities. In order to avoid damage and leakage, these effects have to be studied in detail. Typically methods include model tests where the sloshing-induced pressure peaks are measured for a detached tank (fresh

water filling) moving in six degrees of freedom on a hexapod. In the published numerical investigations, the two-phase flow in detached tanks are commonly analyzed by RANS methods, in some studies the SPH formulation is applied. However, the structural issues associated with tank sloshing are not covered by this thesis.

Instead, the focus lies on coupling effects between internal tank sloshing and the seakeeping behavior of the LNGC. Due to safety reasons, model tests are exclusively conducted with fresh water filling instead of LNG. Validated numerical methods that cover the coupling effects include linear, nonlinear and hybrid approaches such as the modal method, multimodal method, potential theory and RANS based methods. From the available published studies, it becomes clear that so far, idealized setups were considered. The model tests by Rognebakke and Faltinsen (2001), Molin et al. (2002) and Molin et al. (2008), that are widely used for validation purposes were conducted with rectangular tanks mounted to a rectangular barge hull. They have to be considered as 'two-dimensional model tests'. Published numerical studies also cover ship-shaped LNGC hulls but focus on two-dimensional responses in beam seas ($\beta = 90°$). An actual three-dimensional numerical approach that covers and explains all hydrodynamic influences during an offshore offloading procedure is not available so far.

In order to analyze offshore operations where coupling between fluid sloshing and vessel motions has to be considered, idealized assumptions and fresh water results are not meaningful. This is an explicit consequence of the two main phenomena that have not been explained or even identified by the research work published so far, but are investigated in detail in this thesis:

- the shift of the resonant motion peak related to the first natural sloshing mode and
- the occurrence of asymmetric fluid and vessel motion responses for symmetric excitations.

Bunnik and Veldman (2010) explicitly mentioned the shift of the resonant response peak, but simply attributed it to the large variations in tank added mass in this frequency range, which is no satisfactory explanation of this phenomenon. Observations and investigations of the asymmetric responses have not been published at all so far.

For the first time, a holistic approach that covers all relevant hydrodynamic effects for offshore offloading procedures, including multi-body interaction as well coupling of internal tank sloshing and vessel motions in dependency of the incident wave angle and the tank filling height is presented in this thesis. The proposed procedure eventually reduces this complex four-dimensional problem to a single curve that characterizes the offloading procedure in terms of tolerable sea states (combinations of significant wave

height $H_s$ and zero-upcrossing period $T_0$). The theoretical background for the numerical method is provided in the following chapter 2.

# Chapter 2

# Description of the Numerical Method

This chapter provides the theoretical background for the proposed holistic approach to assess offshore LNG transfer operations. At first, a brief overview on the basics of potential theory is given, followed by the determination of linear hydrodynamic forces and motions and an explanation of the influence of internal free fluid surfaces on the hydrodynamic coefficients in the equation of motion. Finally, the equations for the spectral stochastic analysis are compiled and the inclusion of viscous damping effects in the linear model is discussed.

The emphasis of the analyses presented in this thesis lies on dynamic effects caused by free fluid surfaces and multi-body interactions. The investigations and results focus on first order motions, i.e. motions that cannot be compensated by moorings. Effects of the six lines between LNGC and FLNG terminal are neglected, the same applies for the turret mooring of the FLNG terminal, which is only briefly addressed by an excursion on slow drift motion amplitudes due to second order wave forces. All results presented are valid for a water depth of 100 m. The numerical calculations are conducted in frequency domain, and are based on the specially adopted radiation-diffraction panel code WAMIT (Wave Analysis at Massachusetts Institute of Technology, WAMIT Inc. (2006)), which is a linear potential theory approach (see Newman (1977), Clauss et al. (1992) and Thamsen and Siekmann (2009)). The subsequent brief explanations provide the theoretical background of the numerical method.

## 2.1 Potential Theory

In this section, the flow around an arbitrarily shaped body in an ideal fluid with free surface in restricted water depth is considered. The structure is exposed to long-crested waves (incident wave field) characterized by the

wave frequency $\omega$, the wave number $k$ and the wave amplitude $\zeta_a$ (i.e. the wave height $H = 2\ \zeta_a$). The flow domain of interest is denoted by $V$ and is bounded by the sea bed $S_B$, the wetted body surface $S_b$ and the free water surface $S_f$ ($z = 0$ represents the still water level). The far field boundary $S_\infty$ is assumed to be a vertical circular cylinder. For the geometrical description of the structure, a cartesian coordinate system is used with the positive $z$-axis pointing upwards and orthogonal to $S_f$ and the positive $x$-axis pointing in the direction of wave propagation. A defined point on the body surface is described by the position vector $\underline{r}$ (note that underlined parameters represent vectors and column matrices, respectively) and the normal vector $\underline{n}$ always out of the fluid domain.

A structure is considered to be hydrodynamic compact, if its characteristic dimension $D$ is greater than 20% of the wave length $L$ (i.e. $D/L > 0.2$). Incident waves are significantly altered by these structures. In this case, the forces resulting from scattering and radiation (together: diffraction) of the incident waves can not be neglected. Since viscous effects play a minor role when analyzing hydrodynamical compact structures (Exception: Viscous effects considerably contribute to the damping of roll motions), excitation forces, added masses and potential damping can be calculated using potential theory.

The flow potential $\Phi$ (in the domain $V$) around the body has to be known. It has to satisfy Laplace's differential equation:

(*i*) *Laplace's equation* in $V$

$$\Delta\Phi = 0 \tag{2.1}$$

which is derived from the condition that the flow has to be irrotational

$$\underline{\nabla} \times \underline{v} = \underline{\nabla} \times (\underline{\nabla}\Phi) = \underline{0} \tag{2.2}$$

and also has to satisfy the continuity equation (written here for incompressible fluids):

$$\underline{\nabla}^T \underline{v} = \frac{\partial u}{\partial x} + \frac{\partial v}{\partial y} + \frac{\partial w}{\partial z} = 0. \tag{2.3}$$

Furthermore, the following conditions on the boundaries of $V$ have to be taken into account for deriving $\Phi$:

(*ii*) *Linearized, generalized free surface condition* for $z = 0$, i.e. at the still water level $S_f$

$$\frac{\partial\Phi}{\partial z} - \frac{\omega^2}{g}\Phi = 0; \tag{2.4}$$

$\rightarrow$ the hydrodynamic pressure at the free surface equals the atmospheric pressure; no particle leaves the wave contour

(*iii*) *Bottom condition* for $z = -d$, i.e. on the sea bed $S_B$ at water depth $d$

$$\frac{\partial \Phi}{\partial z} = 0; \tag{2.5}$$

$\rightarrow$ no flow through the sea bed

(*iv*) *Body condition* on the wetted body surface $S_b$

$$\underline{\dot{s}}^T \underline{n} = \frac{\partial \Phi}{\partial n}. \tag{2.6}$$

$\rightarrow$ the component of the fluid motion normal to the body surface equals the respective body motion component, i.e. there is no flow through the wetted body surface

The necessity of boundary conditions (2.4), (2.5) and (2.6) is obvious. But these conditions alone are not sufficient for a well-defined description of the problem. No boundary condition describing the far field of $V$ in great distance to the body has been set up so far. Hence, it is not defined whether the generated waves propagate away from or towards the body. Mathematically speaking, both cases are possible. But from the physical point of view, a *perpetuum mobile* would be created if the diffraction and radiation waves propagate towards the body that generated them. Therefore, an additional condition is required in order to model the problem:

(*v*) *Sommerfeld radiation condition*:

$$\lim_{R \to \infty} \sqrt{R} \left( \frac{\partial \Phi_j}{\partial R} - ik\Phi_j \right) = 0 \qquad\qquad j = 1, ..., 7 \tag{2.7}$$

where $R$ is the radius of the fluid domain. Assuming a linear problem, the total potential $\Phi$ is defined as a superposition of various wave systems and their potentials, respectively (Newman (1977)):

$$\Phi = \Phi_0 + \sum_{j=1}^{6} \Phi_j + \Phi_7 \tag{2.8}$$

The potential $\Phi_0$ describes the incident wave field, i.e. the undisturbed wave flow of the far field. Usually, this potential is known, e.g. from the linear wave theory (see Clauss et al. (1992)):

$$\Phi_0 = \frac{\zeta_a \, g}{\omega} \, \frac{cosh[k(z+d)]}{sinh(kd)} cos(\theta) \tag{2.9}$$

where the wave number $k$ can be derived from the dispersion relation

$$\omega = \sqrt{kg \, tanh(kd)} \tag{2.10}$$

The scattering potential $\Phi_7$ describes the wave field caused by scattering — i.e. the reflection and deflection of the incident waves by the structure. The radiation wave field due to body motions in six degrees of freedom $j \in [1,6]$ is described by a sum of altogether six potentials. When the body moves in direction $j$, it generates a wave field with the corresponding potential $\Phi_j$. These six potentials can be split into the six center of gravity velocities of the body $\underline{\dot{s}} = (\dot{s_1}, \dot{s_2}, ..., \dot{s_6})$ and the corresponding *local body potentials* $\varphi_j$

$$\Phi_j = \dot{s}_j \varphi_j \qquad j = 1, 2, ..., 6 \tag{2.11}$$

where $j$ denotes the translatory motions surge (1), sway (2), and heave (3) as well as the rotatory motions roll (4), pitch (5) and yaw (6). All potentials that solve the hydrodynamic problem have to satisfy Laplace's equation (2.1) as well as boundary conditions (2.4) to (2.6). For a well-defined solution, potentials $\Phi_j$ ($j$ = 1,2,. . . , 6) and $\Phi_7$ additionally have to satisfy the Sommerfeld radiation condition (2.7).

The boundary problem briefly stated above is solved by applying *Green's second identity*

$$\iiint_V [\Phi(\Delta G) - G(\Delta\Phi)]\, dV = \iint_S \left(\Phi \frac{\partial G}{\partial n} - G\frac{\partial \Phi}{\partial n}\right) dS \tag{2.12}$$

to derive integral equations for the radiation and diffraction potentials on the body boundary. The Green function $G(\underline{x}, \underline{\xi})$ is referred to as the wave source potential — the velocity potential at the point $\underline{x}$ due to a point source of strength -4$\pi$ located at the point $\underline{\xi}$.

The solution that for the local radiation body potentials $\varphi_j$ gives

$$2\pi\varphi_j(\underline{x}) + \iint_{S_b} \varphi_j(\underline{\xi}) \frac{\partial G(\underline{x}, \underline{\xi})}{\partial n}\, dS_b \;=\; \iint_{S_b} G(\underline{x}, \underline{\xi}) \frac{\partial \varphi_j(\underline{\xi})}{\partial n}\, dS_b \qquad j = 1, ..., 6. \tag{2.13}$$

The corresponding solution for the scattering potential $\Phi_7$ is

$$2\pi\Phi_7(\underline{x}) + \iint_{S_b} \Phi_7(\underline{\xi}) \frac{\partial G(\underline{x}, \underline{\xi})}{\partial n}\, dS_b \;=\; \iint_{S_b} G(\underline{x}, \underline{\xi}) \frac{\partial \Phi_7(\underline{\xi})}{\partial n}\, dS_b \tag{2.14}$$

The potential of the incident wave field $\Phi_0$ and the scattering potential $\Phi_7$ are combined in the total diffraction potential $\Phi_D$. For this potential, an integral equation with simplified right-hand side can be set up:

$$2\pi\Phi_D(\underline{x}) \;+\; \iint_{S_b} \Phi_D(\underline{\xi}) \frac{\partial G(\underline{x}, \underline{\xi})}{\partial n}\, dS_b \;=\; 4\pi\Phi_0(\underline{x}) \tag{2.15}$$

In WAMIT, body surfaces have to be discretized by a finite number of quadrilaterals or panels. The radiation as well as the diffraction velocity potentials are assumed to be constant over each panel.

## 2.2 Hydrodynamic Forces and Motions

The total dynamic force acting on a submerged body in waves results from the integration of the dynamic pressure over the wetted body surface $S_b$:

$$\underline{F}_{dyn} = \iint\limits_{S_b} p_{dyn}\, \underline{n}\, dS_b \tag{2.16}$$

where the dynamic pressure is defined according to Bernoulli's equation

$$p_{dyn} = -\rho \frac{\partial \Phi}{\partial t} \tag{2.17}$$

and can thus be split into three components in analogy to the potential $\Phi$ (cf. Eq. (2.8)):

$$p_{dyn} = -\rho \left( \frac{\partial \Phi_0}{\partial t} + \frac{\partial \Phi_7}{\partial t} + \sum_{j=1}^{6} \ddot{s}_j \varphi_j \right) \tag{2.18}$$

resulting in internal and external (or excitation) forces:

$$\underline{F}_{dyn} = \underbrace{-\rho \iint\limits_{S_b} \left( \frac{\partial \Phi_0}{\partial t} + \frac{\partial \Phi_7}{\partial t} \right) \underline{n}\, dS_b}_{F_{ex},\ \text{excitation force}} \quad - \quad \underbrace{\rho \iint\limits_{S_b} \ddot{s}_j \varphi_j \underline{n}\, dS_b}_{F_{int,dyn},\ \text{dynamic internal force}} \tag{2.19}$$

where the dynamic internal force is depending on the added mass $a_{ij}$ and potential damping coefficients $b_{ij}$:

$$\rho \iint\limits_{S_b} n_i \varphi_j \, dS_b = a_{ij} - \frac{i}{\omega} b_{ij} \tag{2.20}$$

Forced changes in a body's buoyancy, e.g. induced by varying submerged depths $z$, lead to a hydrostatic restoring force, which is the second internal force component to be considered:

$$\underline{F}_{int,stat} = -\rho\, g \iint\limits_{S_b} \underline{n}\, z\, dS_b = \underline{C}\, \underline{s} \tag{2.21}$$

According to Newton's second law, the equilibrium of internal and external forces on the submerged body finally gives the equation of motion, from which the body motion $s_j$ can be determined:

$$\sum_{j=1}^{6} \left[ -\omega^2 \left( m_{ij} + a_{ij} \right) + i\omega b_{ij} + c_{ij} \right] \; s_j = f_{ex,j} \tag{2.22}$$

In the following, the relevant hydrodynamic coefficients to solve this equation are briefly introduced:

- *added mass/potential damping*: The added mass $a_{ij}$ as well as the potential damping $b_{ij}$ are evaluated from the local body potentials $\phi_j$ with the following relation, already introduced in Eq. (2.20):

$$a_{ij} - \frac{i}{\omega} b_{ij} = \rho \iint_{S_b} n_i \varphi_j \, dS_b \tag{2.23}$$

- *restoring coefficients*: hydrostatic restoring $c_{ij}$ is exclusively related to heave, roll and pitch motions (except for external moorings).

$$\underline{C} = \begin{bmatrix} 0 & 0 & 0 & 0 & 0 & 0 \\ 0 & 0 & 0 & 0 & 0 & 0 \\ 0 & 0 & c_{33} & c_{34} & c_{35} & 0 \\ 0 & 0 & c_{43} & c_{44} & c_{45} & c_{46} \\ 0 & 0 & c_{53} & c_{54} & c_{55} & c_{56} \\ 0 & 0 & 0 & 0 & 0 & 0 \end{bmatrix}$$

where

$$\begin{aligned} c_{33} &= \rho g \iint_{S_b} n_3 dS_b \\ c_{34} = c_{43} &= \rho g \iint_{S_b} y n_3 dS_b \\ c_{35} = c_{53} &= -\rho g \iint_{S_b} x n_3 dS_b \\ c_{44} &= \rho g \iint_{S_b} y^2 n_3 dS_b + \rho g \forall z_b - m g z_g \\ c_{45} = c_{54} &= -\rho g \iint_{S_b} x y n_3 dS_b \\ c_{46} &= -\rho g \forall x_b + m g x_g \\ c_{55} &= \rho g \iint_{S_b} x^2 n_3 dS_b + \rho g \forall z_b - m g z_g \\ c_{56} &= -\rho g \forall y_b + m g y_g \end{aligned} \tag{2.24}$$

## 2.3 Internal Tank Effects

The introduced numerical method is capable of capturing the effects of coupling between internal liquid motions and rigid body motions of the LNGC.

The computational domain consists of an external and a specified number of internal fluid domains, which constitute one global boundary surface but the respective potentials are independent and do not influence each other. For the internal tank domain, diffraction effects are neglected (no incident waves, no scattering) and according to the formulation in Eq. (2.11), the velocity potential of each tank gives (Newman (2005)):

$$\Phi_T = i\omega \sum_{j=1}^{6} s_j \, \varphi_{T,j} \tag{2.25}$$

where $s_j$ is the body motion in the $j^{th}$ direction and $\varphi_{T,j}$ the corresponding local tank potential.
At first, hydrostatic parameters are evaluated separately for the hull (at its actual draft but without the influence of the liquid cargo in the mass matrix) and the tanks. Subsequently, restoring coefficients, added mass and damping are combined as follows:

- *restoring coefficients*:
  Free fluid surfaces can be considered as a reduction of the vessel's waterplane area. Contributions from the tanks are added to the restoring coefficients of the hull, e.g. the total heave restoring coefficient becomes $c_{33} = c_{33} + \sum c_{33,T}$. The calculation of the tank restoring coefficients is analogous to Eq. (2.24), with $\rho{=}\rho_T$ being the density of the internal fluid. Due to the inverse orientation of the fluid boundaries, there is no positive restoring force for the tanks, hence the respective contributions are negative and reduce the total restoring coefficients. As

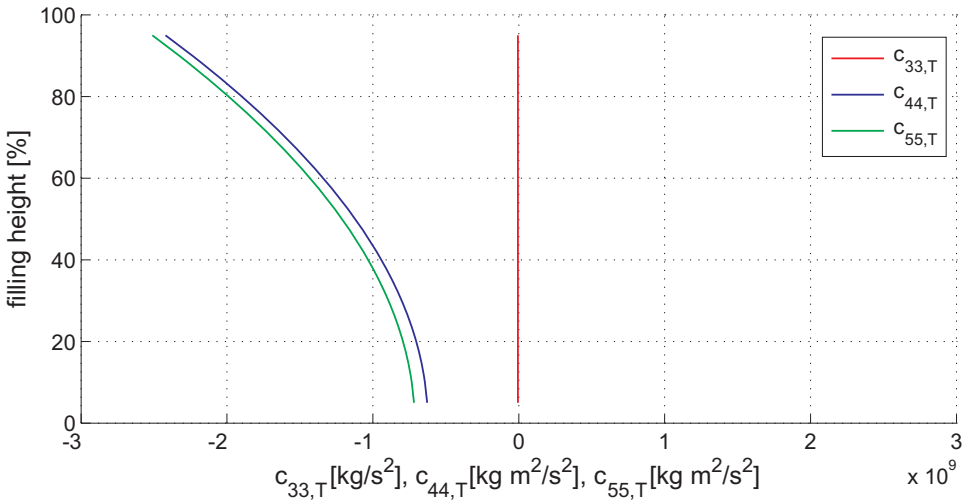


Figure 2.1: *Cuboid tank restoring coefficients $c_{33,T}$, $c_{44,T}$ and $c_{55,T}$ depending on the filling height*

shown in Fig. 2.1 for a cuboid tank (length 38.3 m, width 35.8 m, height 26.1 m), the negative magnitudes of the restoring coefficients increase with increasing filling height except for $c_{33,T}$ which remains constant for all filling conditions. The effect of multiple cargo tanks mounted to a ship hull is exemplarily calculated for the heave restoring coefficient of the MPLS20 LNGC: The hull restoring coefficient in fresh water ($\rho = 998.2\ \frac{kg}{m^3}$) is $c_{33} = 9.59 \times 10^7\ \frac{kg}{s^2}$ and each of the four prismatic tanks (with 30% fresh water filling) contributes $c_{33,T} = -1.34 \times 10^7\ \frac{kg}{s^2}$, resulting in a total heave restoring coefficient $c_{33} = c_{33} + 4 \cdot c_{33,T} = 4.23 \times 10^7\ \frac{kg}{s^2}$.

- *added mass coefficients*:
  Added mass effects can be observed when submerged bodies are subjected to a transient pressure field caused by relative accelerations between fluid and structure. In the case of internal tanks, this also includes relative accelerations between tank walls and the internal fluid. The respective coefficients are evaluated globally by integration of the pressure force over the total wetted body surface, including tank walls where $\rho$ is replaced by $\rho_T$ (see Eq. (2.23)). Only the coefficients for the vertical modes heave, roll and pitch require special adaptations, because a 'fictitious hydrostatic contribution' (WAMIT Inc. (2006)) has to be considered. This adaptation takes into account that the free surface effects on the restoring coefficients are evaluated with respect to the global origin and not to the local centroid of the free surface area as in the classical hydrostatic approach. For example, the heave added mass contribution from the internal tank domain becomes:

$$a_{33,T} = \rho_T \iint_{S_T} n_3\, \varphi_{T,3}\, dS_T = \rho_T \forall_T + \frac{1}{\omega^2} c_{33,T} \tag{2.26}$$

  where the last term is canceled out by the hydrostatic restoring coefficient for very low wave frequencies, i.e. there is no tank contribution for the limit $\omega \to 0$. The added mass characteristics of a tank alone give information on the odd natural modes. All even modes, like the second sloshing mode, are caused by non-linear wave-wave interaction and are therefore not computable by the chosen linear potential theory approach (Malenica et al. (2003)). But since the free surface elevations inside the tank are symmetric for even modes (see Fig. 2.3), there are no coupling effects with the ship motions, i.e. they are not relevant in this context anyway. In Fig. 2.2, $a_{11,T}$ and $a_{22,T}$ are calculated for a detached cuboid tank (length 38.3 m, width 35.8 m, height 26.1 m), showing the first and third longitudinal and transverse mode for exemplary filling heights of 10%, 20% and 30%. In the frequency range below the first mode, the added mass caused by the pressure of the

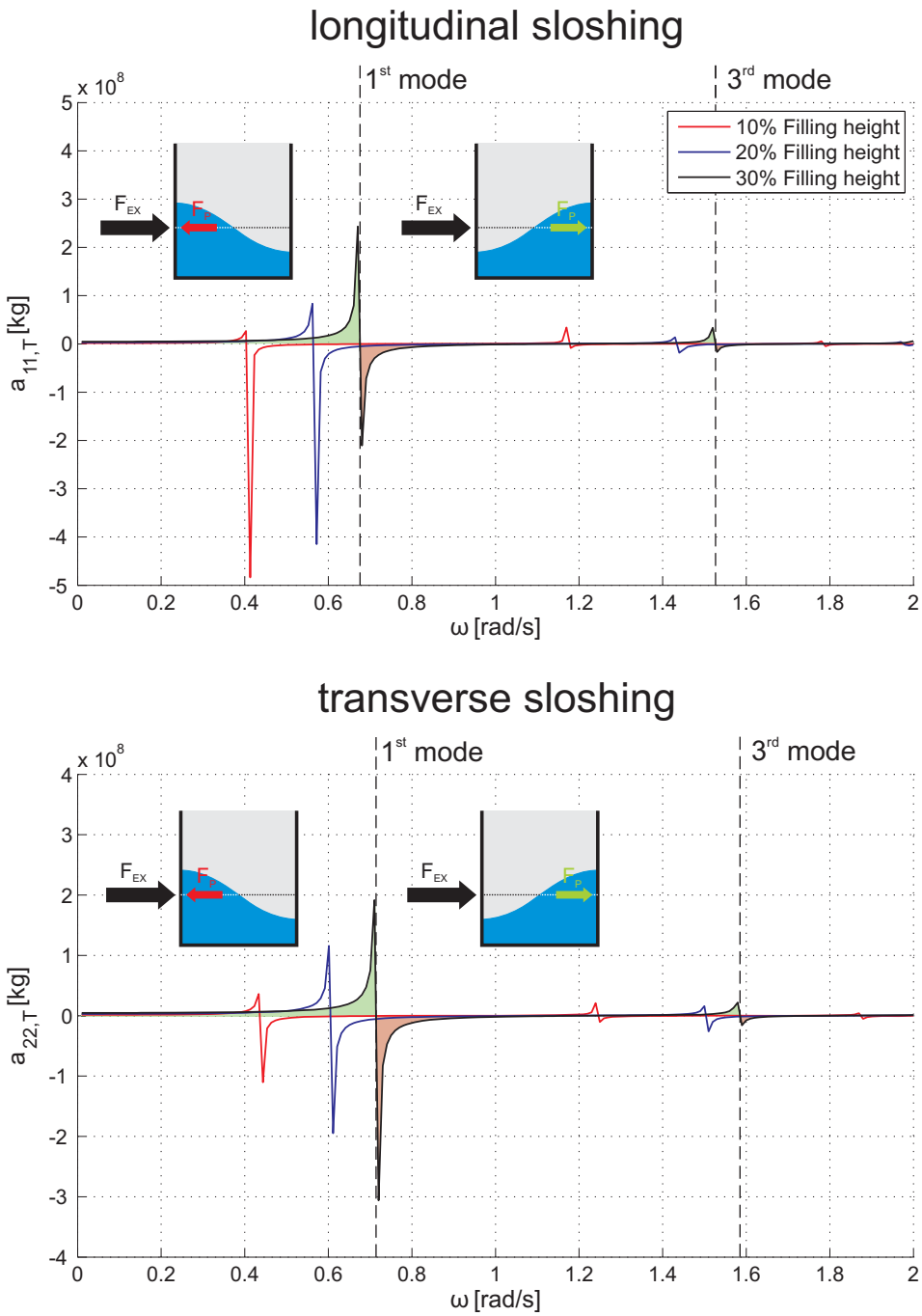


Figure 2.2: *Characteristics of the added masses $a_{11,T}$ (top) and $a_{22,T}$ (bottom) of the detached cuboid tank for exemplary filling heights of 10%, 20% and 30%*

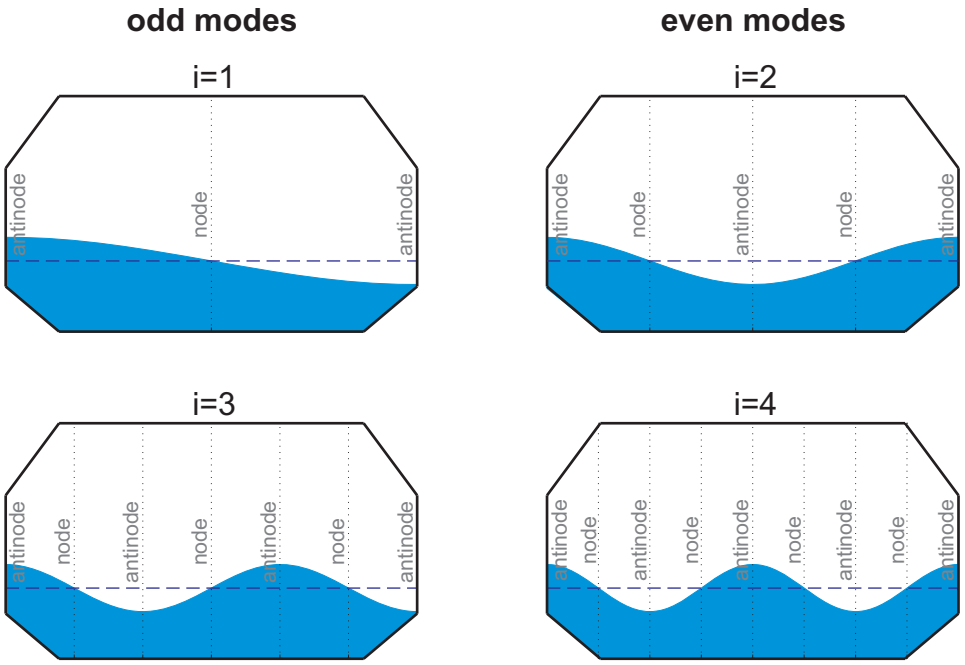


Figure 2.3: *Schematic visualization of the tank surface deflections at the first four sloshing modes*

accelerated fluid is positive (exemplarily indicated by the green area below the added mass for 30% filling height), while a phase shift in the fluid motions for the frequency range above the first mode results in negative added mass effects (exemplarily indicated by the red area below the added mass for 30% filling height). This effect is illustrated by a simplified system with indicated directions of forces for a excited partially filled container. Identical observations can be made for all other odd modes.

- *damping coefficients*:
  The moving walls of the internal tanks generate waves in the internal fluid. Since these waves are trapped and cannot propagate away from the system, no radiation with associated energy dissipation occurs. Therefore, the potential damping contribution of the internal tanks is zero.

According to Faltinsen and Timokha (2009), the natural transverse sloshing frequency of the i$^{\text{th}}$ mode for a rectangular tank is given by an expression based on the dispersion relation:

$$\omega_{r,i} = \sqrt{g \, \frac{\pi i}{B_T} \, tanh\left(\frac{\pi i}{B_T} h_f\right)} \tag{2.27}$$

where the respective filling height inside the tank is denoted by $h_f$ and the tank width by $B_T$. The natural frequency is not dependent on the density of the fluid inside the tank. For prismatic tanks with chamfered bottom, Faltinsen and Timokha (2009) proposed a correction factor:

$$\left(\frac{\omega'_{r,i}}{\omega_{r,i}}\right)^2 = 1 - \frac{\frac{\delta_1}{\delta_2}\, sinh^2\left(\frac{\pi i \delta_2}{B_T}\right) - \frac{\delta_2}{\delta_1}\, sin^2\left(\frac{\pi i \delta_1}{B_T}\right)}{\pi i\, sinh\left(\frac{2\pi i h}{B_T}\right)} \tag{2.28}$$

giving the percentaged deviation compared to rectangular tanks. $\omega'_{r,i}$ is the corrected natural frequency of the i$^{\text{th}}$ mode for prismatic tanks. The excitation of the lowest natural frequency of the liquid motion and its impact and coupling with ship motions is of primary interest. The wave lengths inside the tanks related to the first mode ($i = 1$) are about twice the respective characteristic tank dimension, i.e. $2{\cdot}B_T$ for $\beta = 90°$ and $2{\cdot}L_T$ for $\beta = 180°$, with a node in the tank center.

## 2.4 Operational Limitations

Due to the design and material properties of the transfer pipes, the crucial parameter for offshore offloading procedures is the relative motion of the coupling points of the LNG transfer system, i.e. the relative motion between FLNG terminal and LNGC. Once a maximum tolerable relative motion amplitude is established, the operational range of the FLNG system can be determined based on a linear stochastic approach.
At first the type of spectrum and associated range of peak periods has to be defined. Typical standard spectra include the Pierson-Moskowitz spectrum (Pierson and Moskowitz (1964)), e.g. the formulation recommended by the ITTC

$$S(\omega) = 490\, \frac{H_s^2}{T_P^4\, \omega^5}\, e^{-\frac{1955}{T_P^4\, \omega^4}} \tag{2.29}$$

which can be applied for analyses in the North Atlantic Ocean region. For the North Sea region, the JONSWAP spectrum — which accounts for the occurrence of steeper waves — can be applied, e.g. the formulation by Houmb and Overik (1976) which was extended by Wichers (1979) in order to ensure identical spectral areas — hence identical significant wave heights:

$$S(\omega) = \beta\, H_s^2\, \frac{\omega_p^4}{\omega^5}\, e^{-\frac{5}{4}\left[\frac{\omega_p}{\omega}\right]^4}\, \gamma^{B(\omega)} \tag{2.30}$$

where

$$\begin{aligned} \beta &= \frac{0.313}{F(\gamma)} \quad \text{with} \quad \begin{cases} F = 1 & \text{for} \quad \gamma = 1 \\ F = 1.52 & \text{for} \quad \gamma = 3.3 \end{cases} \\ B(\omega) &= e^{-\frac{(\omega-\omega_p)^2}{2\sigma^2\omega_p^2}} \\ \sigma &= \begin{cases} 0.07 & \text{for} \quad \omega \leq \omega_p \\ 0.09 & \text{for} \quad \omega > \omega_p \end{cases} \end{aligned}$$

The coefficient $\gamma$ represents the ratio of maximum values of JONSWAP to Pierson-Moskowitz spectra — i.e. for $\gamma = 1$, both spectra are identical. A typical value for the North Sea is $\gamma = 3.3$. The spectral shapes resulting from Eqs. (2.29) and (2.30) with $\gamma = 3.3$ are exemplarily compared for $H_s = 1$ m and $T_p = 10$ s in Fig. 2.4. Alternatively, sea spectra can be set up in dependency of the zero-upcrossing period $T_0$, which is related to the peak period by $T_0 = T_p/1.285$.

Once a set of suitable sea state spectra with an associated range of peak periods is established, the stochastic analysis begins with the determination of the desired response spectra $S_j(\omega, T_p)$ by multiplying the sea state spectra by the squared absolute value of the RAO of the $j^{\text{th}}$ mode $s_{j,a}(\omega)/\zeta_a$ (the procedure is illustrated for motions but can be applied analogously to

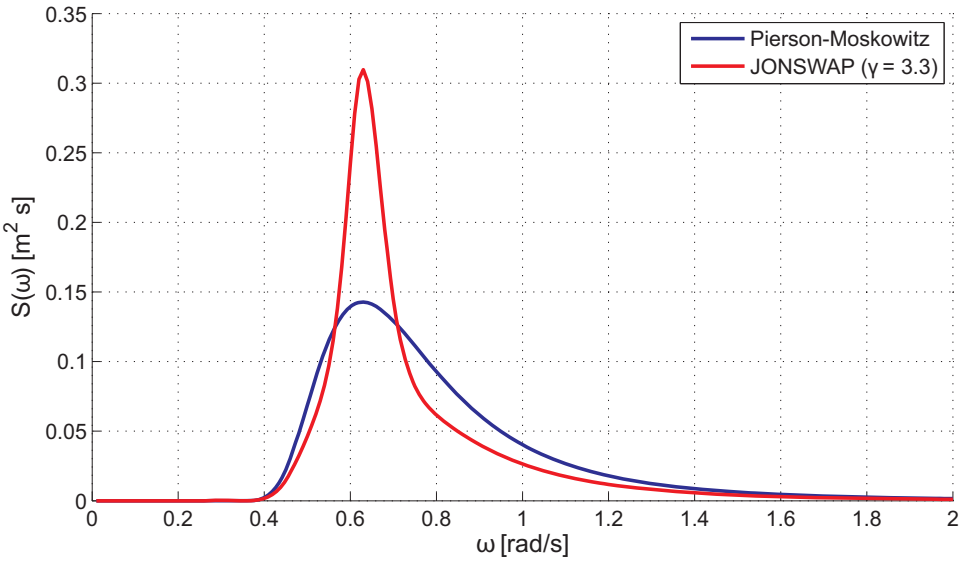


Figure 2.4: *Exemplary comparison of a Pierson-Moskowitz and a JONSWAP spectrum ($\gamma = 3.3$), both for $T_p = 10$ s and $H_s = 1$ m.*

velocities, accelerations, forces):

$$S_j(\omega, T_p) = |\frac{s_{j,a}(\omega)}{\zeta_a}|^2 \; S(\omega, T_p) \tag{2.31}$$

From the area enclosed by these response spectra, significant double amplitudes are determined:

$$(2s_{j,a})_s(T_p) = 4 \sqrt{\int_0^\infty S_j(\omega, T_p) d\omega} \tag{2.32}$$

Division by the significant wave height gives the desired significant RAO. For predefined maximum tolerable parameters, tolerable significant wave heights are calculated in dependency of the peak periods (assuming a statistical value of 1.86 for the ratio of tolerable maximum relative motions to tolerable significant relative motions):

$$H_{s,tol}(T_p) = (2s_{i,a})_{s,tol} \; \frac{H_s}{(2s_{i,a})_s(T_p)} \tag{2.33}$$

These limiting sea states can be transferred to a wave scatter diagram of the respective operational location. With the known frequencies of occurrence for each combination of $H_s$ and $T_p$ (or alternatively $T_0$), the operational range — or the annual downtime in days can be determined.

**Excursion: Statistical Maximum Values**

Theoretically, the wave height distribution of a narrowband sea spectrum is characterized by the Rayleigh distribution

$$\varphi_R(H) = \frac{2\,H}{H_{RMS}^2} \; e^{-\frac{H^2}{H_{RMS}^2}} \tag{2.34}$$

with the root mean square of the heights of all $N$ waves

$$H_{RMS} = \sqrt{\frac{1}{N} \sum_{j=1}^{N} H_j^2} \tag{2.35}$$

Since the significant wave height is the mean value of the 33% highest waves, it can be identified as the center of the area enclosed by the Rayleigh distribution above the limit $H_{33}$:

$$H_s = \frac{\int_{H_{33}}^\infty H \; \varphi_R(H) dH}{\int_{H_{33}}^\infty \varphi_R(H) dH} = 3 \int_{H_{33}}^\infty \frac{2\,H^2}{H_{RMS}^2} \; e^{-\frac{H^2}{H_{RMS}^2}} \tag{2.36}$$

This integral has to be solved numerically and yields

$$H_s \approx \sqrt{2}\, H_{RMS} \tag{2.37}$$

Assuming the maximum wave to be the wave height that is exceeded once in the chosen observation period, its probability of exceedance is

$$P(H \geq H_{max}) = 1 - \Phi_R(H_{max}) = e^{-\frac{H_{max}^2}{H_{RMS}^2}} = \frac{1}{N} \tag{2.38}$$

Solving Eq. (2.38) for $H_{max}$ gives

$$H_{max} = H_{RMS}\, \sqrt{ln(N)} \tag{2.39}$$

Substituting Eq. (2.37) finally gives the relation of $H_{max}$ to $H_s$

$$H_{max} = H_s \sqrt{\frac{ln(N)}{2}} \tag{2.40}$$

Typically, a standard value of $N = 1000$ waves is chosen which represents a three-hour storm with a mean wave period of 10 s. The standard relation is therefore

$$H_{max} = 1.86\, H_s \tag{2.41}$$

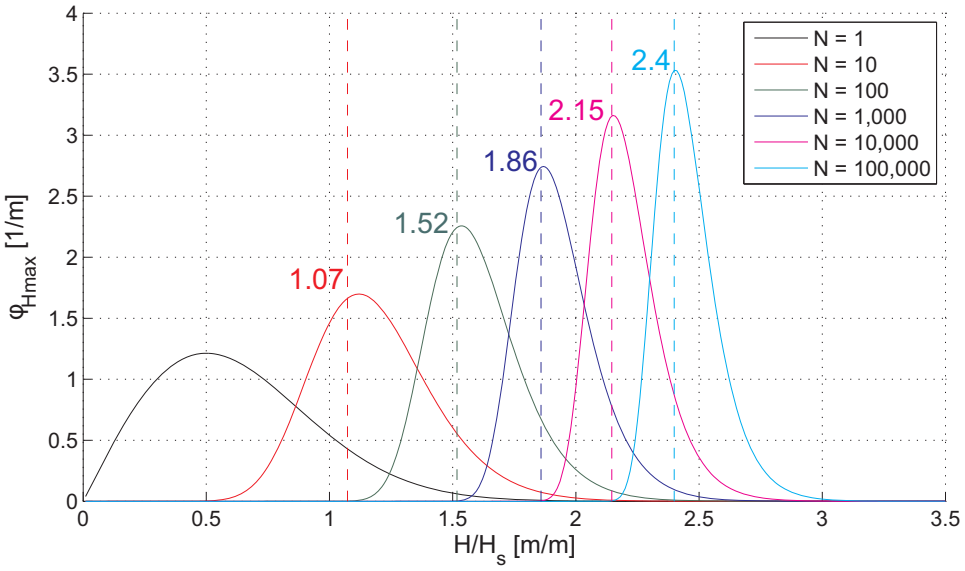


Figure 2.5: *Probability density distribution of the maximum wave height depending on the number of waves N in the observation period*

The associated probability density function

$$\varphi_{Hmax}(H) = N\left(1 - e^{-\frac{2\,H^2}{H_s^2}}\right)^{N-1} \frac{4\,H}{H_s^2}\, e^{-\frac{2\,H^2}{H_s^2}} \tag{2.42}$$

is shown in Fig. 2.5.

For $N = 1$ the function equals the Rayleigh distribution (see Eq. (2.34)) and for increasing wave numbers, the ratio of $H_{max}$ to $H_s$ increases. It can be observed that the values obtained from Eq. (2.40) approximately match the peaks of the probability density functions of the maximum wave height — the most probable maximum. According to Det Norske Veritas (2011), the ratio $H_{max}/H_s$ can be expressed as

$$H_{max}/H_s = \sqrt{\frac{ln(N)}{2}\left(1 - \frac{ln(-ln(p))}{ln(N)}\right)} \tag{2.43}$$

where the $p$ is the cumulative probability function — the probability for a sea state with $N$ waves that $H/H_s$ is less than or equal to a certain value $H_{max}/H_s$. For $N$=1000, $p = 0.5$ yields the median value $H_{max}/H_s = 1.91$, which is equivalent to the centroid of the area enclosed by the probability density function of the maximum wave height. The common value $H_{max}/H_s = 1.86$ is associated with $p = 0.372$, i.e. the probability of exceedance is 62.8%. In order to ensure a very low probability of exceedance, e.g. 1%, $H_{max}/H_s = 2.4$ has to be chosen for $N$=1000 waves. However, the calculations presented in section 3.5.2 are based on the common assumption of the most probable maximum ($H_{max}/H_s = 1.86$ for $N$=1000 waves).

## 2.5 Damping

A body that moves in calm water radiates waves. Since the energy for generating these waves is taken from the kinematic energy, the motions of the structure are simultaneously damped. This phenomenon is referred to as potential damping, an effect which is accounted for in the applied diffraction-radiation code.

Viscous damping effects have to be taken into account in order to obtain realistic resonant responses for all degrees of freedom where restoring forces arise (i.e. heave, roll and pitch). Since viscous damping as well as the resonant vessel responses are highly non-linear with respect to the motion amplitude, the following procedure to modify the linear approach has to be regarded as a good linear approximation.

Roll and pitch decay tests at model scale are conducted, where the model is typically moored with a mass-spring arrangement in calm water. After a moderate initial deflection in the desired degree of freedom, the decay of the vessel motions is measured. The measured roll decay of the MPLS20 LNGC is exemplarily shown in Fig. 2.6.

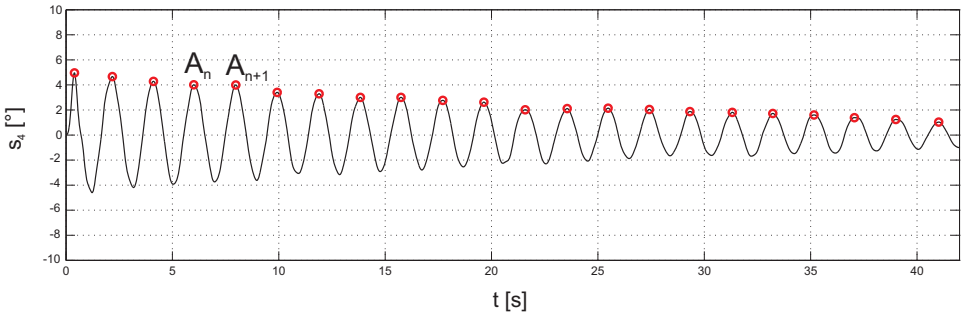


Figure 2.6: *Exemplary roll decay measurement of the MPLS20 LNGC*

The measured damping $b_{m,ij}$ — which is the total damping, since it includes all effects — is determined by

$$b_{m,ij} = \delta \; b_{c,ij} \tag{2.44}$$

where $b_{c,ij}$ is the critical damping (the deflected vessel returns to its initial position without oscillation)

$$b_{c,ij} = 2 \; (m_{ij} + a_{ij}) \; \omega_{r,ij} \tag{2.45}$$

and $\delta$ the ratio of total (measured) damping to critical damping,

$$\delta = \sqrt{\frac{A_{mean}^2}{A_{mean}^2 + 4 \; \pi^2}} \tag{2.46}$$

which can be determined by the mean logarithmic decrement $A_{mean}$ of the decay measurement

$$A_{mean} = ln \left( \frac{A_n}{A_{n+1}} \right)_{mean} \tag{2.47}$$

with $A_n$ and $A_{n+1}$ being consecutive motion amplitudes (see also Fig. 2.6).

The viscous part ($b_{v,ij}$) of the total damping is determined by subtracting the potential damping ($b_{ij}$) calculated by the potential theory code from the total damping ($b_{m,ij}$) determined by decay tests.

$$b_{v,ij} = b_{m,ij} - b_{ij} \tag{2.48}$$

Since the model tests do not take into account scaled viscosities (exclusively Froude-compliant), the total damping is overestimated compared to full scale values. Based on these results, an external viscous damping matrix is implemented in the numerical code.

In cases where no decay test results are available, recommendations for numerical estimations of the damping for the most critical degree of freedom — the roll motion — are provided by ITTC (2011).

# Chapter 3

# Hydrodynamic Challenges

Offshore LNG transfer poses several hydrodynamic challenges that have to be considered in order to ensure save operations. In this chapter, all relevant issues are explained in detail and calculations are exemplarily conducted for the offloading procedure of the MPLS20 system in 100 m water depth (dimensions of the involved vessels are listed in Tab. 1.2). First of all, it is shown how internal free fluid surfaces reduce the initial stability of the LNGC. After this introduction to static impacts, dynamic sloshing effects are discussed for detached tanks as well as tanks mounted to the LNGC hull.

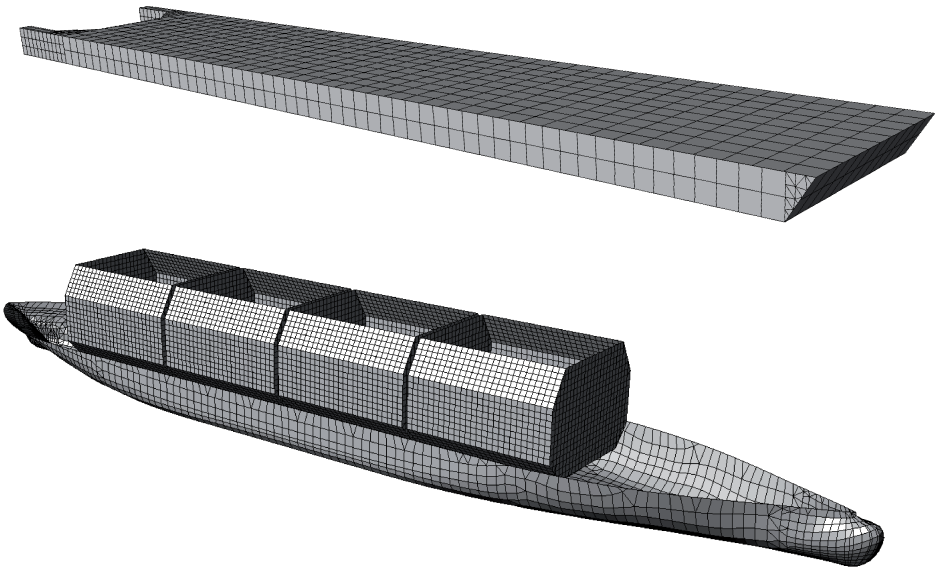

Figure 3.1: *Discretization of the FLNG terminal (top) and the LNGC (bottom)*

Here, the focus lies coupling effects between internal fluid motions and the vessel response in waves. In-depth studies reveal resonant peak shifts and asymmetric effects and the consequences are discussed. During the approach of the LNGC to the FLNG terminal and in particular during the loading phase, alterations of the seakeeping behavior due to multi-body effects are studied. On basis of the data set obtained with the holistic numerical approach, a classical stochastic analysis yields the operational range of the MPLS20 system for the *Haltenbanken* region. The chapter concludes with excursions to exemplary variations of the system configuration and FLNG mooring considerations.

As shown in Fig. 3.1, the submerged part of the FLNG terminal hull is discretized by a total of 1,716 panels and the LNGC by a total of 13,104 panels (submerged part of hull: 3,376 panels, tanks 4 x 2,432 panels). Due to the simple and continuous shape of the FLNG terminal, a relatively coarse panel resolution proved to be sufficient to capture all hydrodynamic effects, while the LNGC hull and in particular the tanks have to be represented by a finer grid in order to account for the coupling of internal fluid motions and seakeeping.

## 3.1 Initial Stability

When a ship is inclined by a small angle $\varphi$, a righting moment (product of buoyancy force and righting arm) arises, moving the vessel back to its equilibrium position. Free fluid surfaces aboard a ship lead to a decrease of the initial intact stability. With increasing inclination of the vessel, the liquid's resulting center of gravity shifts, which reduces the righting arm $h(\varphi)$. According to SNAME (1989b) a *free surface correction* procedure has to be performed, where the effect of the free surfaces leads to an increasing height of the vessel's center of gravity above keel $\overline{KG}$ and a related decrease of the initial metacentric height $\overline{GM_0}$

$$\overline{GM_0} = \overline{KB_0} + \overline{B_0M_0} - \overline{KG} \ , \tag{3.1}$$

respectively, which is considered to be a measure of the vessel's stability. Assuming small inclination angles $\varphi$, the free surface correction can be expressed by a shift of the center of gravity:

$$\overline{GG'} = \sum_{j=1}^{NT} \frac{I_j}{\forall} \frac{\rho_{T,j}}{\rho} \tag{3.2}$$

where the number of tanks with free surfaces is $NT$, $I_j$ is the second moment of area for each tank $I_j = (B_{T,j}^3 L_{T,j})/12$ and $\forall$ the submerged volume of the vessel. The corrected — i.e. reduced — metacentric height can now be written as

$$\overline{GM_{0_{corr}}} = \overline{KB_0} + \overline{B_0M_0} - (\overline{KG} + \overline{GG'}) \tag{3.3}$$

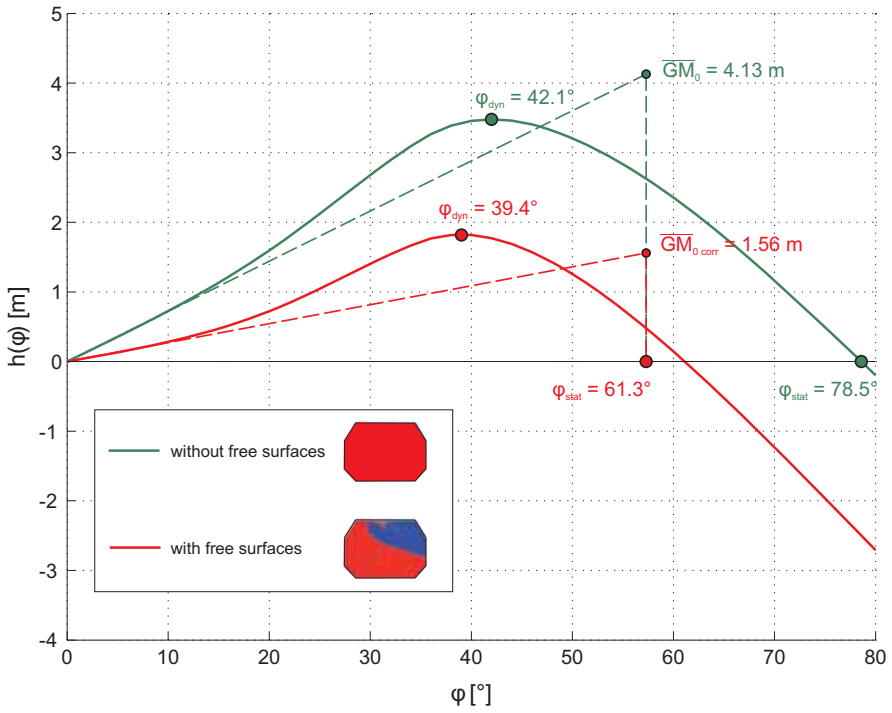


Figure 3.2: *Decrease of initial stability due to free fluid surfaces inside the LNGC's tanks (30% LNG filling height, $\rho_T = 435\ kg/m^3$)*

For larger inclination angles $\varphi$, the center of buoyancy shifts three-dimensional, which also affects the metacenter. The vertical line through the center of buoyancy now intersects with the vertical axis of symmetry at the prometacenter $N_\varphi$ — the formulation for the metacentric height according to Eq. (3.3) has to be extended by the additional stability term $\overline{M_0 N_\varphi}$ as well as an oscillatory term for $\overline{GG'}$:

$$\overline{GN_{\varphi corr}} = \overline{KB_0} + \overline{B_0 M_0} - (\overline{KG} + \overline{GG'}\, sin(\varphi)) + \overline{M_0 N_\varphi} \tag{3.4}$$

Based on Eq. (3.4), the righting arm $h_{corr}(\varphi)$ is expressed as an oscillation with the amplitude $\overline{GN_{\varphi corr}}$:

$$h_{corr}(\varphi) = \overline{GN_{\varphi corr}}\, sin(\varphi) \tag{3.5}$$

Fig. 3.2 shows the righting arm for the LNGC at solid filling condition (green line) compared a loading condition with four partially filled tanks (red line [30% LNG filling height, $\rho_T = 435\ kg/m^3$]). The initial metacentric height $\overline{GM_0}$ and $\overline{GM_{0corr}}$, respectively, can be determined from the starting tangent values at $\varphi = 1$ rad $\approx 57.3°$ at the axis of ordinate. The influence of the four tanks with free surfaces leads to a decrease of the metacentric height by 2.57 m. Also, the dynamic as well as the static capsize angles are reduced from 42.1° to 39.4° and 78.5° to 61.3°, respectively.

## 3.2 Sloshing

Liquids with free surfaces inside rigid tanks can be excited to perform resonant motions — so called sloshing — by moving the tank in the respective direction with the associated natural frequency. The frequencies of the natural sloshing modes depend on the geometry of the container, the direction in which the container moves and the liquid filling height, but not on the density of the liquid. The most severe sloshing responses occur at the first mode, where a standing wave twice as long as the tank dimension in the direction of motion evolves inside the tank. While large amplitude oscillations appear close to the tank walls, the free surface level at the center of the tank remains at the initial height (node of the standing wave). The higher the sloshing modes, the shorter the wave length of the response and less severe the response amplitudes (wave length equals tank dimension at the second mode, at the third mode a wave with a length of 2/3 of the tank dimension occurs).

The sloshing modes for cuboid tanks can be analytically approached by applying Eq. (2.27). For chamfered tanks, these frequencies have to be corrected according to Eq. (2.28). In order to investigate the capability and quality of the linear potential theory approach to calculate responses of internal liquids, analytical and numerical sloshing modes are compared for a cuboid tank at first. As already discussed in section 2.3, the tank

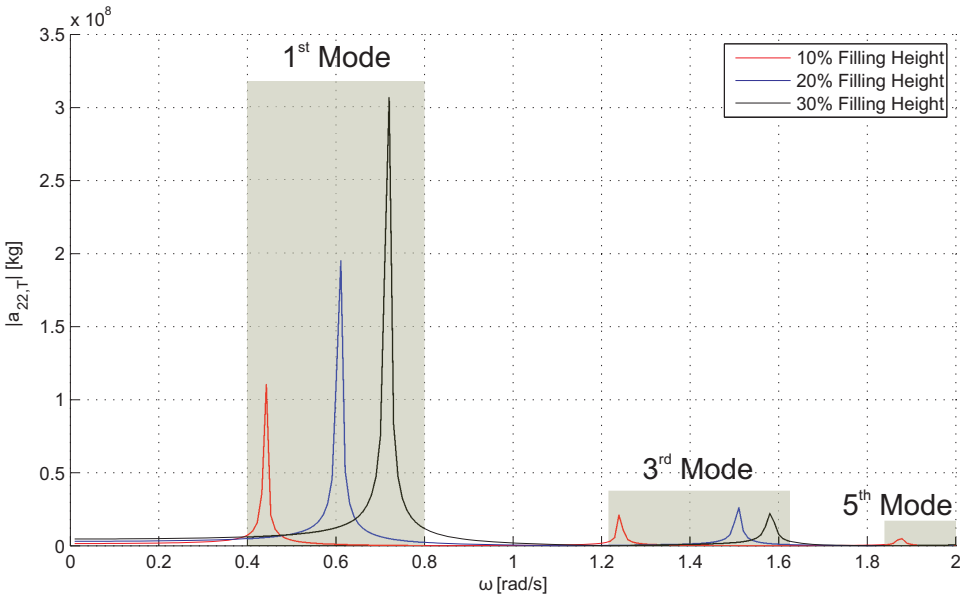


Figure 3.3: *Example of numerical sloshing mode determination for the cuboid tank from absolute values of the transverse added mass* $a_{22,T}$

added mass coefficients are singular at the resonant periods corresponding to odd sloshing modes of the tanks. Therefore, the numerical modes of the tank alone in the transverse and longitudinal direction are obtained from the peaks in the absolute values of the added masses $a_{22,T}$ and $a_{11,T}$, respectively. This procedure is exemplarily illustrated in Fig. 3.3, where the peaks in the absolute values of the transverse tank added mass $a_{22,T}$ that indicate the first three odd sloshing modes for 10%, 20% and 30% filling height are highlighted.

The comparison of analytical and numerical results for the first five sloshing modes for a cuboid tank with dimensions according to Fig. 3.4 and Tab. 3.1 is shown in Fig. 3.5. As already explained in section 2.3, even modes cannot be calculated by a linear potential theory approach, therefore only the first and third mode results can be consulted for validation purposes. For these two modes, excellent agreement of analytical and numerical data can be observed for both, the transverse (top) as well as the longitudinal direction (bottom). With increasing filling height, the frequencies follow a parabola shaped curve, approaching a limiting frequency. The filling height where this limitation is reached, decreases with increasing mode numbers. While the limit for the first transverse mode is not reached for this case, the third transverse mode converges to $\omega_R = 1.61$ rad/s already at 50% filling height.

These observation are in compliance with Faltinsen and Timokha (2009), who explicate that the influence of liquid depth inside the tank on the first natural frequency becomes smaller for 'deep liquid conditions' ($h_f/B_T > 1.0$ in the transverse and $h_f/L_T > 1.0$ in the longitudinal case), while in 'intermediate and finite liquid depths' ($0.1 < h_f/B_T < 1.0$ and $0.1 < h_f/L_T < 1.0$), frequencies are strongly shifting with altered liquid depths. In very 'shallow liquid conditions' ($h_f/B_T < 0.1$ and $h_f/L_T < 0.1$), hydraulic jumps may occur inside the tank. In case of the investigated cuboid tank, the maximum achievable ratios for solid filling (i.e. filling height 100%) are $h_f/B_T = 0.73$

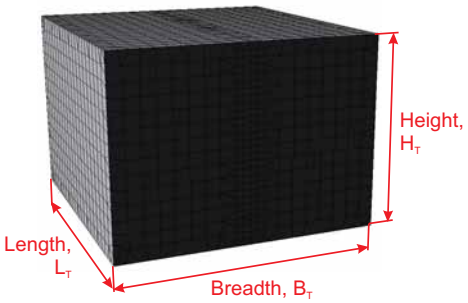


Figure 3.4: *Numerical discretization of the cuboid tank with characteristic dimensions*

| | |
|---|---|
| Length, $L_T$ [m] | 38.3 |
| Breadth, $B_T$ [m] | 35.8 |
| Height, $H_T$ [m] | 26.1 |
| Volume, $V_T$ [m$^3$] | 35,787 |

Table 3.1: *Dimensions of the cuboid tank*

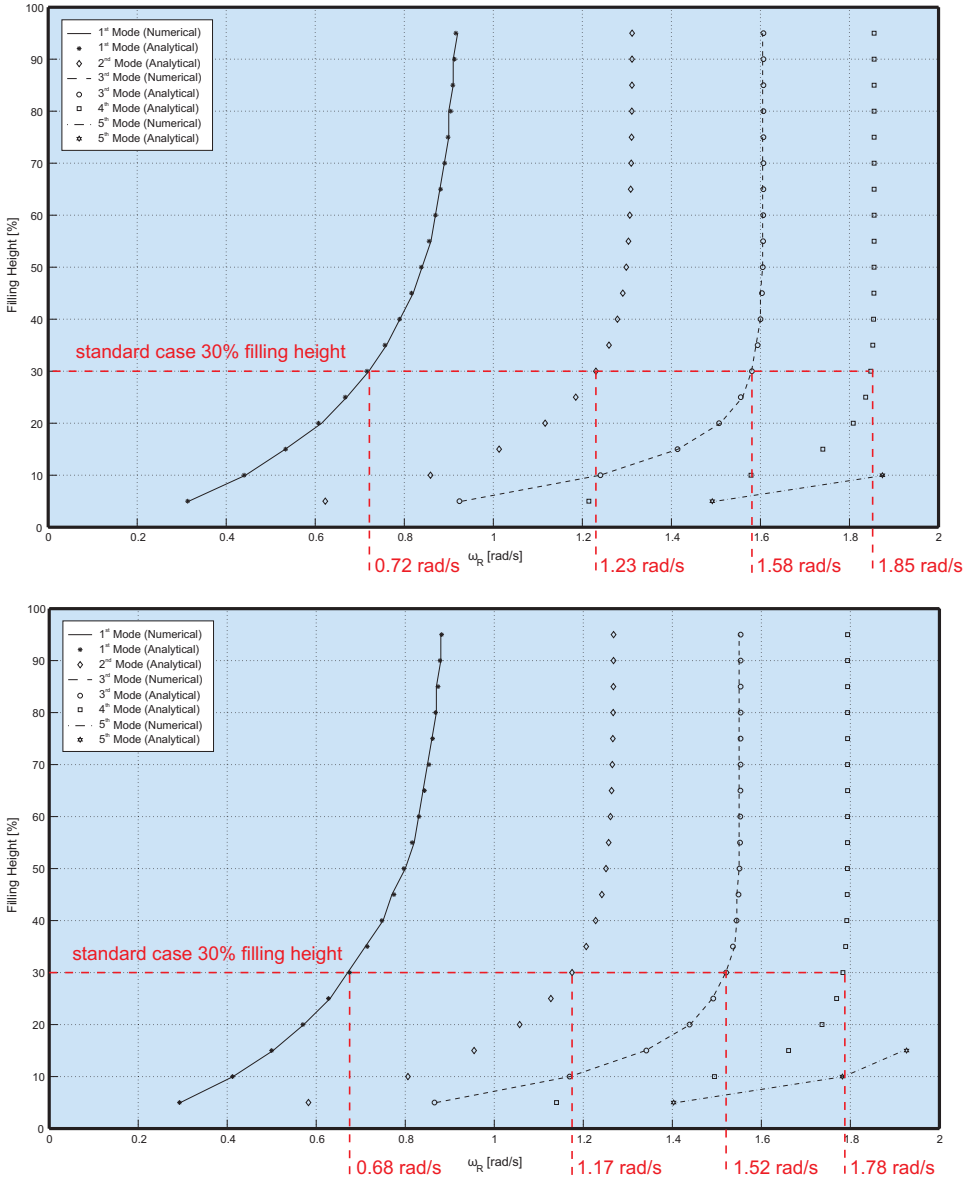


Figure 3.5: *Analytical tank resonance frequencies according to Faltinsen and Timokha (2009) compared to numerical results in dependency of the filling height in transverse (top) and longitudinal direction (bottom) for the cuboid tank*

and $h_f/L_T = 0.68$ — i.e. the first mode cannot reach the 'deep liquid condition'.

As already explained in section 2.3 and shown for the cuboid tank in Fig. 2.1, sloshing of internal fluids does also affect the restoring coefficients of the vertical modes by negative contributions. While $c_{33,T}$ remains a constant (negative) value that is independent of filling height variations, the absolute values of $c_{44,T}$ and $c_{55,T}$ increase with increasing filling height.

The comparison of analytical and numerically calculated natural sloshing modes for a prismatic tank of equal outer dimensions (see Fig. 1.6 and Tab. 1.3) according to Clauss et al. (2010b) and Clauss et al. (2011) are presented in Fig. 3.6. As before, the linear numerical approach allows comparison exclusively for odd modes. The upper part of this figure shows the first four transverse sloshing modes with respect to the filling level of the prismatic tank. Results reveal a very good agreement within a filling range from 20% to 70% (first mode) and 30% to 70% (third mode), respectively. For filling levels within the top chamfer region, i.e. more than 70%, strong deviations occur, since these geometrical features are not covered by Eqs. (2.27) and (2.28). In these regions of smaller transverse cross sections, the trend of the numerical data appears to be more reasonable and trustworthy. The bottom chamfer region on the other hand — i.e. less than 20% filling height — is taken into account by the analytical set of equations. Nevertheless, results from both approaches reveal slight deviations and should generally be considered with care in this domain, since the effect of the tank bottom falling dry at low filling heights and resonant liquid motions (hydraulic jumps) is neglected.

The longitudinal natural modes are given in the lower part of Fig. 3.6. Since Eq. (2.27) does account for the smaller transverse cross sections ($> 70\%$ and $< 20\%$ filling height), slight deviations between analytical and numerical results can be observed throughout the entire frequency range, but in particular in the chamfer regions.

Without doubt, the linear potential theory code is capable to reproduce the first and third natural sloshing modes in the longitudinal and transverse direction for cuboid tanks. For prismatic tanks, results within the narrowing upper and lower chamfer regions (where in this case the resonance frequencies are up to 25% higher with respect to the rectangular tank shape) seem to be reasonable, but should be considered with care, since nonlinear effects that cannot be taken into account are likely to occur — especially for very low filling levels. The analytical calculation procedure seems to be less reliable for prismatic tanks, since it does not account for free fluid surfaces within the upper chamfer region.

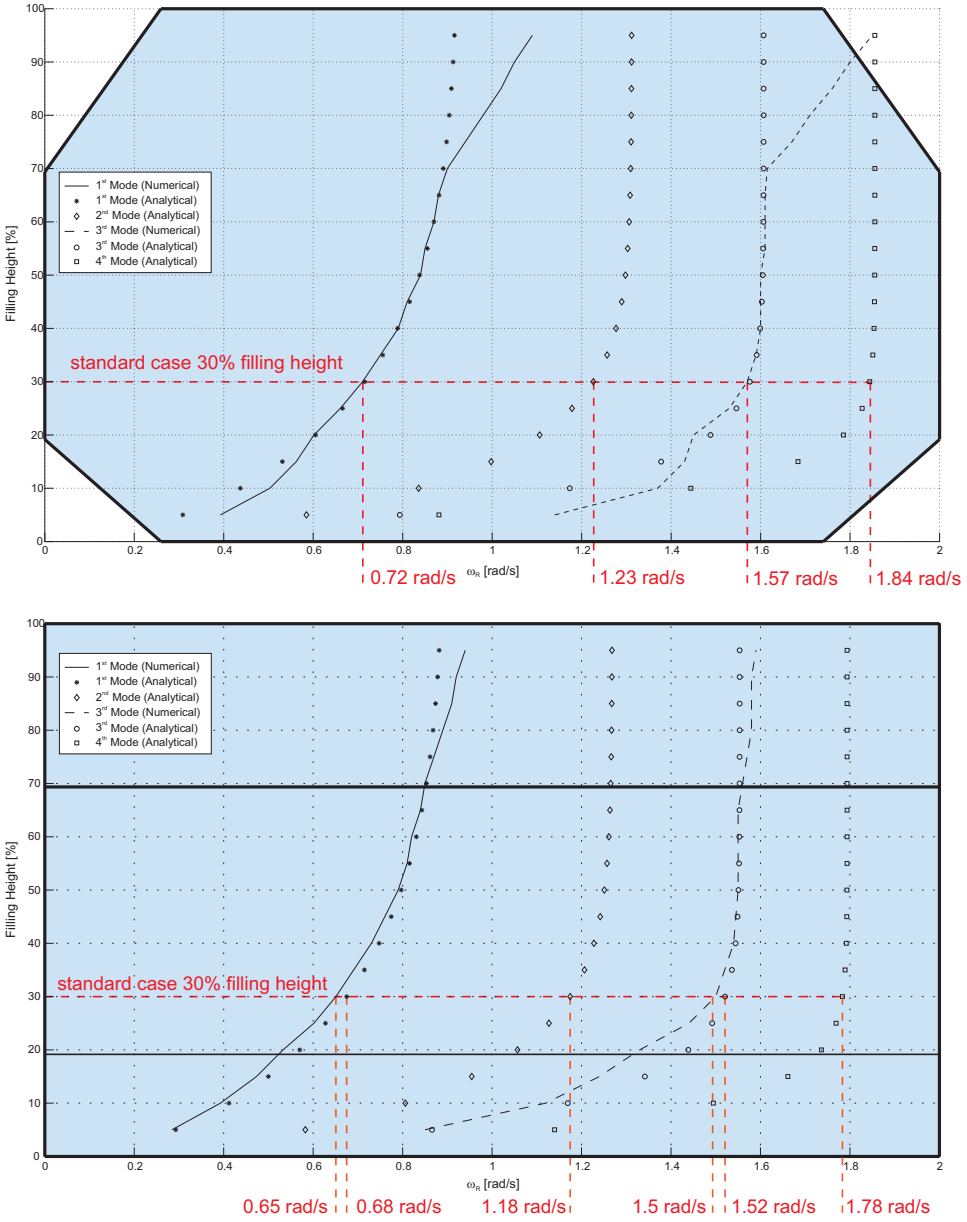


Figure 3.6: *Analytical tank resonance frequencies according to Faltinsen and Timokha (2009) compared to numerical results in dependency of the filling height in transverse (top) and longitudinal direction (bottom) for the prismatic tank (see also Clauss et al. (2010b) and Clauss et al. (2011))*

## 3.3 Coupling of Sloshing and Ship Motions

In the preceding section, solitary cuboid and prismatic tanks have been investigated to gain knowledge on the natural modes in dependency of the filling height as well as to prove the capabilities of the selected numerical method. Now, the influence of free fluid surfaces in four prismatic tanks, that are mounted to the hull of a LNGC (for main dimensions refer to Tab. 1.2) is investigated. It can be expected that free fluid surfaces onboard a vessel pose a hazardous thread on the safety of offshore operations. Not only the initial intact stability is reduced as described in section 3.1, but the ship's dynamic motion behavior is also strongly influenced by resonant internal fluid motions — as presented by Clauss et al. (2010a).

Numerical results obtained by the linear potential theory approach for relevant degrees of freedom are presented in Fig. 3.7. In the upper part of this figure, the representative motions in beam seas (incident wave angle $\beta = 90°$), i.e. sway, heave and roll (from left to right) for solid filling (tanks completely filled, no free surfaces) and 30% filling height in all four tanks (fresh water, $\rho_T = 998.2$ kg/m$^3$) are compared in frequency domain. While the heave motion remains widely unaltered (the tank fluid translates the rigid body motion), sway and in particular roll show strong alterations. Instead of one resonance peak at $\omega = 0.44$ rad/s as for the solid filling case, the roll motion RAO for 30% filling height features two peaks: the hull resonance peak of the LNGC at $\omega = 0.32$ rad/s (the shift of the rigid body resonance frequency is caused by different mass distributions due to

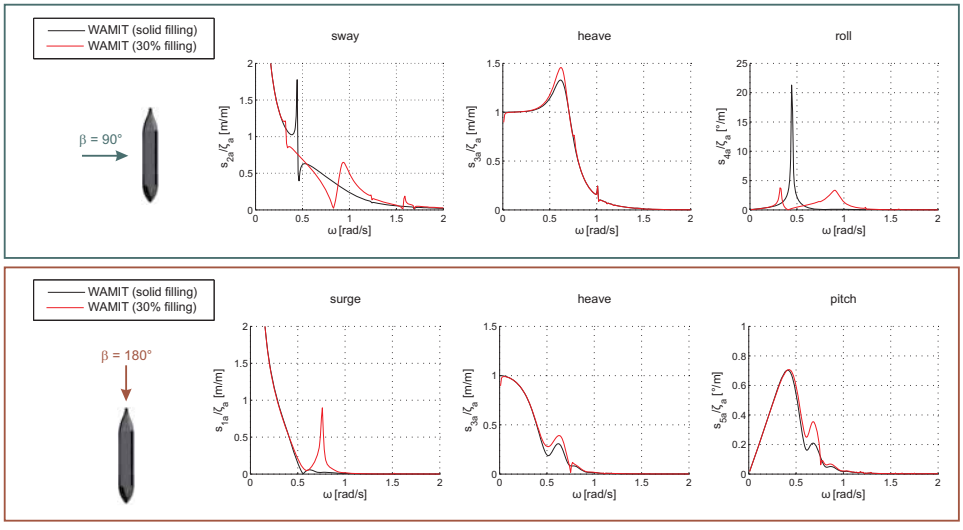


Figure 3.7: *Influence of sloshing on LNGC motions: exemplary numerical results for $\beta = 90°$ (top) and $\beta = 180°$ (bottom)*

the liquid cargo) and a secondary peak at $\omega = 0.90$ rad/s. This peak, which is less sharply pronounced than the hull resonance peak is obviously related to transverse sloshing effects in the four prismatic tanks. Captures from a miniature camera mounted onboard the LNGC behind the sternmost tank in regular waves confirm this classification of the resonance peaks (see Fig. 3.8, top and center). The characteristic of the sway motion RAO also shows obvious alterations: It approaches zero at $\omega = 0.83$ rad/s, where the inverse total mass of the system is zero, while at $\omega = 0.93$ rad/s, transverse sloshing effects lead to amplified sway RAO values.

In head seas (incident wave angle $\beta = 180°$), surge, heave and pitch are selected to illustrate the effects of free fluid surfaces on the seakeeping behavior. As shown in the lower part of Fig. 3.7, the heave motion as well as the pitch motion remain largely unaltered in the presence of internal fluids. In contrast to that, the surge motion RAO for 30% filling height features a prominent peak at $\omega = 0.76$ rad/s, which is — according to the camera captures in regular waves (see Fig. 3.8, bottom) — obviously related to resonant longitudinal sloshing inside the tanks.

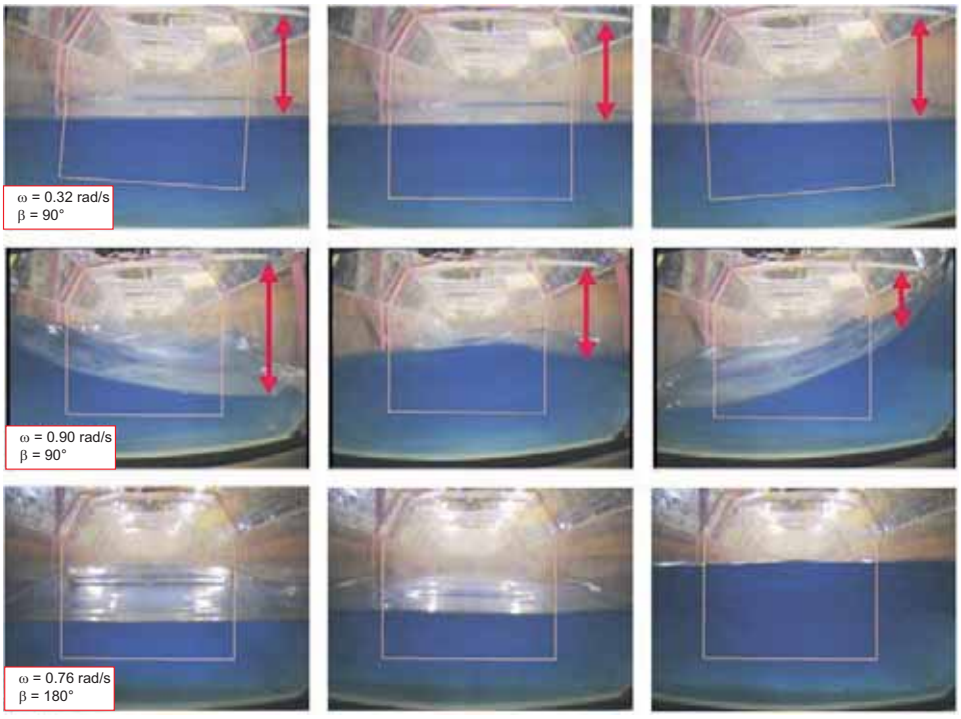


Figure 3.8: *Screen captures from the onboard camera in regular waves: $\omega = 0.32$ rad/s (top, $\beta = 90°$), $\omega = 0.90$ rad/s (center, $\beta = 90°$) and $\omega = 0.76$ rad/s (bottom, $\beta = 180°$)*

Surprisingly for both, the longitudinal and the transverse case, the sloshing related motion peaks do not match the tank resonance frequencies for the respective filling height as presented in Fig. 3.6. The secondary roll motion peak is located at $\omega = 0.90$ rad/s instead of $\omega = 0.72$ rad/s and the surge motion peak occurs at $\omega = 0.76$ rad/s instead of $\omega = 0.65$ rad/s. The causes for these deviations $\Delta\omega$ are explained in detail in section 3.3.2.

### 3.3.1 Validation of the Numerical Method

Prior to in-depth numerical studies, the selected numerical method has to be validated in order to ensure trustworthiness. For this purpose, a series of model tests with the LNGC hull made of GRP (glass-fiber reinforced plastic) at a scale of 1:100 has been conducted in the seakeeping basin of Technical University of Berlin (TU Berlin), where the model is soft-moored and equipped with four wireless, individually pulsed infrared sensors. The body motions in six degrees of freedom are precisely tracked by five cameras mounted on a carriage above the basin with a tracking range of 8 × 10 m.

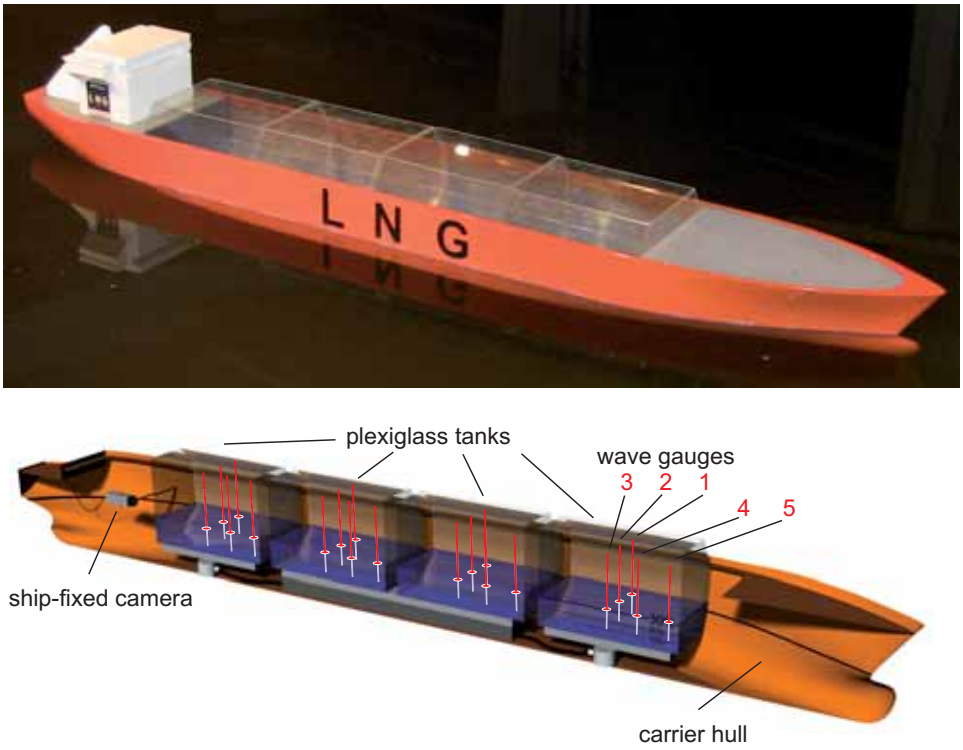


Figure 3.9: *1:100 model of the LNGC with four prismatic tanks in the seakeeping basin of TU Berlin (top); cut through a three-dimensional model of the LNGC showing the measuring equipment*

In each tank, an array of five equally spaced miniature gauges is installed from the tank centerlines to the outer tank walls in order to measure the free surface elevations inside the tanks (see Fig. 3.9). Test series with a filling level of 30% fresh water ($\rho_T = 998.2\ \frac{kg}{m^3}$) in all four tanks have been conducted at a draft of 12 m (full scale) in head seas ($\beta = 180°$) as well as beam seas ($\beta = 90°$). In order to analyze the seakeeping characteristics of the LNGC as well as the internal fluid motion characteristics at this loading condition in frequency domain, transient wave packet technique is applied (cf. Clauss and Kühnlein (1997)). Note that due to the limited motion and acceleration capabilities of the wave maker in the seakeeping basin, the frequency range of the measurements is restricted.

At first, the linear code's capability to reproduce the LNGC motion RAOs under the influence of internal fluid motions at 30% filling height is investigated. In the upper part of Fig. 3.10 the numerically determined RAOs for sway, heave and roll in beam seas ($\beta = 90°$) are compared to model test data, while the comparison for surge, heave and pitch in head seas ($\beta = 180°$) is shown in the lower part of Fig. 3.10. For both cases, the agreement of results is excellent. The occurrence and location of the sloshing-induced motion peaks that appear in the calculated roll and surge motion RAOs are confirmed by the experiments. Since body motions at resonant conditions are highly nonlinear, the height of resonance peaks has

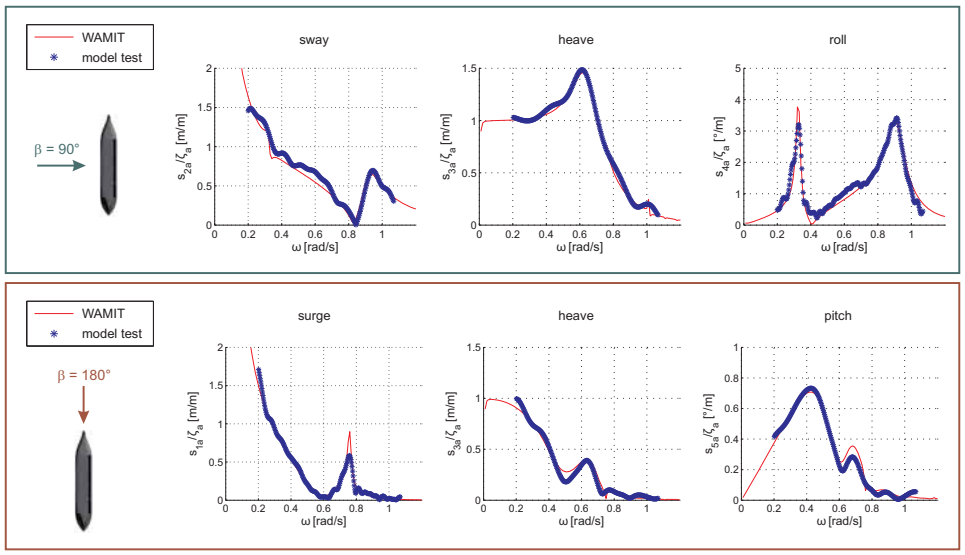


Figure 3.10: *Body motions of the LNGC with 30% filling height (fresh water, $\rho_T = 998.2\ kg/m^3$) in all four prismatic tanks: comparison of numerical calculations and model test data in beam seas ($\beta = 90°$, top) and head seas ($\beta = 180°$, bottom)*

to be considered with care in any case. Actually, the motion response at resonance frequencies cannot be represented by a linear RAO, since the ratio of motion response amplitude to exciting wave amplitude increases with decreasing incident wave heights and vice versa.

Apart from the seakeeping characteristics of the LNGC, the internal fluid motions in each of the four prismatic tanks are of particular interest. The array of five wave gauges (denoted by G1 to G5) from the model tests is numerically simulated by an array of five field points per tank at the same positions. At each field point, the ratio of the surface elevation amplitudes of the internal fluid to the amplitudes of the incident wave is calculated and compared to the measurements conducted with the ship-fixed wave gauges. The comparison for beam seas ($\beta = 90°$) is presented in Fig. 3.11. Each column contains results for one tank (tank 4 to 1 from left to right) and the

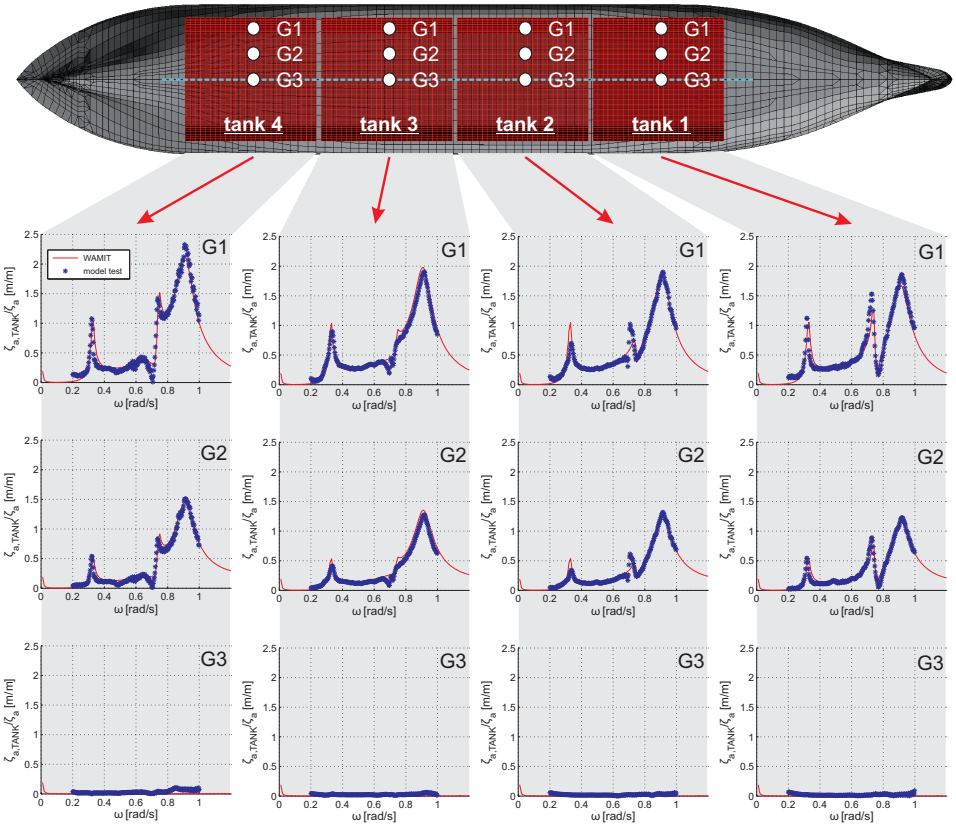


Figure 3.11: *Internal fluid motions inside the four prismatic tanks mounted to the LNGC hull with 30% filling height (fresh water, $\rho_T = 998.2$ kg/m$^3$): comparison of numerical calculations and model test data in beam seas ($\beta = 90°$)*

lines represent different gauge locations (gauge G1 [near the transverse tank wall] to gauge G3 [at the tank's longitudinal center line] from top to bottom). In the frequency range of the model test data (0.2 rad/s $\leq \omega \leq$ 1.0 rad/s), excellent agreement of numerical and experimental data is observed. For deviations in resonance peak height the same as for the body motions applies. A continuous decrease of surface elevation amplitudes from the tank wall to the center line becomes apparent. Since the evaluated frequency range includes the first but no higher sloshing modes, this observation is in compliance with the assumption of a standing wave with the node at the center line (G3) of the tank and antinodes at the tank walls (G1).

From the lateral motion RAOs (see roll in Fig. 3.7), two resonance peaks can be expected for the internal fluid motions: the LNGC hull resonance at $\omega = 0.32$ rad/s and the peak related to transverse sloshing effects at

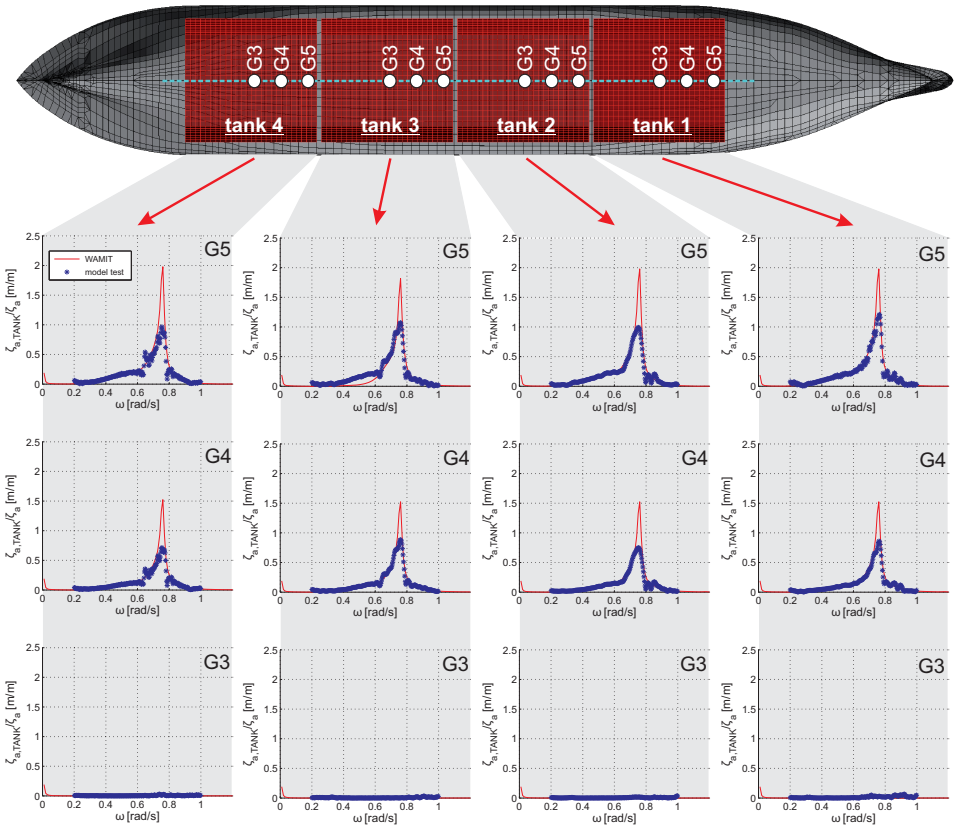


Figure 3.12: *Internal fluid motions inside the four prismatic tanks mounted to the LNGC hull with 30% filling height (fresh water, $\rho_T = 998.2$ kg/m$^3$): comparison of numerical calculations and model test data in head seas ($\beta = 180°$)*

$\omega = 0.90$ rad/s. Instead, Fig. 3.11 reveals a surprising finding, which is discussed in detail in section 3.3.3: The internal fluid motions of the investigated LNGC with 30% filling height in all four prismatic tanks feature a third peak at $\omega = 0.75$ rad/s, whose magnitude differs from tank to tank. Especially in the outer tanks 1 and 4, this peak is strongly pronounced, while it is less visible in the center tanks 2 and 3.

The internal fluid motions in head seas ($\beta = 180°$) are shown in Fig. 3.12. In analogy to the preceding case, each column contains results for one tank (tank 4 to 1 from left to right) and each line represents a specific gauge location (gauge G5 [near the longitudinal tank wall] to gauge G3 [at the tanks transverse center line] from top to bottom). Again, excellent agreement of the potential theory results and experimental data can be observed. Since a longitudinal standing wave is evolving inside the tank in the frequency range around the first natural mode, responses decrease from G5 (antinode) to G3 (node). In contrast to the beam sea case, no additional surprising fluid response peak occurs.

### 3.3.2 Discussion I: Frequency Shifts

It has been shown by Clauss et al. (2011), that the peak frequency shift $\Delta\omega$ addressed in the last paragraph of section 3.3 is accompanied by a phase shift between LNGC hull motions and internal liquid motions. This effect is visualized by the exemplary comparison of LNGC hull motions and internal fluid motions for $\beta = 90°$ in Fig. 3.13: In the vicinity of the first transverse sloshing mode, a phase shift occurs between LNGC roll motions and liquid motions. Although strong transverse sloshing is present at $\omega = 0.72$ rad/s, no amplifying effect on the vessel motions can be observed, i.e. there is no peak in the roll RAO. For lower (0.4 rad/s $< \omega <$ 0.6 rad/s) and higher frequency regions (0.8 rad/s $< \omega <$ 1.1 rad/s) internal liquid motions are in phase with the roll motion which leads to reciprocal amplification. However, this observation seems to be an effect of the frequency shift rather than a cause. As schematically illustrated in Fig. 3.14, the complete chain of cause and effect for the transverse sloshing peak shift can be broken down into three steps (see also Clauss et al. (2012)):

1. The matrix formulation of the underlying equation of motion

$$\underline{s}\ \left[-\omega^2\ (\underline{A} + \underline{M}) + i\omega\ (\underline{B} + \underline{B}_v) + \underline{C}\right] = \underline{F}_{ex} \tag{3.6}$$

   can be solved for the desired motion $s_i$ by multiplying the external forces on the right-hand side by the inverse matrix of the internal forces (The formulation in brackets on the left-hand side is denoted by $\underline{F}_{int}$ in the following. Factoring out the restoring coefficients, this expression is equivalent to the well-known dynamic magnification factor V($\Omega$,$\delta$), see appendix B). Hence, the roll motion $s_4$ can explicitly be determined by

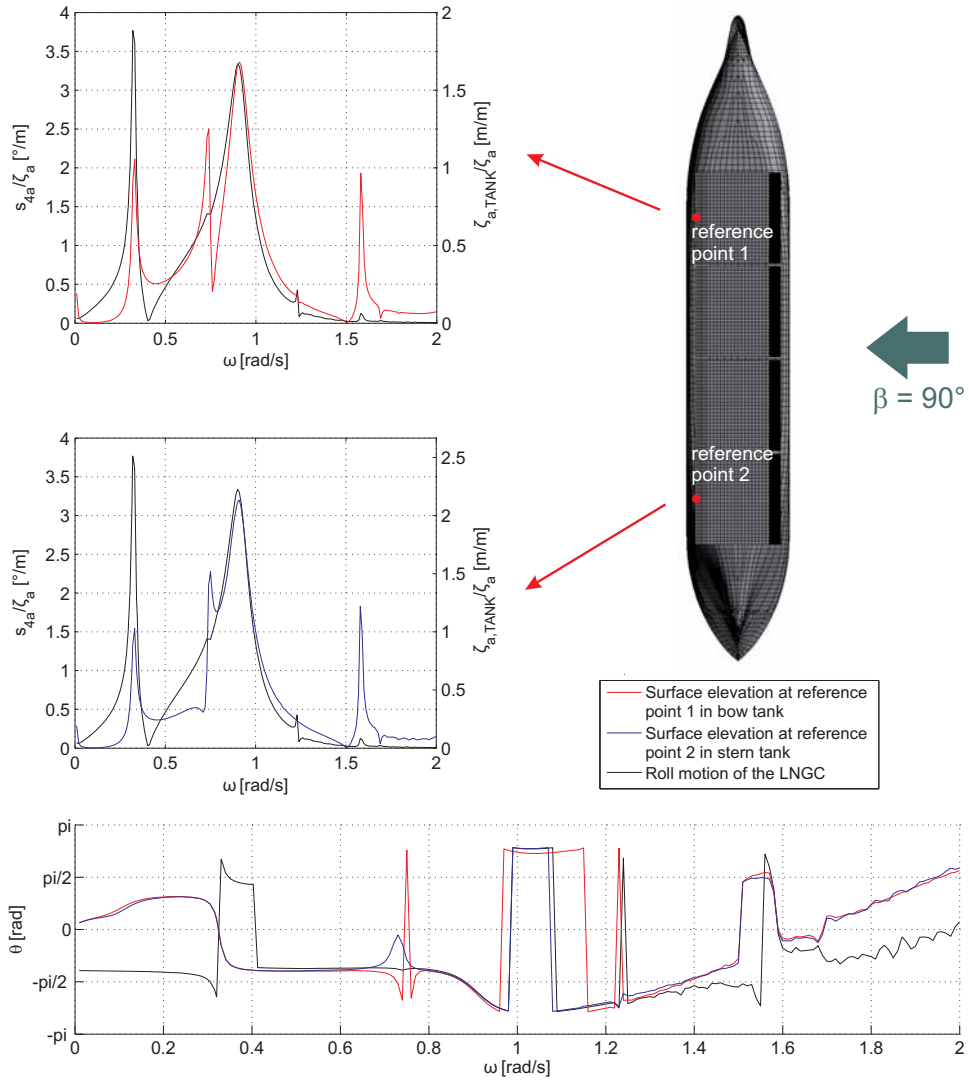


Figure 3.13: *Comparison of roll motion and internal tank surface elevations at the indicated reference points for the bow tank (top left) and the stern tank (center left) as well as phase angles of the surface elevations and the roll motion of the hull (bottom) for 30% filling height in all four tanks and* $\beta = 90°$

the expression

$$s_4 = \sum_{j=1}^{6} f_{ex,j} \cdot f_{int,j4}^{-1} \, . \tag{3.7}$$

For the chosen LNGC geometry in beam seas ($\beta = 90°$), the first, third and fifth term of Eq. (3.7) becomes zero and the sixth term is very small, so in this case the roll motion can be approximated by

$$s_4 \approx f_{ex,2} \cdot f_{int,24}^{-1} + f_{ex,4} \cdot f_{int,44}^{-1} \, , \tag{3.8}$$

in other words by effects related to pure roll and sway-roll coupling. In box 1 of Fig. 3.14, these two components are visualized. It becomes clear that the shifted peak at $\omega = 0.9$ rad/s is related to the first term of Eq. (3.8), i.e. the sway-roll coupling. The decomposition of this term reveals that the shifting phenomenon is associated with the inverse internal force component, which is further analyzed in the next step.

2. The detailed investigation of the components of the inverse internal force $f_{int,24}^{-1}$ reveals that the mass term is the source of the peak shift phenomenon. As shown in box 2 in Fig. 3.14, the peak of the added mass $a_{24}$ (solid blue line, overlapped by solid red line) as well as of the total mass $[a + m]_{24}$ (solid red line) is located at the predicted first transverse sloshing mode ($\omega = 0.72$ rad/s). The inversion of both matrices leads to shifted discontinuities: the jump of the inverted added mass $a_{24}^{-1}$ (dashed blue line) is located at $\omega = 1.16$ rad/s and of the inverted total mass $[a + m]_{24}^{-1}$ (dashed red line) at $\omega = 0.9$ rad/s. Since the inversion procedure obviously seems to be the key to the comprehension of the frequency shift, it is manually reconstructed in the subsequent step.

3. The inverse of the 6x6 mass matrix is determined according to Cramer's rule:

$$\underline{A}^{-1} = \frac{1}{det(\underline{A})} \, Adj(\underline{A}) \tag{3.9}$$

where $det(\underline{A})$ is the determinant and $Adj(\underline{A})$ the adjugate matrix of $\underline{A}$, which can be calculated by the expression

$$Adj(\underline{A}) = (-1)^{i+j} \, det(\underline{A}_{ij}^{*}) \tag{3.10}$$

where the minor is denoted by $det(\underline{A}_{ij}^{*})$. The determinants of these sparse matrices can be calculated by applying Laplace expansion. For this particular case, the equation to determine element $_{24}$ of the inverted added mass matrix becomes

$$a_{24}^{-1} = \frac{det(\underline{A}_{42}^{*})}{det(\underline{A})} \tag{3.11}$$

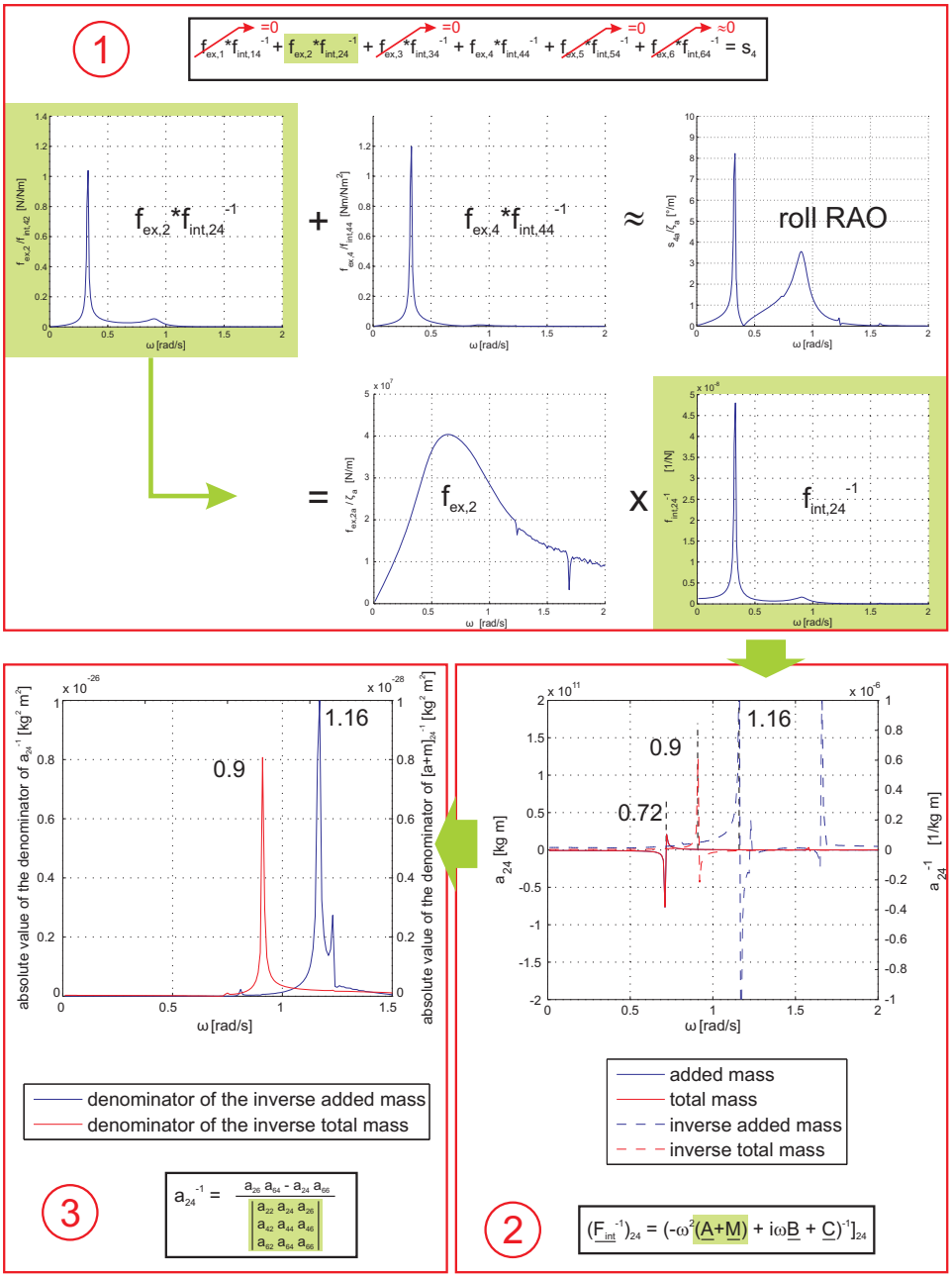


Figure 3.14: *Scheme of the systematical backtracing of the first transverse sloshing peak shift in three steps*

and the inverted total mass element is

$$[a+m]^{-1}_{24} = \frac{det([\underline{A+M}]^{*}_{42})}{det([\underline{A+M}])} \tag{3.12}$$

respectively. The procedure described above finally leads to an explicit expression for element $_{24}$ of the inverted added mass matrix:

$$a^{-1}_{24} = \frac{a_{26}a_{64} - a_{24}a_{66}}{\begin{vmatrix} a_{22} & a_{24} & a_{26} \\ a_{42} & a_{44} & a_{46} \\ a_{62} & a_{64} & a_{66} \end{vmatrix}} \tag{3.13}$$

The inverse total mass element can be expressed analogously. The discontinuities can finally be traced back to the peaks of absolute reciprocal value of the denominator of Eq. (3.13) — which is proven by the graph in box 3 in Fig. 3.14. Coupling of sway, roll and yaw motions are relevant influences. The magnitude of the peak shift is directly related to the ratio of rigid body mass (i.e. hull mass without mass of the liquid cargo) to added mass: The lower the respective rigid mass, the larger the peak shift $\Delta\omega$. For the added mass alone (equivalent to all rigid mass elements equal zero, i.e. $\underline{M} = 0$) the maximum shift is obtained, in this case $\Delta\omega = 0.44$ rad/s, with a response peak at $\omega = 1.16$ rad/s instead of 0.72 rad/s.

For the LNGC in head seas ($\beta = 180°$), a shift of the peak frequency $\Delta\omega$ as addressed in the last paragraph of section 3.3 can be observed as well. In Fig. 3.15, the absolute values and phases of the LNGC surge motion and internal fluid motions are compared. At $\omega = 0.76$ rad/s, the absolute values of the liquid motions in both tanks as well as the surge motion feature a prominent peak. At this frequency, longitudinal sloshing amplifies the surge motion of the vessel. In contrast to the transverse direction, the motions of the internal fluid in tank 1 and tank 4 show no significant deviations. This impression is confirmed by the phase angles of the respective liquid motions: for $\omega < 1.1$ rad/s, the phase angles at both reference points are identical. Since the indicated reference points are located at the rear walls of tank 1 and tank 4, a phase shift of 180° between the surge motion (positive in forward direction) and internal fluid motions occurs over a wide range of frequencies ($\omega < 0.9$ rad/s).

For the longitudinal direction, an analogous investigation of the peak shift can be conducted, i.e. Eq. (3.6) can be solved for the surge motion $s_1$:

$$s_1 = \sum_{j=1}^{6} f_{ex,j} \cdot f^{-1}_{int,j1} \tag{3.14}$$

For the LNGC in head seas ($\beta = 180°$), the second, fourth and sixth term of Eq. (3.14) becomes zero, i.e. the equation to determine the surge motion

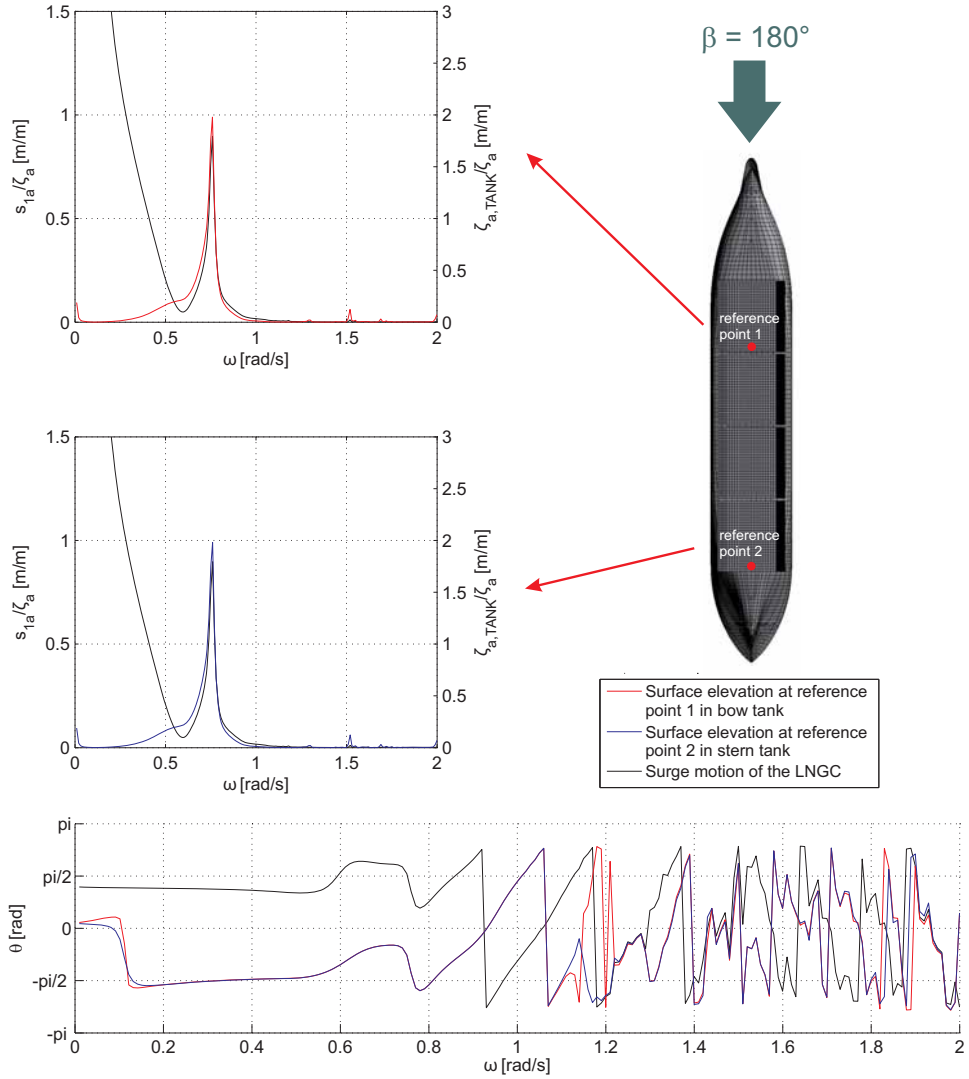


Figure 3.15: *Comparison of surge motion and internal tank surface elevations at the indicated reference points for the bow tank (top left) and the stern tank (center left) as well as phase angles of the surface elevations and the surge motion of the hull (bottom) for 30% filling height in all four tanks and* $\beta = 180°$

can be explicitly written as

$$s_1 = f_{ex,1} \cdot f_{int,11}^{-1} + f_{ex,3} \cdot f_{int,31}^{-1} + f_{ex,5} \cdot f_{int,51}^{-1} \tag{3.15}$$

This formulation contains coupling effects between surge, heave and pitch motions. In box 1 of Fig. 3.16, these three components are visualized. Since the shifted longitudinal sloshing peak at $\omega = 0.76$ rad/s clearly appears in all three terms of Eq. (3.15), the third term (surge-pitch coupling) is exemplarily chosen for further analyses. As before for the transverse case, the decomposition of this term reveals that the shifting phenomenon is related to the mass term of the inverse internal force component $f_{int,51}^{-1}$. As shown in box 2 in Fig. 3.16, the peak of the added mass $a_{51}$ (solid blue line, overlapped by solid red line) as well as of the total mass $[a+m]_{51}$ (solid red line) is located at the predicted first longitudinal sloshing mode ($\omega = 0.65$ rad/s). Again, the inversion of both, the added mass and the total mass matrix, reveals discontinuities at $\omega = 0.76$ rad/s (inverted total mass $[a + m]_{51}^{-1}$ [dashed red line]) and $\omega = 1.12$ rad/s (inverted added mass $a_{51}^{-1}$ [dashed blue line]). In order to reconstruct the inversion procedure manually, the following equation (exemplarily conducted for the added mass, the inverse total mass element $[a + m]_{51}^{-1}$ is determined analogously) has to be solved:

$$a_{51}^{-1} = \frac{det(\underline{A}_{15}^{*})}{det(\underline{A})} \tag{3.16}$$

Finally, an explicit expression for element $_{51}$ of the inverted added mass matrix is obtained:

$$a_{51}^{-1} = \frac{a_{31}a_{53} - a_{33}a_{51}}{\begin{vmatrix} a_{11} & a_{13} & a_{15} \\ a_{31} & a_{33} & a_{35} \\ a_{51} & a_{53} & a_{55} \end{vmatrix}} \tag{3.17}$$

The graph in box 3 of Fig. 3.16 shows that the discontinuities can be traced back to the peaks of the absolute reciprocal value of the denominator of Eq. (3.17), where coupling of surge, heave and pitch motions are relevant influences. As for the transverse case, the magnitude of the peak shift $\Delta\omega$ is directly related to the ratio of rigid body mass to added mass: For the added mass alone (equivalent to all rigid mass elements equal zero, i.e. $\underline{M} = 0$) the maximum shift is obtained, in this case $\Delta\omega = 0.36$ rad/s, with a response peak at $\omega = 1.12$ rad/s instead of 0.76 rad/s.

The same effects have to be taken into account when LNGC seakeeping with internal liquids of different density is compared. It is common to conduct model tests with fresh water ($\rho_T = 998.2$ kg/m$^3$) inside LNG tanks, but the obtained results cannot be directly transferred to full scale operations with LNG ($\rho_T = 435$ kg/m$^3$). Due to the greater mass of fresh water at identical filling heights, the solid hull mass for the same vessel at constant

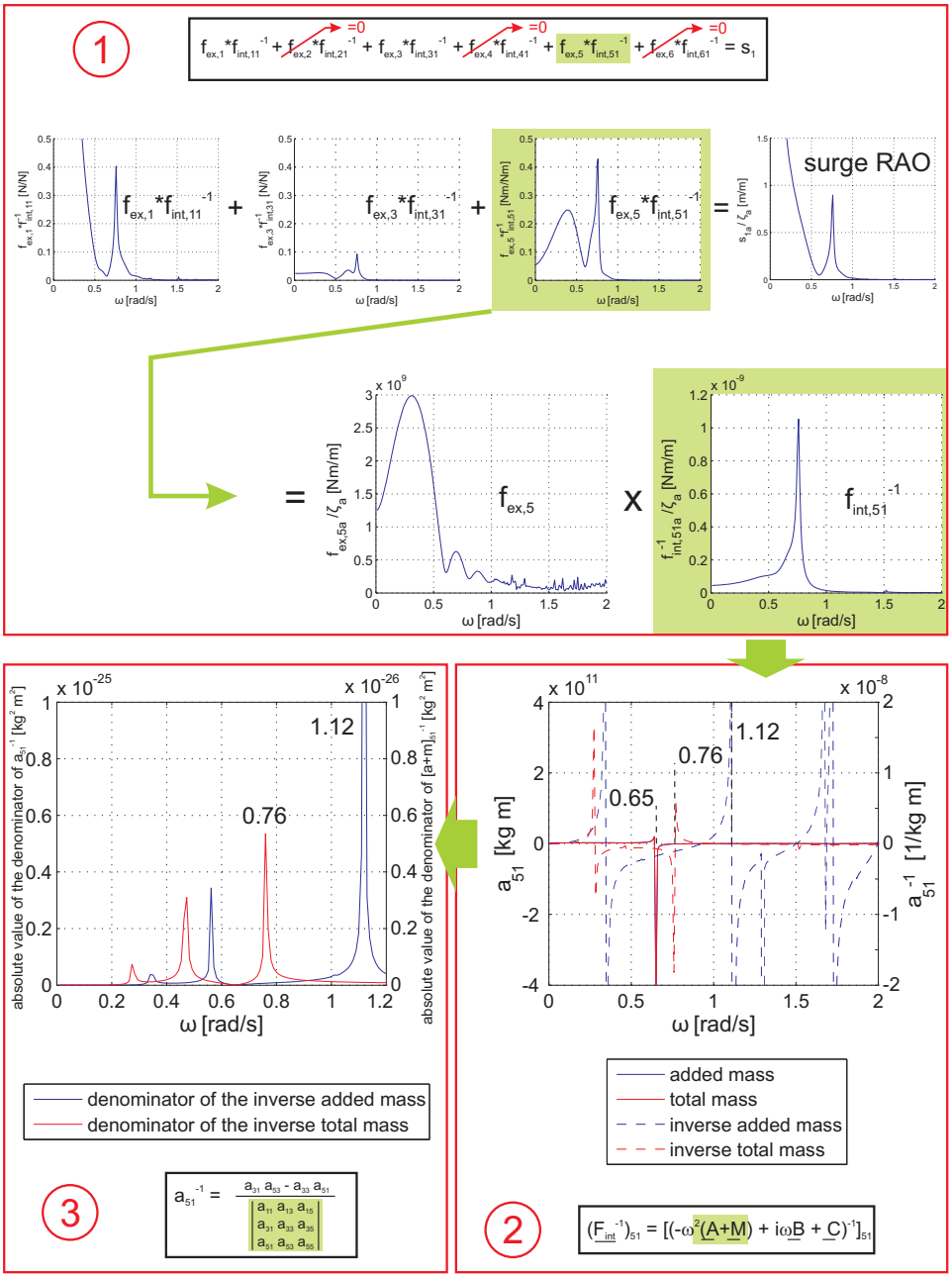


Figure 3.16: *Scheme of the systematical backtracing of the first longitudinal sloshing peak shift in three steps*

draft has to be higher when the tanks are filled with LNG instead. Consequently, the high-frequency peak of the internal LNG motions as well as the associated peaks in the surge and roll motion RAO will be located closer to the theoretical first sloshing mode, i.e $\Delta\omega_{H_2O} > \Delta\omega_{LNG}$. This is exemplarily shown in Fig. 3.17 where the roll motion RAO ($\beta = 90°$, left) as well as the surge motion RAO ($\beta = 180°$, right) for 30% fresh water filling (red line) are compared to 30% LNG filling. Due to the higher rigid body mass for LNG filling in this case, the rigid body resonance frequency is higher.

In order to obtain general conclusions on the evolution of the frequency deviation $\Delta\omega$, the LNGC is systematically investigated with equally distributed fresh water ($\rho_T = 998.2$ kg/m$^3$) as well as LNG ($\rho_T = 435$ kg/m$^3$) filling in all four prismatic tanks (all relevant input data for the respective calculations is given in Appendix A). Due to the higher density of fresh water, the weight of the liquid cargo would exceed the vessel's buoyancy for filling heights of more than 70%, i.e. calculations are conducted in a range of filling heights between 5% and 70%, while for LNG, the entire range from 5% to 95% filling height is investigated. In Fig. 3.18, the analytical first sloshing mode according to Eqs. (2.27) and (2.28) is compared to the sloshing related (shifted) peaks in the relevant motion RAOs. In the upper part of the figure, the deviation $\Delta\omega$ between the analytical first transverse sloshing mode and the sloshing related peak of the roll motion ($\beta = 90°$) is presented in dependency of the filling height for fresh water and LNG. The deviation between the analytical first longitudinal sloshing mode and the surge motion peak ($\beta = 180°$) is shown in the lower part of Fig. 3.18. The

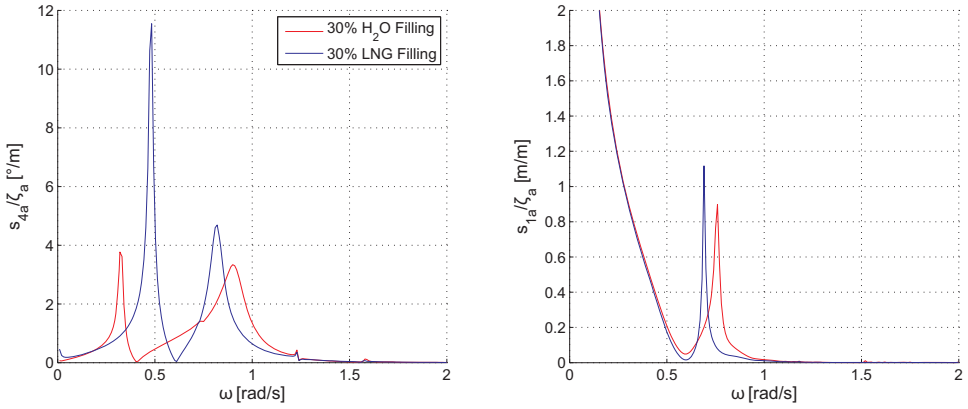


Figure 3.17: *Comparison of the roll (left) and surge (right) motion RAOs of the LNGC for 30% fresh water ($\rho_T = 998.2$ kg/m$^3$) and LNG ($\rho_T = 435$ kg/m$^3$) filling in all four prismatic tanks.*

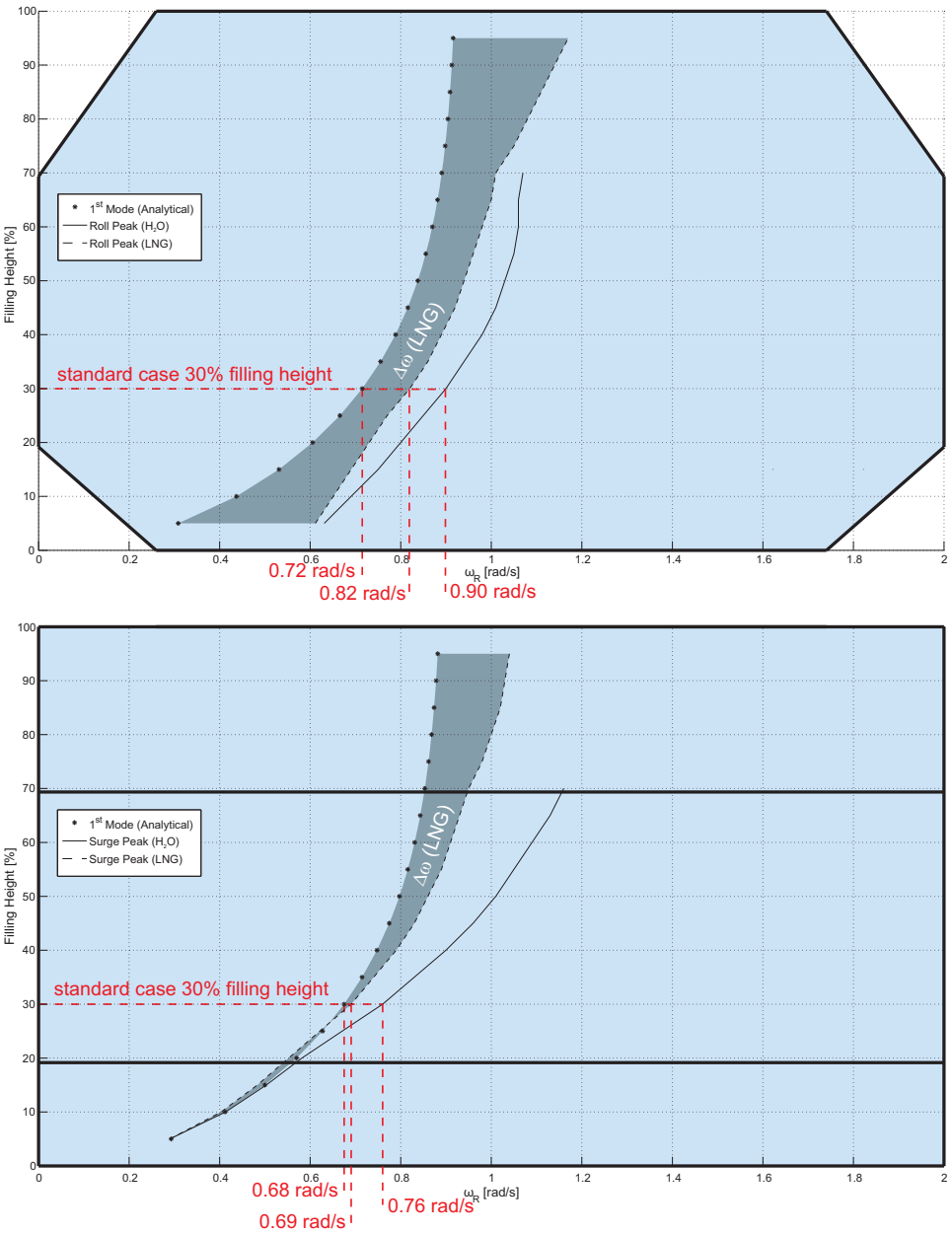


Figure 3.18: *Analytical tank resonance frequencies according to Faltinsen and Timokha (2009) compared to numerical results of the sloshing induced LNGC roll motion peak ($\beta = 90°$, top) and surge motion peak ($\beta = 180°$, bottom) in dependency of the filling height and the fluid density (straight line represents fresh water [$\rho_T = 998.2$ kg/m$^3$], dashed line represents LNG [$\rho_T = 435$ kg/m$^3$]) for four equally filled prismatic tanks mounted to the hull. The deviations $\Delta\omega$ between the analytical first sloshing mode and the body response for LNG filling are highlighted by dark shaded areas.*

observation for the exemplary case with 30% filling height in Fig. 3.17 can be confirmed in general: due to the lower density of LNG compared to fresh water, $\Delta\omega$ for LNG is always smaller. While the deviation remains roughly constant over the entire range of filling heights for the transverse direction, the longitudinal $\Delta\omega$ is close to zero for very low filling heights and increases with increasing filling heights. This effect is even more pronounced for fresh water. Due to coupling of the lateral motions sway and roll and yaw, the sway as well as the yaw motion is also affected by transverse sloshing effects. As briefly shown in Fig. 3.19, the yaw motion response peaks are subject to the same phenomenon as described above for the roll and surge motion: the deviation $\Delta\omega$ — which in case of the yaw motion is also increasing with increasing filling height — is related to the ratio of rigid body mass to added mass. Peak shifts $\Delta\omega$ also occur for the sloshing induced sway responses. These observations substantiate that model tests with fresh water alone are not sufficient to determine the seakeeping behavior of LNGCs with partially filled tanks. Instead, additional numerical investigations with LNG have to

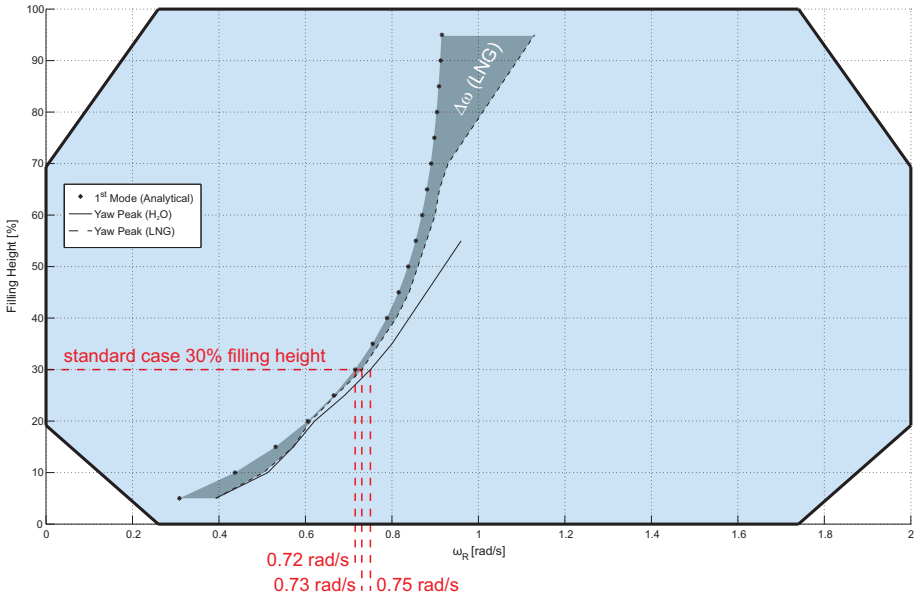


Figure 3.19: *Analytical tank resonance frequencies according to Faltinsen and Timokha (2009) compared to numerical results of the sloshing induced LNGC yaw motion peak in dependency of the filling height and the fluid density (straight line represents fresh water [$\rho_T$ = 998.2 kg/m$^3$], dashed line represents LNG [$\rho_T$ = 435 kg/m$^3$]) for four equally filled prismatic tanks mounted to the hull. The deviations $\Delta\omega$ between the analytical first sloshing mode and the body response for LNG filling are highlighted by dark shaded areas.*

be conducted once the numerical model is successfully validated with fresh water model tests.

### 3.3.3 Discussion II: Asymmetries

As already briefly mentioned in section 3.3.1, the validation of the internal fluid motion RAOs in beam seas reveals a surprising phenomenon: On the basis of the lateral motion RAOs (see Fig. 3.10, top) — in particular the roll motion RAO — two characteristic peaks are expected to occur in the transverse fluid motions. But in Fig. 3.11, three peaks can be observed: A low frequency peak at $\omega = 0.32$ rad/s, which represents the rigid body roll motion resonance, a high frequency peak at $\omega = 0.90$ rad/s which is related to strong transverse sloshing and a peak of intermediate frequency at $\omega = 0.75$ rad/s, which is strongly pronounced in the outer tanks 1 and 4 and less prominent in the center tanks 2 and 3. This peak is close to the theoretical transverse sloshing peak at $\omega = 0.72$ rad/s, but its cause and origin are not clear yet.

In order to get a comprehensive impression of the internal fluid responses, the numerically obtained deflections of the entire free surface in tank 4 (refer to Fig. 3.11) are visualized by three-dimensional tank representations in Fig. 3.20. The internal fluid motions at the hull resonance frequency $\omega = 0.32$ rad/s are shown in the left column, the response at $\omega = 0.75$ rad/s is shown in the center column and the right column contains resonant transverse sloshing at $\omega = 0.90$ rad/s. For each frequency, the fluid motion is represented by images of one period of the harmonic response oscillation at $\theta = 0$ rad (response for wave crest at the ship's centerline), $\theta = \pi/2$ rad (zero down-crossing at ship's centerline), $\theta = \pi$ rad (wave trough at ship's centerline) and $\theta = 3/2\pi$ rad (zero up-crossing at ship's centerline) respectively. For orientation, the RAO of gauge G1 in tank 4 is shown at the top of the figure. The position of the gauge is indicated by a vertical red line in each tank image.

For the hull resonance frequency at $\omega = 0.32$ rad/s, the free surface inside tank 4 remains level and parallel to the surrounding still water level but inclines with respect to a ship-fixed observer. This phenomenon can be described to appear as if 'the ship rolls around the internal fluid' and is confirmed by snapshots from the onboard camera in Fig. 3.8 (top).

Strong transverse fluid motions can be observed at $\omega = 0.90$ rad/s. At this frequency, the surface elevations at the rear tank wall are constantly higher than at the front tank wall.

At $\omega = 0.75$ rad/s, strong sloshing occurs in tank 4. From the development over one period, it becomes clear that a moderate transverse component (see $\theta = \pi/2$ rad and $\theta = 3/2\pi$ rad) and a strong longitudinal component (see $\theta = 0$ rad and $\theta = \pi$ rad) are present. This asymmetric

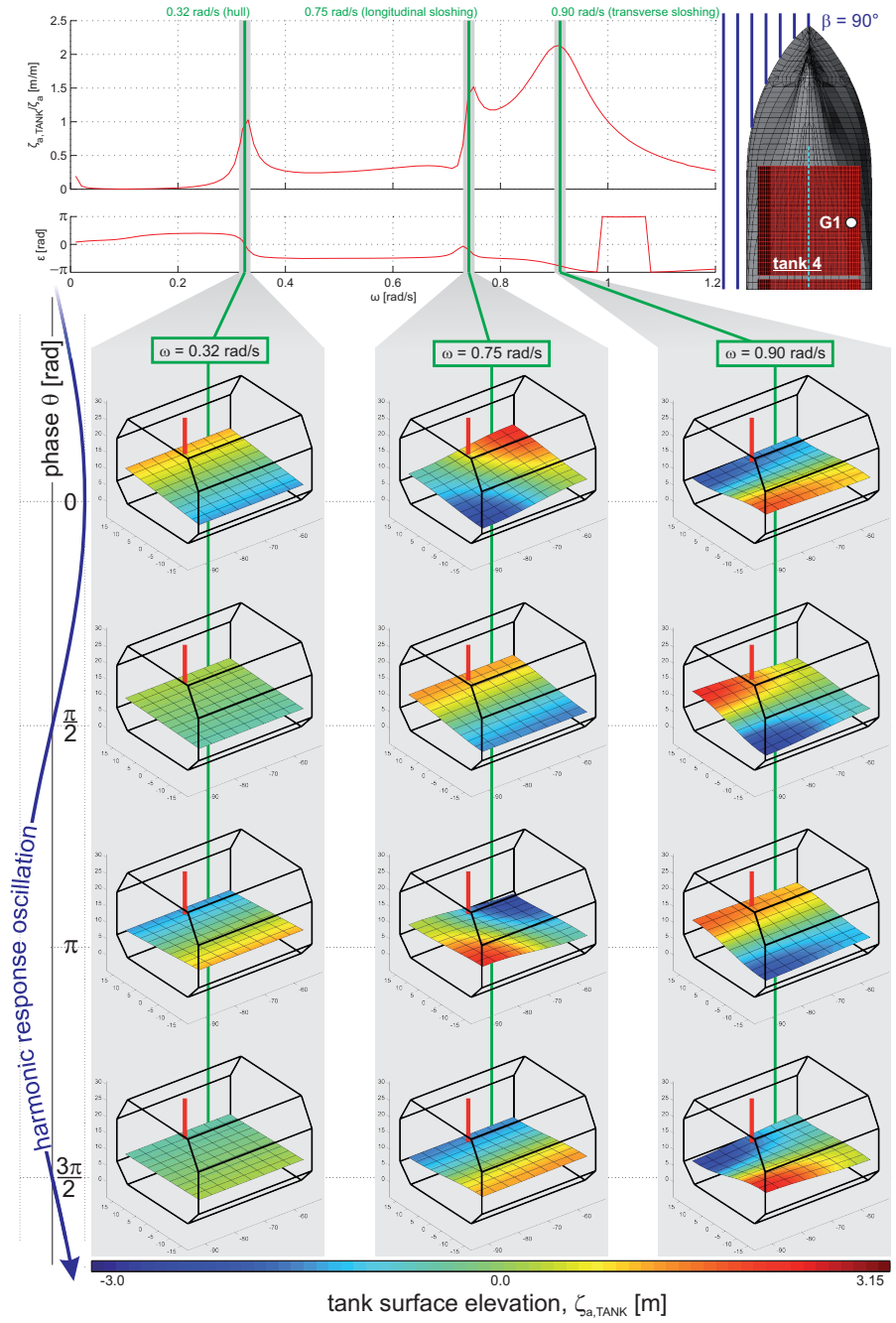


Figure 3.20: *Surface elevation of the internal fluid in tank 4 (stern) for the three selected frequencies $\omega = 0.32$ rad/s (left column), $\omega = 0.75$ rad/s (center) and $\omega = 0.90$ rad/s (right column) for the LNGC in beam seas at 30% filling height. Each column represents one harmonic oscillating response period for one frequency in four steps ($\theta = 0$, $\pi/2$, $\pi$ and $3/2\,\pi$), respectively.*

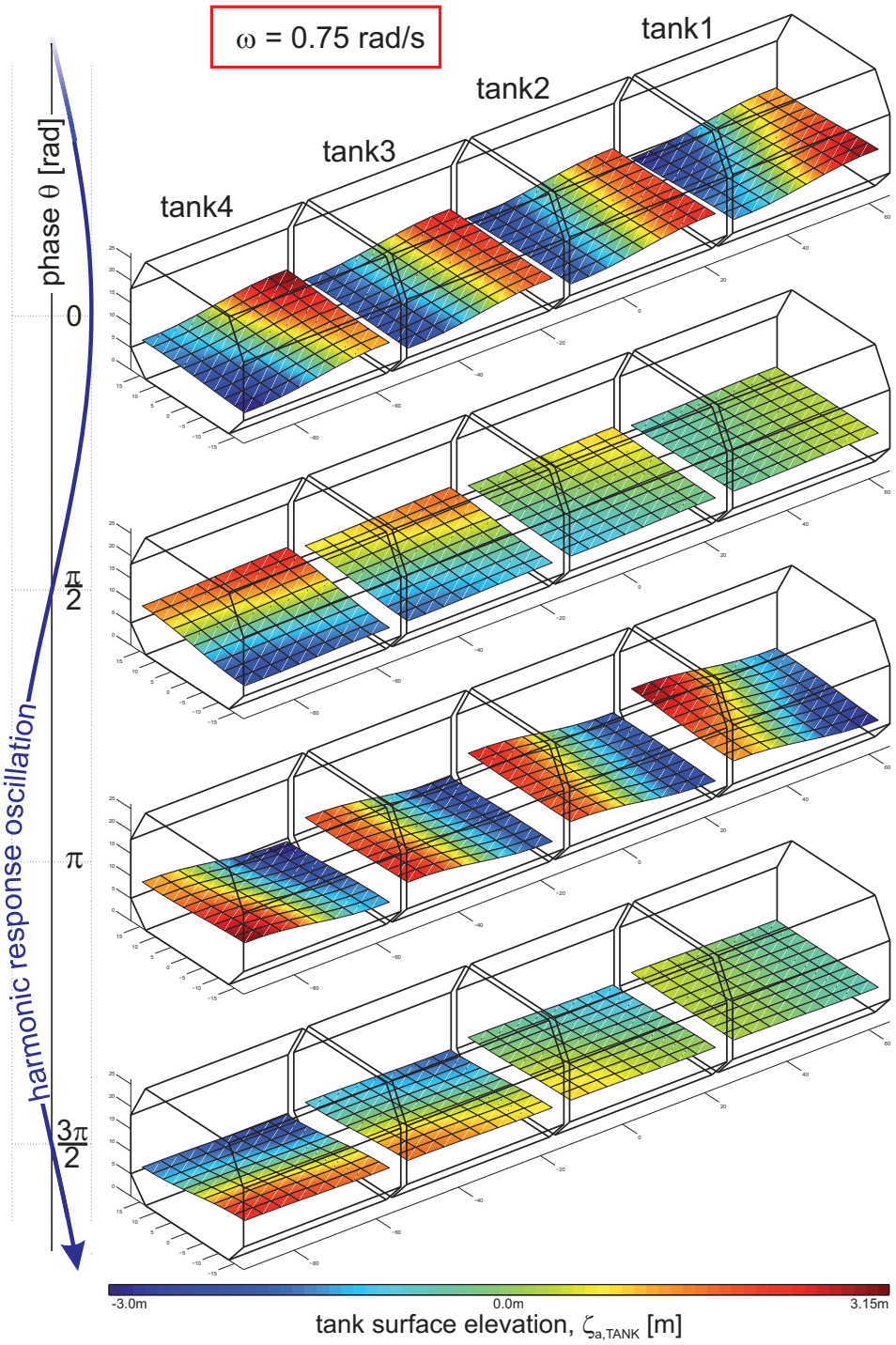


Figure 3.21: *Surface elevation of the internal fluid in all four tanks for $\omega = 0.75$ rad/s over one harmonic oscillating response period in four steps ($\theta = 0$, $\pi/2$, $\pi$ and $3/2\pi$): note that three-dimensional sloshing effects are observed in pure beam seas ($\beta = 90°$).*

three-dimensional response for an incident wave angle of exactly $\beta = 90°$ is a surprising phenomenon and is further investigated by visualizing the respective response over one period for all four tanks in Fig. 3.21. Strong longitudinal sloshing (see $\theta = 0$ rad and $\theta = \pi$ rad) and minor transverse sloshing (see $\theta = \pi/2$ rad and $\theta = 3/2\pi$ rad) is present in all four tanks. In particular the transverse component continuously decreases from tank 4 to tank 1 (refer to Fig. 3.11). Although the excitation is exactly symmetric (two-dimensional), the response is asymmetric (three-dimensional) and varies from tank to tank.

The cause for the observed surprising internal fluid behavior is determined by successive elimination of all asymmetries in the submerged hull geometry as well as in the mass distribution of the LNGC. The original hull geometry of the LNGC (geometry 1 in Fig. 3.22) is modified in two steps. First, the original hull shape is replaced by a rectangular box of equal dimensions ($L_{pp}$, $B_v$, $D_v$), where the new center of gravity of the hull alone is assumed to be located at the center of buoyancy of the box (geometry 2 in Fig. 3.22). In the second step, the four tanks are relocated from their original position (shifted towards the stern of the vessel) by 5.5 m towards the bow so that the tank arrangement becomes symmetric with respect to the vessel's center of buoyancy (geometry 3 in Fig. 3.22).

The influence of these variations on the LNGC motions as well as the internal fluid responses is exemplarily shown for tank 4 (stern), gauge 1

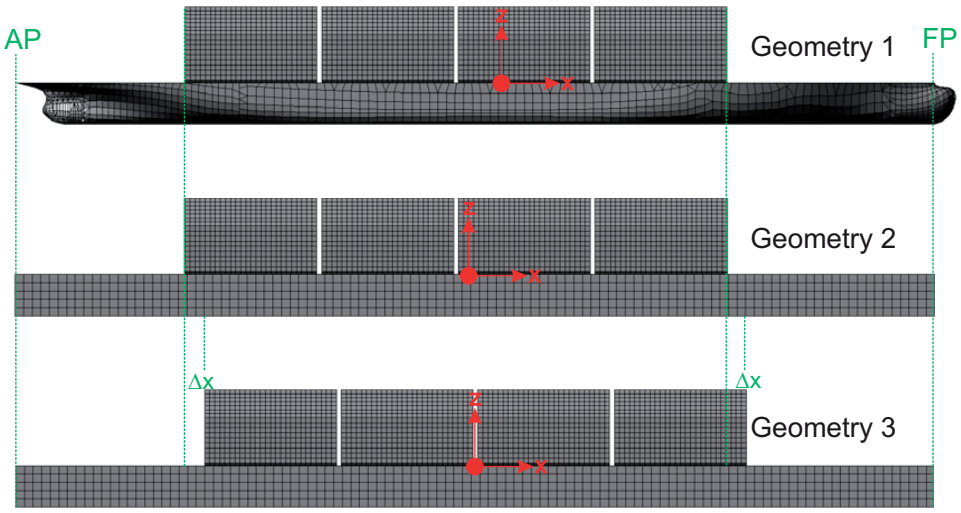


Figure 3.22: *Modification of the original LNGC geometry (1) in two steps: replacement of the hull by a rectangular box with evenly distributed masses (2), additional centering of the four cargo tanks (3).*

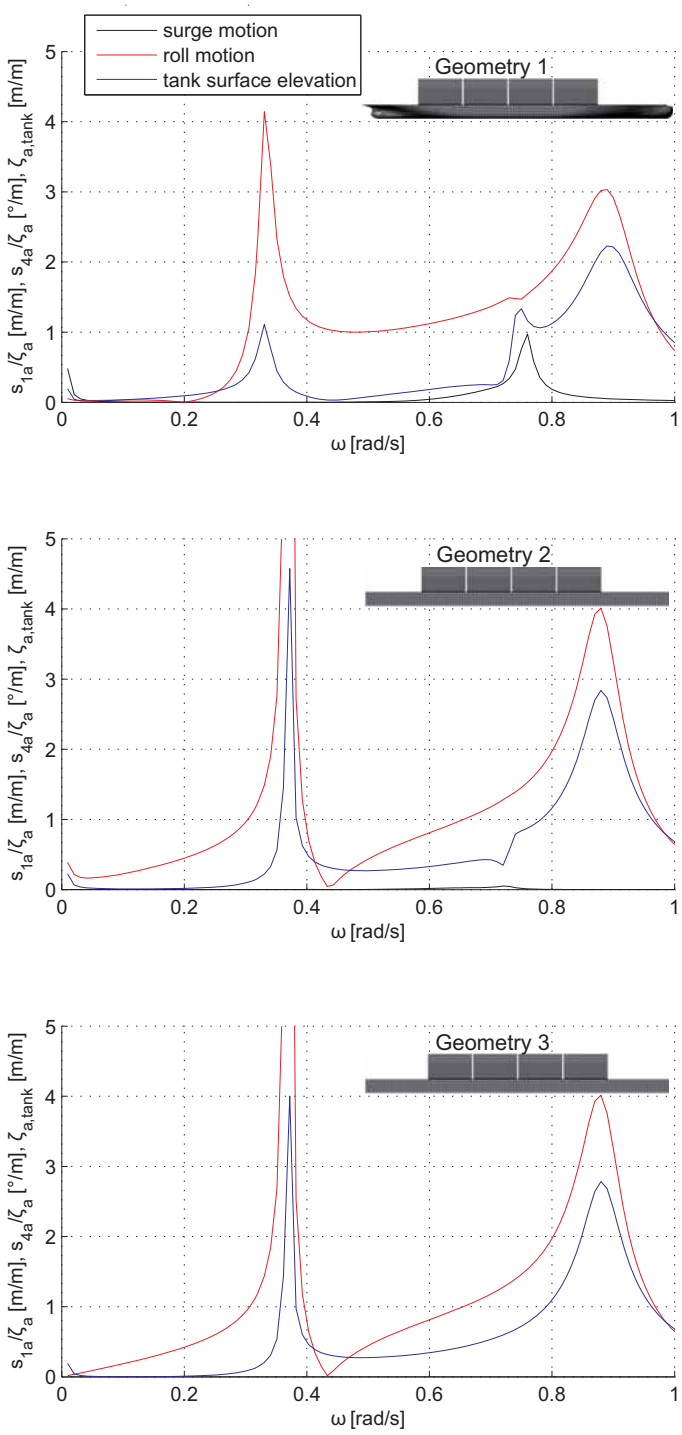


Figure 3.23: *Comparison of the surge motion RAO, roll motion RAO and internal surface elevation RAO (tank 4, gauge 1) for the original LNGC geometry (top), the box-shaped hull (center) and the symmetric tank arrangement (bottom). In all three cases, the filling height in all four tanks is 30% fresh water.*

(tank side wall) in Fig. 3.23, where numerical results for 30% water filling height (in all four tanks) in beam seas ($\beta = 90°$) are compared. For the original LNGC arrangement (geometry 1), the surface elevation features the characteristic three peaks: The peak at $\omega = 0.32$ rad/s is associated with the hull resonance that also appears in the roll motion RAO, the peak at $\omega = 0.75$ rad/s is the first longitudinal sloshing mode that leads to a surge response in beam seas and the third peak at $\omega = 0.90$ rad/s is the first transverse sloshing mode that is shifted by $\Delta\omega$ (see section 3.3.2) and is coupled with the LNGC roll motion.

The substitution of the LNGC hull shape for a box-shaped hull of equal outer dimensions (geometry 2) leads to significant changes. Due to the different hull shape, displacement and mass distribution of the box-shaped hull, the hull resonance has shifted to 0.37 rad/s while the impact of the first transverse sloshing mode remains at 0.90 rad/s. Instead of a minimum of 1 °/m, the roll motion now features a clear cancelation point at $\omega = 0.43$ rad/s. But most important, the fluid response peak at $\omega = 0.75$ rad/s is now much less pronounced and therefore the surge motions are negligible. Hence, the asymmetry of the LNGC hull is a major cause for the three-dimensional fluid response.

The symmetrical arrangement of tanks mounted to the box-shaped hull (geometry 3) finally leads to an ideal response in beam seas. The longitudinal component of the internal fluid response together with the surge motion has completely vanished. Internal surface elevations as well as roll motions both now exclusively feature transverse effects — the hull roll resonance and the impact of the first transverse sloshing mode.

Due to the coupling of internal fluid motions and vessel motions in the incident wave field, the three-dimensional characteristic of the internal surface elevation is associated with asymmetric LNGC responses. As shown in Fig. 3.24, model tests as well as numerical calculations confirm that the LNGC responses perpendicular to the direction of excitation are not negligi-

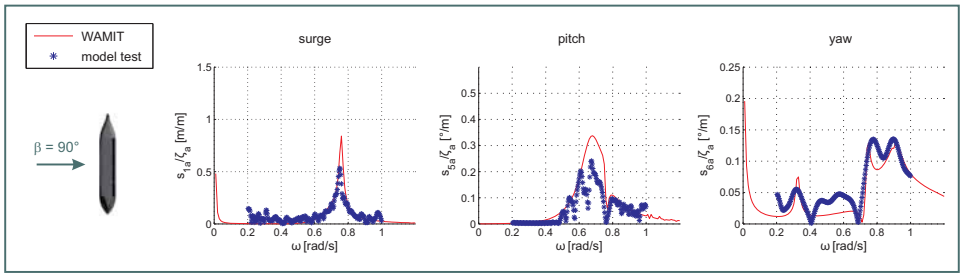


Figure 3.24: *Surge, pitch and yaw motion of the LNGC with 30% filling height (fresh water, $\rho_T = 998.2$ kg/m$^3$) in all four prismatic tanks: comparison of numerical calculations and model test data in beam seas ($\beta = 90°$).*

ble: although the vessel is exposed to pure beam seas, surge, pitch and yaw motions have to be considered. This finding is of particular importance for offshore offloading operations, where relative motions between two floating vessels are crucial. Simplifications with respect to the motion responses of a LNGC with partially filled tanks have to be considered with care.

## 3.4 Multi-Body Analysis

In the preceding sections, the LNGC alone was analyzed in various conditions in order to comprehend the influence of internal fluid motions on the seakeeping characteristics of the vessel. Now, an offshore offloading scenario including the LNGC and the FLNG terminal is considered, where both vessels constitute a multi-body system. Due to the vicinity of the vessels, the presence of the FLNG terminal alters the incident wave field for the LNGC in terms of scattering and radiation and vice versa (see also Clauss and Jacobsen (2004)). For two bodies instead of one, one additional scattering potential and six additional radiation potentials (a total of fifteen potentials) have to be considered in the potential theory approach, i.e. for $N$ bodies, Eq. (2.8) is expanded and becomes

$$\Phi = \Phi_0 + \underbrace{\sum_{j=1}^{N\cdot 6} \Phi_j}_{\text{radiation}} + \underbrace{\sum_{l=6\cdot N+1}^{6\cdot N+N} \Phi_l}_{\text{scattering}} \tag{3.18}$$

As a consequence of Eq. (2.23), which now comprises the radiation potentials for all $N$ bodies, hydrodynamic coupling in terms of coupled added mass and potential damping terms occurs. For two bodies, both matrices are 12×12 and fully populated. The restoring matrix is also 12×12 but no coupling terms exist. The motions for each body are now obtained from the expanded equation of motion in analogy to Eq. (2.22):

$$\sum_{j=1}^{6\cdot N} \left[-\omega^2 \left(m_{ij} + a_{ij}\right) - i\omega b_{ij} + c_{ij}\right] \; s_j = f_{ex,j} \tag{3.19}$$

and therefore also include the effects of hydrodynamic coupling (see also Newman (2001)).

The impact of hydrodynamic coupling on the seakeeping behavior is exemplified with the offshore loading procedure of the MPLS20 concept (see section 1.3). The LNGC approaches the FLNG terminal and enters the 'Mooring Bay' at the stern of the vessel. At a distance of 10 m, the shuttle carrier is moored to the terminal in a symmetrical arrangement of six mooring lines. During the cargo transfer from the FLNG terminal to the LNGC, the carrier maintains a constant draft of 12 m, which is achieved

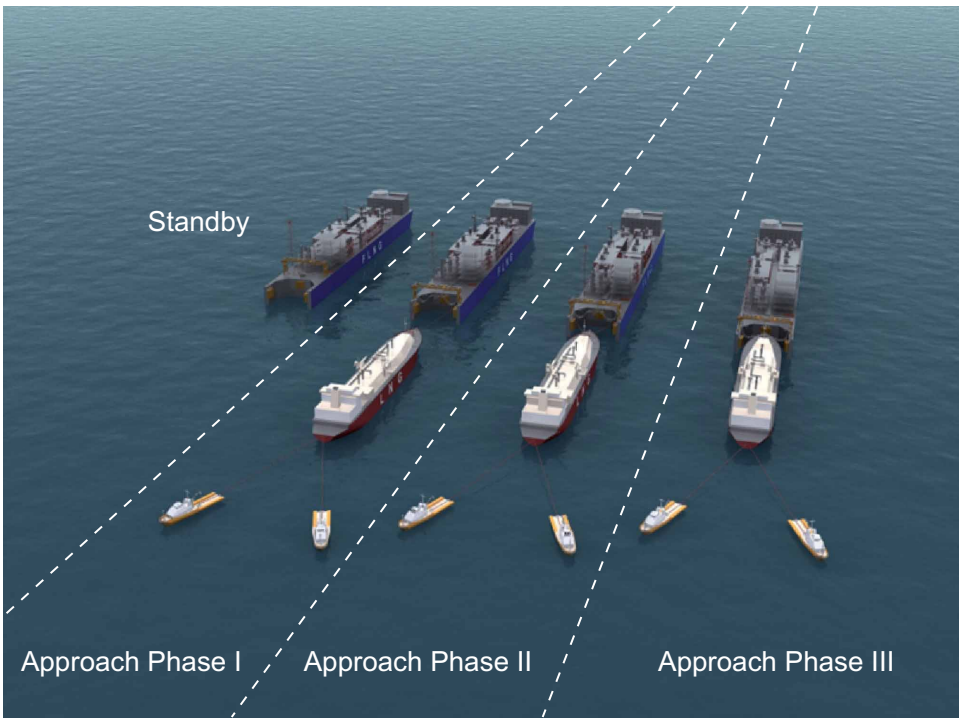


Figure 3.25: *Impression of the MPLS20 offloading procedure: approach of the LNGC to the 'Mooring Bay' of the FLNG terminal in three steps (Phase I: distance 100 m, Phase II: distance 50 m, Phase III: distance 10 m).*

by ballasting operations. The entire procedure is broken down intro 22 numerical calculations, which represent the following conditions, that are also visualized in Fig. 3.25:

1. Approach Phase I: LNGC in line with the FLNG terminal, distance 100 m, LNGC in ballast
2. Approach Phase II: LNGC in line with the FLNG terminal, distance 50 m, LNGC in ballast
3. Approach Phase III: LNGC in line with the FLNG terminal, distance 10 m, LNGC in ballast

4.-22. Transfer Phase: LNGC in line with the FLNG terminal, distance 10 m, LNGC filling levels from 5% to 95% in steps of 5%

### Approach Phase

For the investigation of the approach phase, that is subdivided into three steps, it is assumed that the LNGC is in ballast (the numerical setup is

identical to the case that is referred to as 'solid filling' in section 3.3) and orientated in line with the FLNG terminal. An ideal situation with head seas ($\beta = 180°$) is exemplarily considered. In Fig. 3.26, the relevant motion RAOs for this condition — i.e. surge, heave and pitch — of the LNGC and the FLNG terminal are compared to the results for the single-body cases (distance between FLNG terminal and LNGC $\infty$). It already becomes clear at the first glance, that the motion alteration of the larger FLNG terminal caused by the presence of the smaller LNGC (for dimensions see Tab. 1.2), which is positioned downstream, are negligible. Surge, heave and pitch motions for all three approach phases in multi-body configuration are practically identical to the motion amplitudes for the FLNG terminal alone.

However, the motion behavior of the LNGC is significantly influenced by the presence of the larger FLNG terminal that is situated upstream and shadows the carrier from the incident wave field to some extend. The difference between the single-body RAOs of the carrier and the RAOs for the multi-body configurations is clearly visible. The motion amplitudes — especially the heave and pitch motions — are decreased and in case of the pitch motion, the peak of the RAOs is also shifted from $\omega = 0.41$ rad/s to 0.36 rad/s. For the approaching of the LNGC from 100 m (Phase I) to 50 m (Phase II) and finally 10 m (Phase III), the shielding effect of the terminal is slightly increasing with decreasing distance between the two bodies.

### Transfer Phase

Once the LNGC is safely moored in the 'Mooring Bay' at a distance of 10 m to the stern of the FLNG terminal, a rail-mounted movable loading crane, that bridges the 'Mooring Bay' from one wing to the other places the header on the LNGC receiving manifold. After the connection is established, LNG is transferred from the storage tanks of the FLNG terminal into the four prismatic cargo tanks of the LNGC, which maintains a constant draft of 12 m during the entire procedure due to active ballasting. Although the inner diameter of the cryogenic transfer pipes is 16" — which is relatively large compared to current standards — and thus provides high mass flow, the loading procedure takes approx. 18 to 24 hours. The material properties and strength of the corrugated pipe allow only restricted motions. Torsion cannot be accommodated at all and the limited bending radius of the pipe implies that the relative motions of the coupling points on the LNGC and the FLNG terminal (see red dots in Fig. 3.27) should not exceed a certain threshold in order to ensure safe offshore transfer operations.

In the potential theory calculations, the continuous increase of liquid cargo inside the four prismatic tanks onboard the LNGC is modeled by 19 discrete LNG filling levels from 5% to 95% with associated changes in the rigid body (hull plus ballasting) mass, mass moments of inertia and

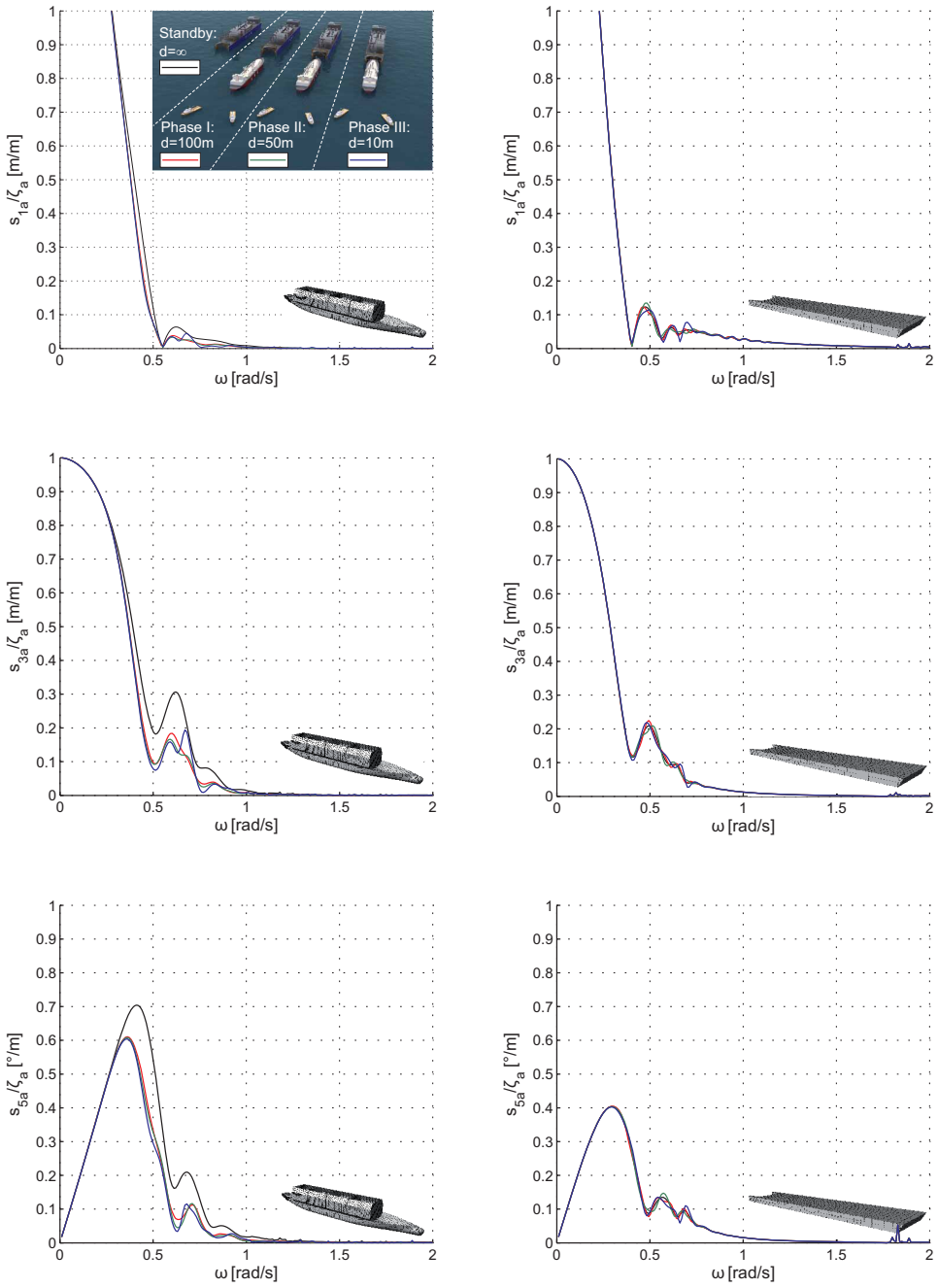


Figure 3.26: *Comparison of the surge, heave and pitch RAOs of LNGC (left) and FLNG terminal (right) in multi-body arrangement for the three approach phases with the respective single-body RAOs ($\beta = 180°$)*

the location of the vessel's center of gravity. The mooring arrangement between LNGC and FLNG terminal is neglected in the calculations. This simplification is legitimate since only first order motions are considered, which cannot be suppressed. Moorings are designed to restrain second order effects like drift, but have to be veered by winches in order not to be damaged by first order motions. From roll and pitch decay tests with 30% water filling in all four prismatic tanks, the ratio of viscous damping to critical damping $\delta$ is determined to be 2.7% for roll damping and 13.1% for pitch damping. These parameters are kept constant for all calculations of the transfer phase (all input values are listed in Appendix A). Each calculation run encompasses 72 incident wave angles, $0° \leq \beta \leq 360°$. Assuming linearity, i.e. small roll, pitch and yaw angles, the absolute translatory motions of each coupling point can be calculated as follows

$$\begin{bmatrix} s_x \\ s_y \\ s_z \end{bmatrix} = \begin{bmatrix} 1 & -s_6 & s_5 \\ s_6 & 1 & -s_4 \\ -s_5 & s_4 & 1 \end{bmatrix} \cdot \begin{bmatrix} r_x \\ r_y \\ r_z \end{bmatrix} + \begin{bmatrix} s_1 \\ s_2 \\ s_3 \end{bmatrix}, \tag{3.20}$$

where the distance from the origin of the respective body-fixed coordinate system to the coupling point is denoted by $r_x$, $r_y$ and $r_z$. As described by Clauss et al. (2009), Eq. (3.20) can be equivalently expressed by

$$\begin{bmatrix} s_x \\ s_y \\ s_z \end{bmatrix} = \begin{bmatrix} s_4 \\ s_5 \\ s_6 \end{bmatrix} \times \begin{bmatrix} r_x \\ r_y \\ r_z \end{bmatrix} + \begin{bmatrix} s_1 \\ s_2 \\ s_3 \end{bmatrix} \quad \text{and} \quad \begin{bmatrix} s_\varphi \\ s_\vartheta \\ s_\psi \end{bmatrix} = \begin{bmatrix} s_4 \\ s_5 \\ s_6 \end{bmatrix} \tag{3.21}$$

The relative motions of the coupling points (see Fig. 3.27) can now be obtained by calculating the absolute values of the motion differences in terms of complex numbers (containing phase information) for each degree of freedom:

$$\begin{bmatrix} s_{relx} \\ s_{rely} \\ s_{relz} \\ s_{rel\varphi} \\ s_{rel\vartheta} \\ s_{rel\psi} \end{bmatrix} = \left| \begin{bmatrix} s_{x,FLNG} \\ s_{y,FLNG} \\ s_{z,FLNG} \\ s_{\varphi,FLNG} \\ s_{\vartheta,FLNG} \\ s_{\psi,FLNG} \end{bmatrix} - \begin{bmatrix} s_{x,LNGC} \\ s_{y,LNGC} \\ s_{z,LNGC} \\ s_{\varphi,LNGC} \\ s_{\vartheta,LNGC} \\ s_{\psi,LNGC} \end{bmatrix} \right| \tag{3.22}$$

Conducting this procedure for the multi-body system with 19 filling heights, 72 incident wave angles, 6 degrees of relative motion and 200 wave frequencies results in a four-dimensional data array, which makes a comprehensive graphical visualization impossible. In order to get an impression of the relative motions, exemplary three-dimensional graphs for special cases are presented.

At first, the relative motions of the coupling points in six degrees of freedom for all incident wave angles are compiled in three-dimensional polar graphs for the standard filling case of 30% LNG filling height. For each

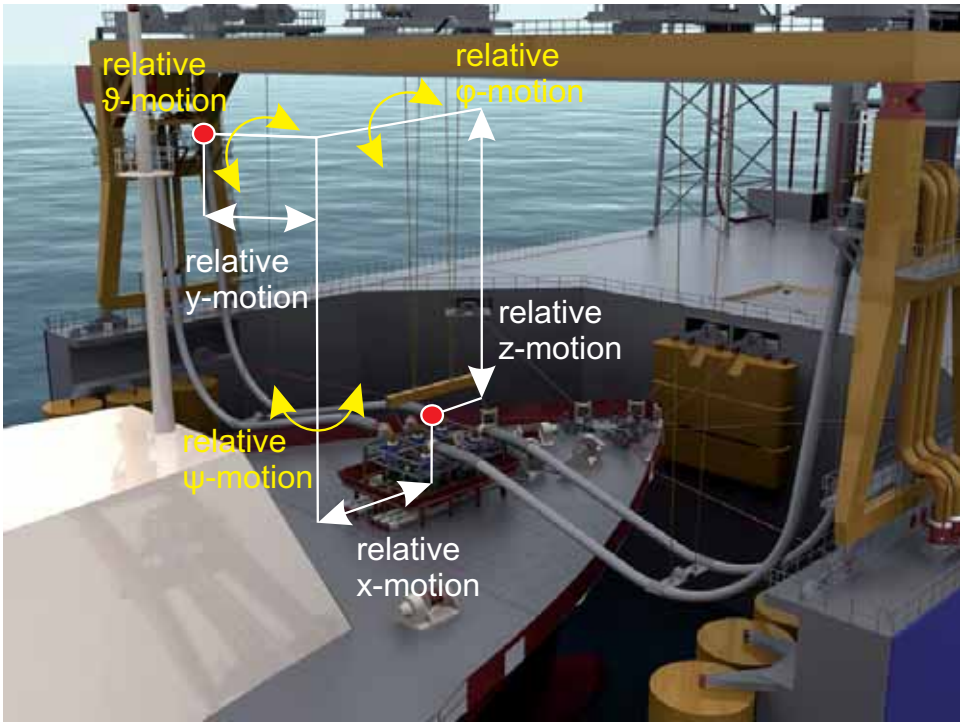


Figure 3.27: *Visualization of the coupling points of the LNG transfer system (red dots) at the receiving manifold on the LNGC bow deck and at the loading bridge of the FLNG terminal. The associated relative translatory and rotatory motions of the coupling points are indicated.*

degree of freedom, one exemplary incident wave angle is selected and the corresponding two-dimensional RAO is shown next to the polar graph in order to clarify this kind of representation. Fig. 3.28 shows the three translatory relative motions for all incident wave angles and 30% filling height. The relative $x$-motion (top) features its maximum of slightly more than $\pm 3$ m per meter wave amplitude in very long waves ($0$ rad/s $< \omega < 0.2$ rad/s) and head to bow quartering seas ($160° < \beta < 200°$) as well as following to stern quartering seas ($320° < \beta < 40°$). At $\omega = 0.69$ rad/s, all relative $x$-motion RAOs feature a peak of $\approx 0.5$ m per meter wave amplitude, which results in a ring-shaped formation in the polar graph. A comparison with Fig. 3.18 reveals that this ring is caused by the first longitudinal sloshing mode of the prismatic tanks at 30% LNG filling height. In the center part of Fig. 3.28, the relative $y$-motion is shown. The maximum values of $\approx 8$ m per meter wave amplitude occur in beam seas ($60° < \beta < 120°$ as well as $240° < \beta < 300°$). Although there is no complete ring caused by

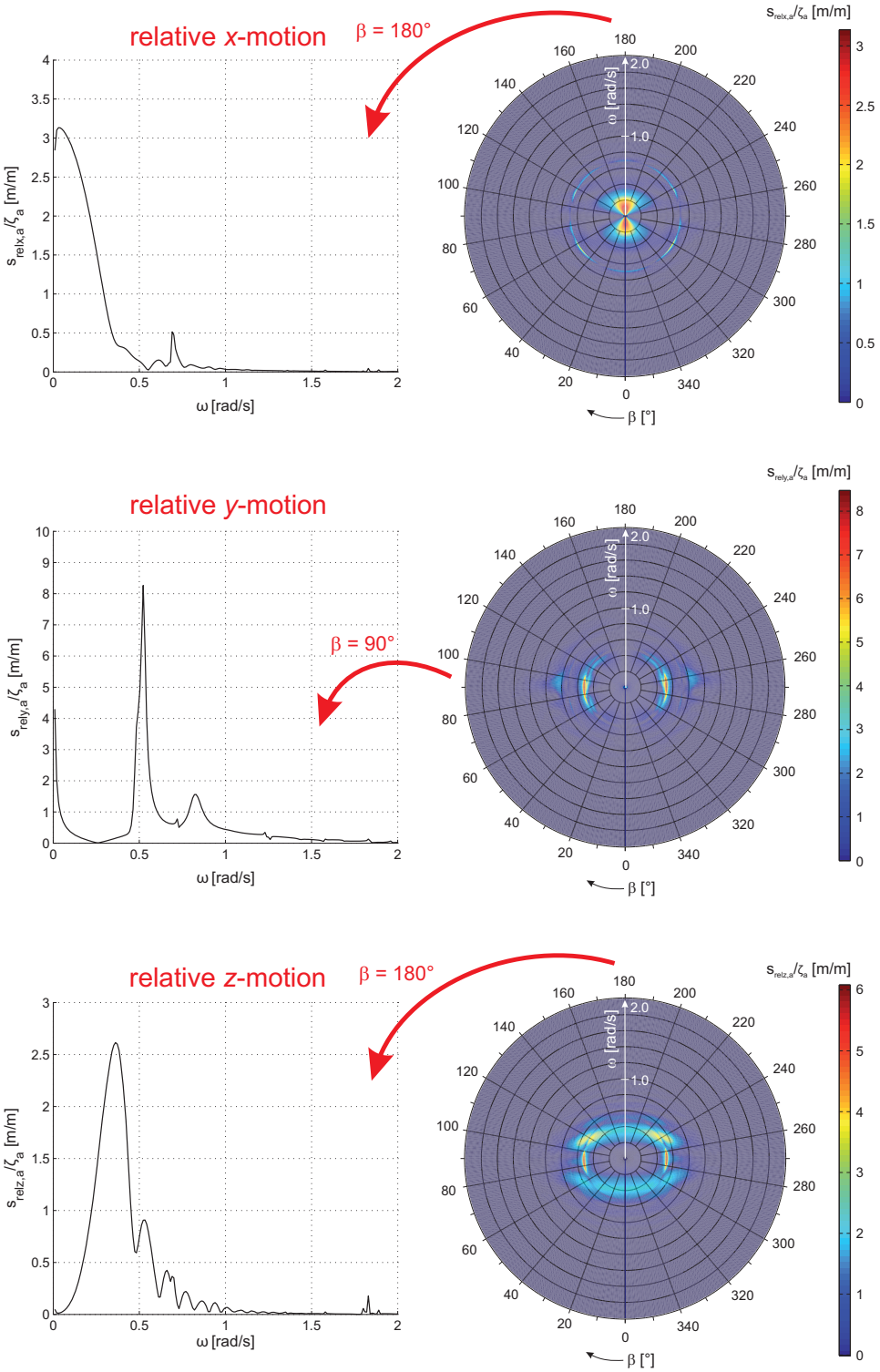


Figure 3.28: *Translatory relative motions in x- (top), y- (center) and z-direction (bottom) of the coupling points of the LNG transfer pipe for 30% LNG filling height in all four tanks. The polar diagrams on the right-hand side show the respective RAOs for all incident wave angles $0° \leq \beta \leq 360°$, while RAOs for exemplary incident wave angles are presented on the left-hand side.*

peaks across all incident wave angles, there are two distinct peak regions in beam sea conditions, which is particularly visible in the exemplary relative $y$-motion RAO for $\beta = 90°$ on the left-hand side. The lower frequency peak at $\omega = 0.52$ rad/s is caused by the rigid body roll resonance of the FLNG terminal, while the peak at $\omega = 0.82$ rad/s (magnitude $\approx \pm 1.5$ m per meter wave amplitude) is related to the first transverse sloshing mode of the prismatic tanks (cf. Fig. 3.18, top). The relative $z$-motions of the coupling points in head and following seas are dominated by the pitch motions of the LNGC (maximum values $\approx \pm 2.5$ m per meter wave amplitude), while in beam seas, pure heave motions cause the relative deflections (maximum motions twice as high as in head seas: $\approx \pm 3$ m per meter wave amplitude). In bow quartering seas, the influence of the first transverse sloshing mode at $\omega = 0.52$ rad/s is apparent, leading to relative $z$-motions of $\pm 2.5$ m per meter wave amplitude.

The three rotatory motions for all incident wave angles and 30% LNG filling height are compiled in Fig. 3.29. The maximum amplitudes of the relative $\varphi$-motion of the coupling points (top of the figure) occur in beam seas ($\beta = 90°$ and $\beta = 270°$). This motion, which is equivalent to the relative roll motion between FLNG terminal and LNGC, features two distinct peaks (see the exemplary RAO for $\beta = 90°$ on the left-hand side): One low-frequency peak, which comprises the FLNG terminal's rigid body roll resonance at $\omega = 0.52$ rad/s and the LNGC rigid body roll resonance for the 30% filling height case as a local maximum at $\omega = 0.48$ rad/s as well as one high-frequency peak at $\omega = 0.82$ rad/s, which is related to the first transverse sloshing mode of the prismatic tanks onboard the LNGC at 30% LNG filling height (cf. Fig. 3.18, bottom). While the impact of transverse sloshing is noticeable in beam seas exclusively, where it reaches maximum values about $\pm 5°$ per meter wave amplitude, the rigid body resonance modes cause significant relative $\varphi$-motions in bow and stern quartering seas as well. Here, maximum motion amplitudes of about $\pm 14°$ per meter wave amplitude can be observed. The relative $\vartheta$-motion, which is equivalent to the relative pitch motion, is shown in the center part of Fig. 3.29. From the comparison of the pattern in the polar graph (right-hand side) and the exemplary RAO for $\beta = 180°$ (left-hand side) with the relative $z$-motion visualization in Fig. 3.28, it becomes clear that the vertical relative motion of the coupling points is dominated by the pitch motion of the two vessels. This is not surprising, since the coupling points are located at a great distance from the respective centers of rotation. The relative $\varphi$-motion is significant for almost the entire range of incident wave angles, except for pure beam seas ($80° < \beta < 100°$ and $260° < \beta < 280°$) and reaches maximum amplitudes of slightly more than $\pm 1°$ per meter wave amplitude in the lower frequency region (the maximum for $\beta = 180°$ is located at $\omega = 0.28$ rad/s). Apart from slight impacts in bow quartering seas of $\beta = 120°$ and $\beta = 240°$, respectively,

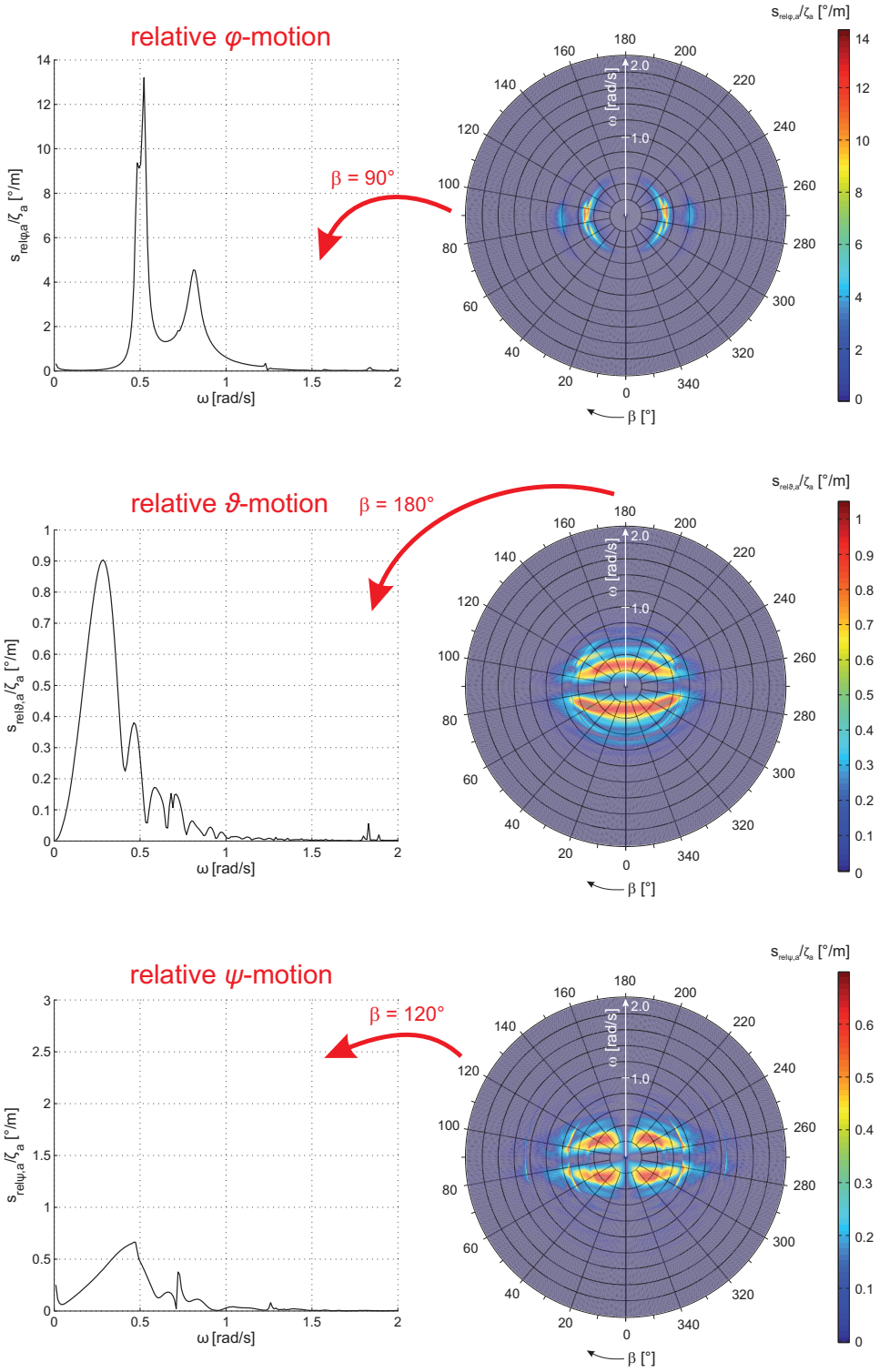


Figure 3.29: *Rotatory relative motions in $\varphi$- (top), $\vartheta$- (center) and $\psi$-direction (bottom) of the coupling points of the LNG transfer pipe for 30% LNG filling height in all four tanks. The polar diagrams on the right-hand side show the respective RAOs for all incident wave angles $0° \leq \beta \leq 360°$, while RAOs for exemplary incident wave angles are presented on the left-hand side.*

the relative pitch motion is not significantly influenced by sloshing effects. In the bottom part of Fig. 3.29, the relative $\psi$-motion of the coupling points of the LNG transfer pipe — which is equivalent to the relative yaw motion — is represented as a three-dimensional polar graph (right-hand side) as well as an exemplary two-dimensional RAO for $\beta = 120°$ on the left-hand side. Maximum motion amplitudes of $\approx \pm 0.7°$ per meter wave amplitude occur in bow and stern quartering seas around $\omega = 0.48$ rad/s — amplified by the LNGC rigid body roll resonance — while in head, following and beam seas, responses are negligible. A secondary peak of $\pm 0.5°$ per meter wave amplitude occurs at $\omega = 0.73$ rad/s. According to Fig. 3.19, the amplification of motions at this frequency is related to transverse sloshing effects.

While in the previous graphs, relative motion RAOs for all incident wave angles were shown for the standard case of 30% filling height exclusively, the four-dimensional data is now visualized by cartesian three-dimensional graphs, showing the six relative motion RAOs in dependency of the internal tank filling height at one representative incident wave angle per degree of freedom. In Fig. 3.30, the translatory relative motions of the coupling points for the cryogenic transfer pipe are presented in perspective (left-hand side) as well as plan view (right-hand side) in order to give a better impression of the motion characteristics in dependency of the LNG filling height. For all filling heights, the relative $x$-motion ($\beta = 180°$, top) features maximum amplitudes of $\approx \pm 3$ m per meter wave amplitude in very long waves ($\omega \rightarrow 0$). Especially from the plan view, the progression of the secondary peak — which is related to the first longitudinal sloshing mode of the equally filled four prismatic tanks — becomes traceable (cf. Fig. 3.18, bottom). The relative $y$-motion for $\beta = 90°$ in the center of the figure reveals three significant characteristics: The maximum motion amplitudes of $\approx \pm 8$ m per meter wave amplitude are located on a straight ridge at $\omega = 0.52$ rad/s, which is obviously caused by the rigid body roll resonance of the FLNG terminal. A less pronounced and slightly meandering ridge is located close to the FLNG terminal's rigid body roll resonance on the low-frequency side and is related to the rigid body resonance of the LNGC. The progression of this ridge is owed to the fact that the ratio of rigid to liquid mass of the system is continuously decreasing with increasing filling height and the height of the center of gravity of the remaining rigid mass is changing at the same time. First order transverse sloshing effects finally cause the third characteristic feature of the relative $y$-motion: With increasing filling height, the frequency of the related peaks increases in analogy to Fig. 3.18 (top). As expected, the cartesian three-dimensional visualization of the relative $z$-motion ($\beta = 180°$, bottom of Fig. 3.30) features no sloshing related effects, but a clear domination of the pitch motion influence on the absolute vertical motion of the coupling points. Maximum motion amplitudes of $\approx \pm 2.5$ m per meter wave amplitude occur on a rather broad straight ridge located at $\omega = 0.36$ rad/s for all filling heights.

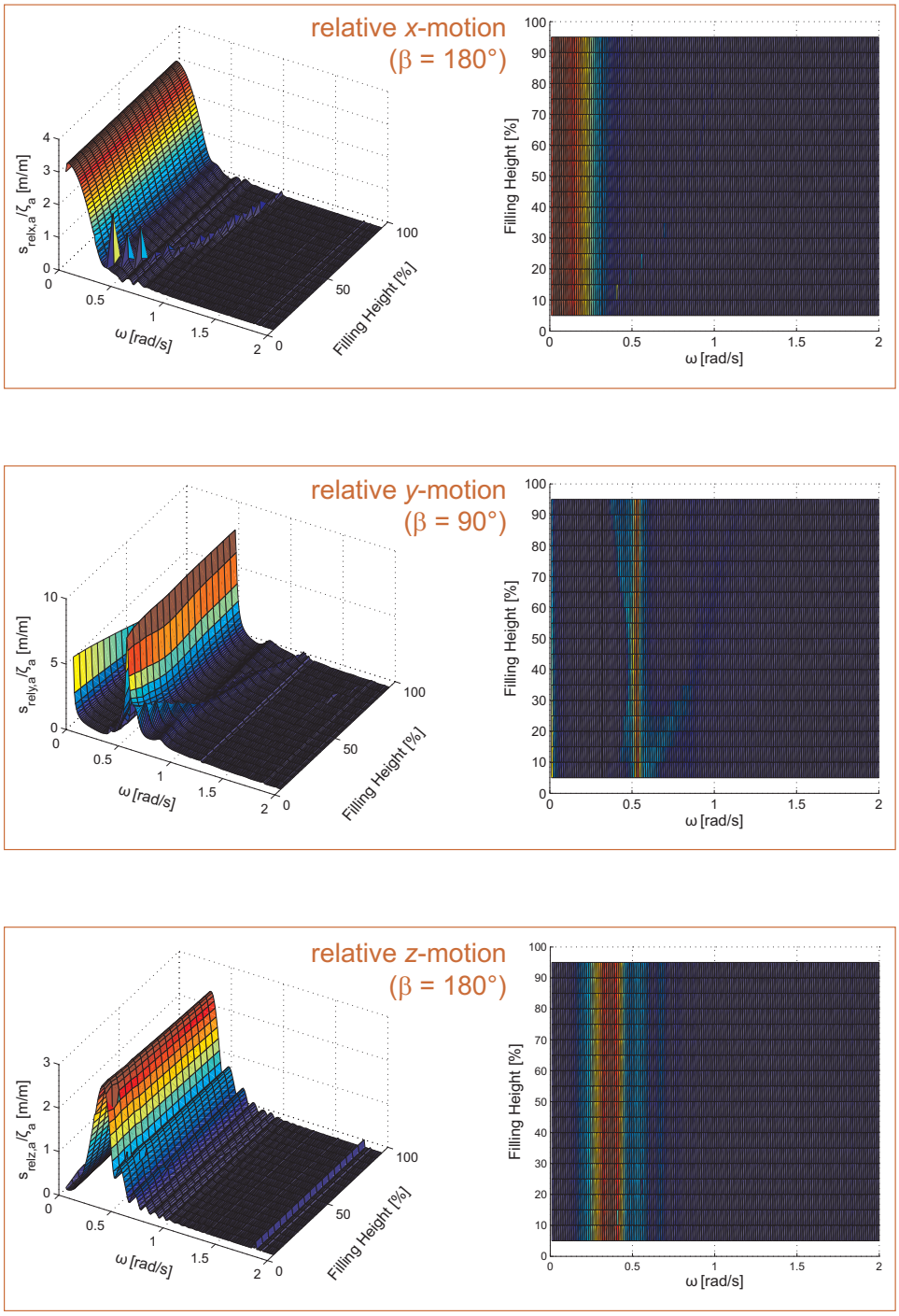


Figure 3.30: *Translatory relative motions of the coupling points of the LNG transfer pipe in x- (top), y- (center) and z-direction (bottom) for selected incident wave angles and all LNG filling heights (5% to 95%).*

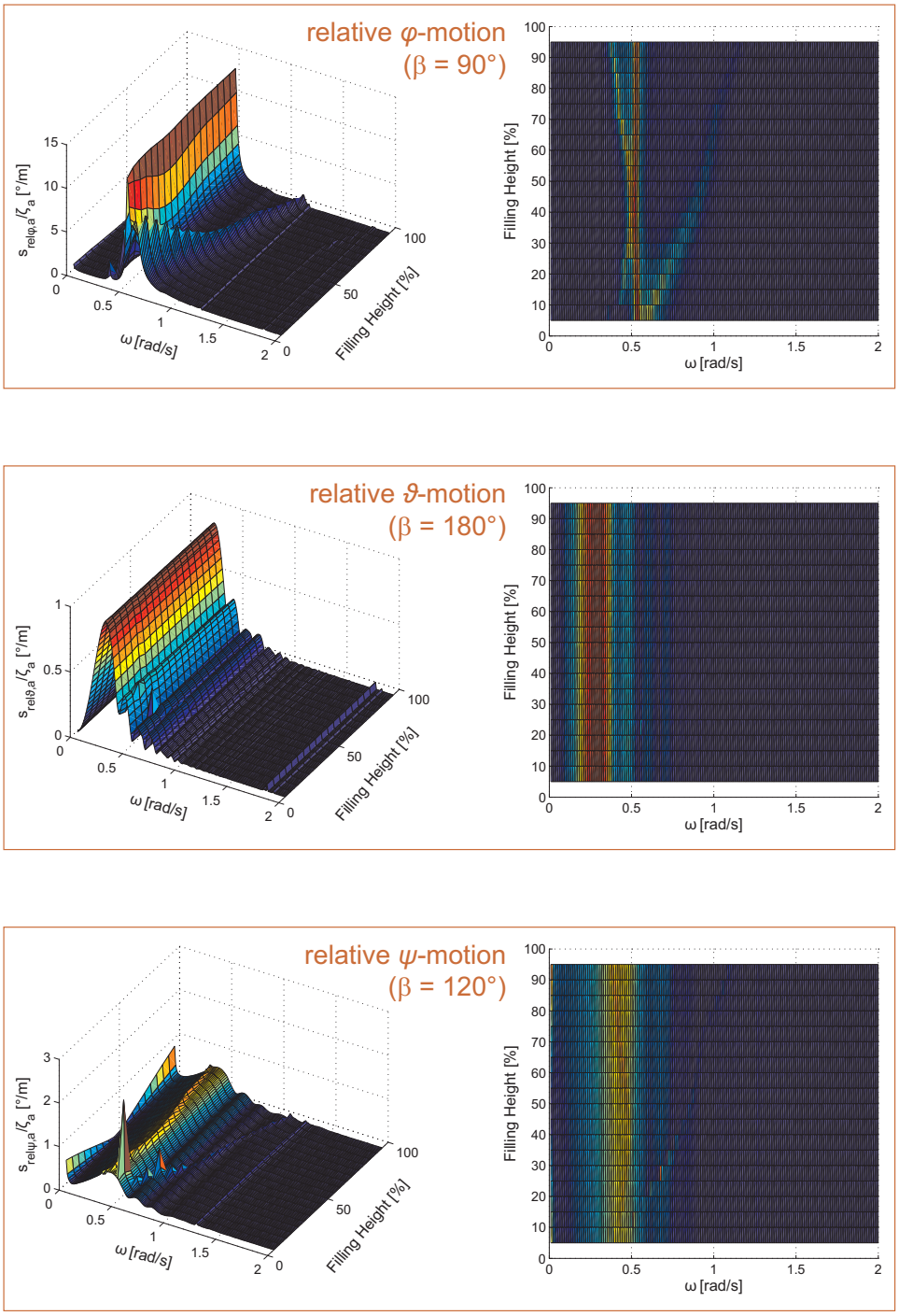


Figure 3.31: *Rotatory relative motions of the coupling points of the LNG transfer pipe in φ- (top), ϑ- (center) and ψ-direction (bottom) for selected incident wave angles and all LNG filling heights (5% to 95%).*

The rotatory relative motions in three-dimensional cartesian graphs for all filling heights and representative incident wave angles are presented in Fig. 3.31. In the upper part of this figure, the relative $\varphi$- or relative roll motion of the coupling points of the transfer pipe is shown for $\beta = 90°$. A qualitative agreement of the motion characteristics can be identified from the comparison of the relative roll motion characteristics with the relative $y$-motion (cf. Fig. 3.28, center): maximum motion amplitudes of $\approx \pm 13°$ per meter wave amplitude are caused by the FLNG terminal's rigid body roll resonance at $\omega = 0.52$ rad/s. Secondary peaks are caused by the LNGC rigid body roll resonance (0.35 rad/s $\leq \omega \leq$ 0.43 rad/s) and the first transverse sloshing mode (0.6 rad/s $\leq \omega \leq$ 1.18 rad/s). The characteristics of the relative $\vartheta$- or relative pitch motion for $\beta = 180°$ (center part of the figure) agree qualitatively with the relative $z$-motion in Fig. 3.28 (bottom). This is attributed to fact that the vertical motion ($z$-motion) is dominated by the pitch motion component, since the coupling points are located at a great distance to the vessels' centers of rotation: at the bow (LNGC) and the stern (FLNG terminal), respectively. Maximum values of $\approx \pm 1°$ per meter wave amplitude occur on a broad straight ridge at $\omega = 0.28$ rad/s. As the relative $z$-motion, the relative pitch motion is also not significantly influenced by internal tank sloshing. The progression of the relative $\psi$- or relative yaw motion on the other hand is characterized by sloshing and lateral motion coupling effects ($\beta = 120°$, cf. Fig. 3.31, bottom). In the frequency range 0.35 rad/s $\leq \omega \leq$ 0.43 rad/s, a meandering ridge — which is induced by roll-yaw motion coupling — causes maximum relative motion amplitudes of $\approx \pm 0.4$ ° per meter wave amplitude. Transverse sloshing effects lead to secondary peaks whose frequency of occurrence increases with increasing filling height (cf. top of Fig. 3.18). Please note, that (as for all resonant effects) the height of these peaks and respective motion amplitudes should not be treated linearly.

The four-dimensional data array obtained from the multi-body analysis in the transfer phase contains all necessary information on the system characteristics of FLNG terminal and LNGC during the entire offloading procedure. With given maximum tolerable values regarding the relative motions of the coupling points of the cryogenic transfer pipe, the operational range of the system can be determined for any given offshore location. This procedure is exemplarily shown in the following section.

## 3.5 Stochastic Analysis

For the operating company, it is important to gain knowledge how the limiting parameters — i.e. the maximum tolerable relative motions of the coupling points of the cryogenic transfer pipe — influence the operational range of the entire system. From an economical point of view, it is certainly fa-

vorable to optimize the system in order to achieve a minimum annual downtime for the designated location of operation, or in other words to be able to transfer LNG from a FLNG terminal to a LNGC whenever desired or necessary. In this chapter, the MPLS20 system is exemplarily investigated at the *Haltenbanken* region, 150 km off the coast of Norway and 200 km south of the Arctic Circle. The limiting motion parameters for the subsequent calculations correspond to the values that have been established for offloading operations with the 16" vacuum insulated transfer pipes that have been developed in the framework of the MPLS20 joint research project. The strength of the pipe structure allows bending up to certain minimum radii, which — in combination with the guidance of the pipe — leads to maximum tolerable relative motions of the pipe coupling points of ±2 m in $x$-direction and ±5 m in $z$-direction (cf. Fig. 3.27).

### 3.5.1 Worst Case Identification

The duration of the offloading procedure is estimate to be 18 to 24 hours. Within this period, the multi-body system consisting of the FLNG terminal and the LNGC might be exposed to any sea state in any possible combination of filling height and incident wave angle. Therefore, the worst case, or rather maximum response, for all relevant filling heights and incident wave angles is determined.

At first, the four-dimensional data array is reduced to a three-dimensional matrix by determining the worst case scenario with respect to the 19 discrete tanks filling heights that are analyzed. For each wave frequency $\omega$ and incident wave angle $\beta$, the maximum amplitude from the filling height-depending relative $x$- and relative $z$-motion RAOs is determined, i.e. the amount of relevant data is reduced from 5.47E5 to 2.88E4 values.

During the LNG transfer process, the turret mooring allows the FLNG terminal to perform weather vaning motions due to combined environmental loads resulting from waves, wind and currents. It is assumed that these motions lie within a certain range that implies incident wave angles of $150° \leq \beta \leq 210°$, in other words the terminal's orientation – and therefore the orientation of the entire system — might change about ±30° with respect to the main wave direction (head sea condition) during the transfer phase. This restriction to 13 relevant incident wave angles leads to a further decrease of data to 5,200 values.

The relative $x$-motion which results from the worst case analysis regarding the tank filling height is illustrated in Fig. 3.32, where the angular range relevant for weather vaning is separately accentuated in the upper part of the figure. Since the influence of all 19 investigated discrete filling heights is combined in these RAOs, multiple circular structures can be observed in

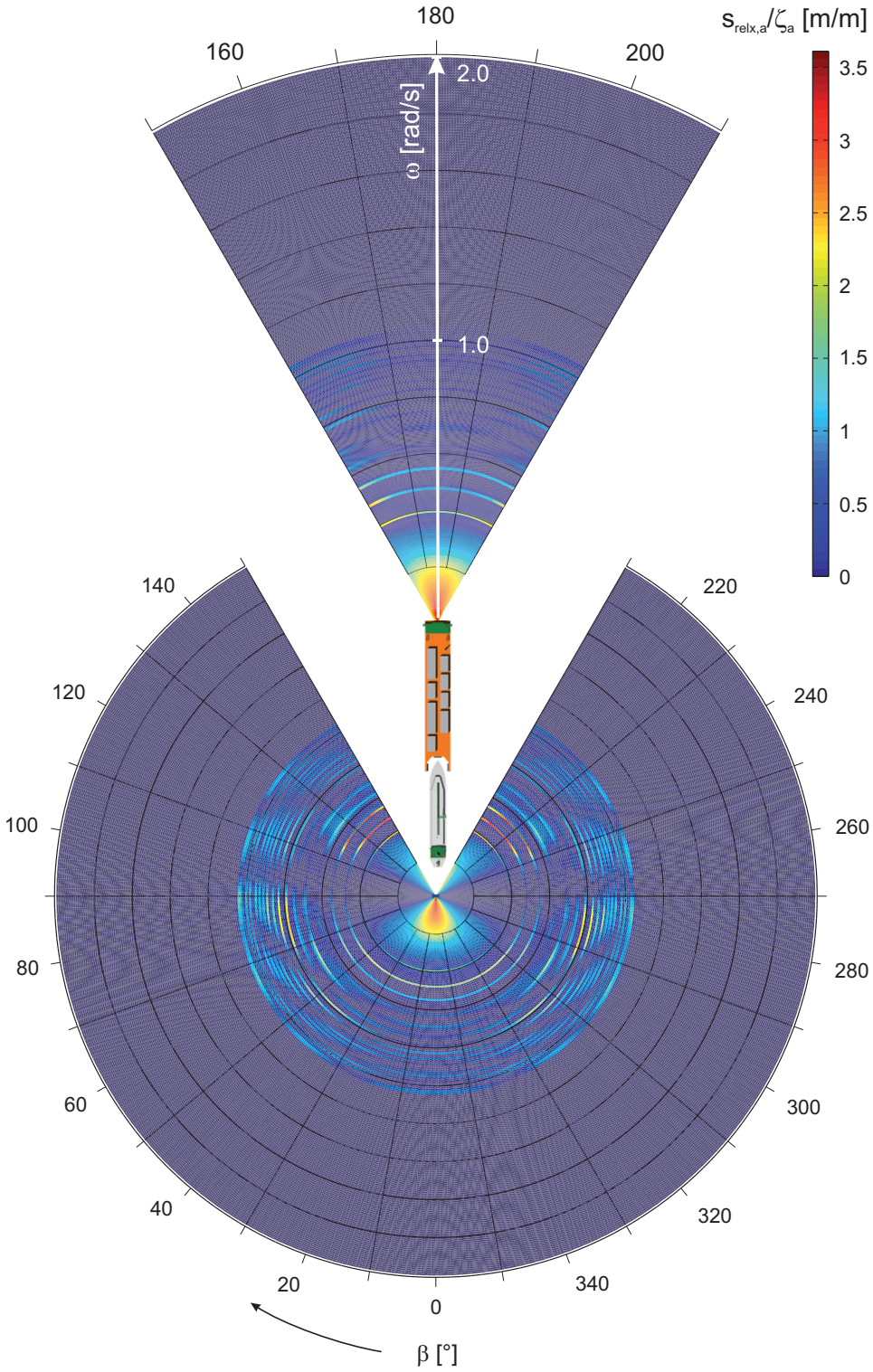


Figure 3.32: *Relative $x$-motion amplitudes of the coupling points of the transfer pipe resulting from the worst case analysis with respect to the filling height during the transfer period. The relevant incident wave angles lie within the weather vaning range ($150° \leq \beta \leq 210°$).*

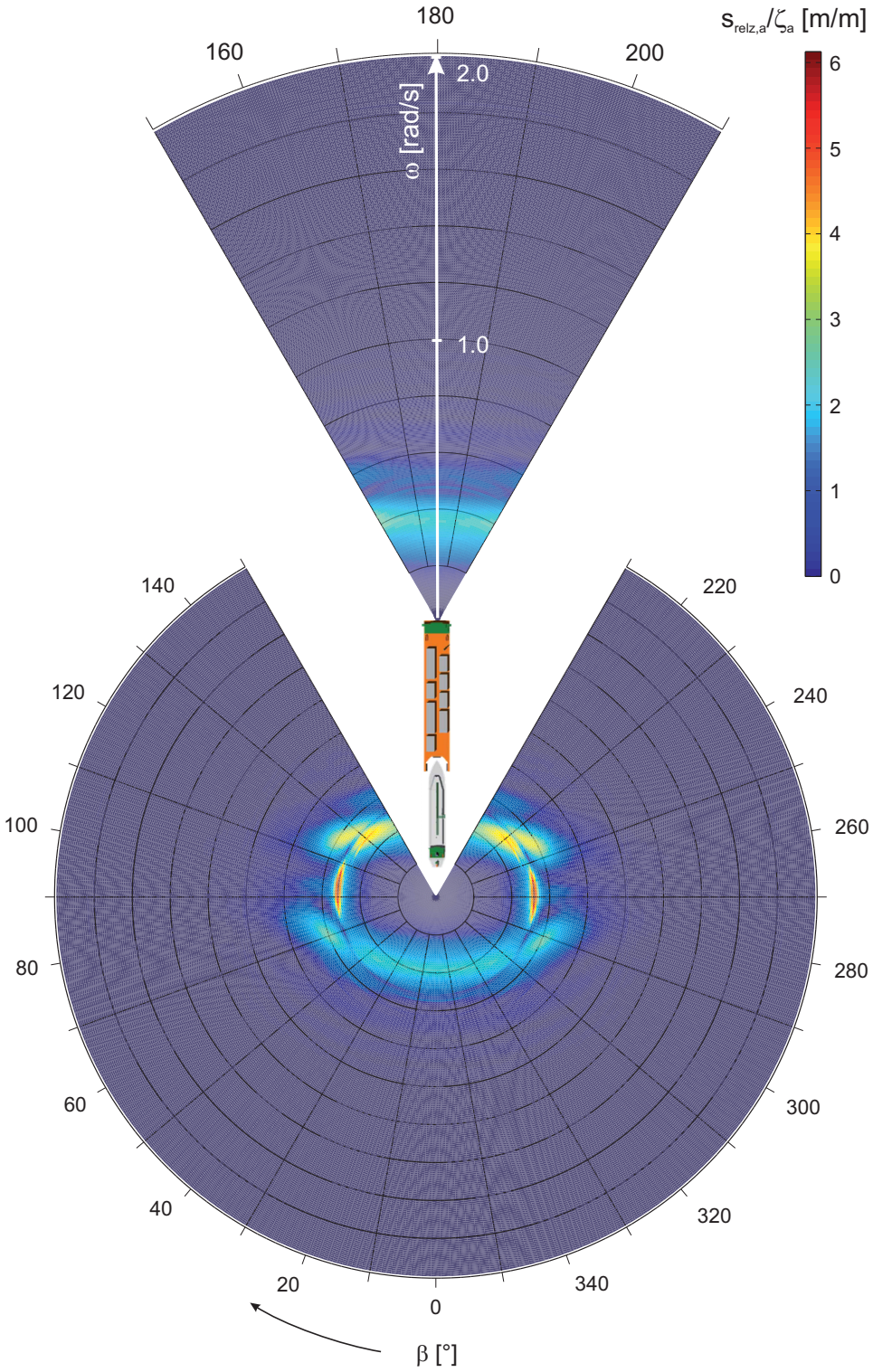


Figure 3.33: *Relative z-motion amplitudes of the coupling points of the transfer pipe resulting from the worst case analysis with respect to the filling height during the transfer period. The relevant incident wave angles lie within the weather vaning range ($150° \leq \beta \leq 210°$).*

the range of 0.4 rad/s $< \omega <$ 1.0 rad/s, each ring representing the resonant response due to the first longitudinal sloshing mode associated with the respective loading case. Maximum relative $x$-motion amplitudes of $\pm 3$ m per meter wave amplitude occur in very long waves and head seas ($\beta = 180°$).

In Fig. 3.33, the maximum relative $z$-motions with respect to the internal fluid filling height is visualized analogously to the relative $x$-motion. As previously discussed, the vertical motion features no sloshing impacts. For $\beta = 150°$ and $\omega = 0.4$ rad/s, maximum motion amplitudes of $\pm 3$ m per meter wave amplitude occur.

In the final step of the worst case analysis procedure, the maximum relative $x$- and $z$-motion amplitudes with respect to the incident wave angle in the weather vaning range are determined for each wave frequency $\omega$. This leads to a further reduction of data from the initial four-dimensional data array to a common two-dimensional RAO for the relative $x$- and $z$-direction. In order to retrace the maximum values for each frequency, Fig. 3.34 shows the RAOs for the weather vaning range with superposed white lines indicating the angular location of the maximum values. Note that due to the symmetry of the system, maximum values are visualized in the lower half of the frequency range ($150° \leq \beta \leq 180°$) exclusively. In the upper part of this figure, the origin of the relative $x$-motion worst case RAO (left) can be retraced from the polar graph representing the weather vaning range. In very long waves, i.e. $\omega < 0.2$ rad/s, maximum relative $x$-motion amplitudes occur in head seas ($\beta = 180°$), while the maximum values within the resonant sloshing frequency range (0.4 rad/s $< \omega <$ 1.0 rad/s) are located at the maximum assumed weather vaning deflections at $\beta = 150°$. The distribution for higher frequencies ($\omega > 1.0$ rad/s) appears to be rather random within an angular range of $160° < \beta < 180°$.

The origin of the relative $z$-motion worst case RAO can be retraced in the lower part of Fig. 3.34. As for the $x$-direction, the maximum motion amplitudes in long waves ($\omega < 0.2$ rad/s) occur in head seas. Since — in contrast to the longitudinal case — no resonant sloshing effects are present, maximum values for $\omega > 0.2$ rad/s are distributed randomly over the entire weather vaning range.

The worst case RAOs for the relative $x$- and relative $z$-motion constitute the basis for the classical stochastic downtime analysis (cf. section 2.4), which is conducted in the subsequent section.

### 3.5.2 Determination of the Operational Range

In the following, the operational range for offshore LNG transfer with the MPLS20 system is exemplarily determined for the *Haltenbanken* region off Norway, where the water depth is assumed to be 100 m and the sea conditions are described by the JONSWAP formulation according to Eq. (2.30). At first, a series of 150 JONSWAP spectra of unit wave height ($H_s = 1$ m)

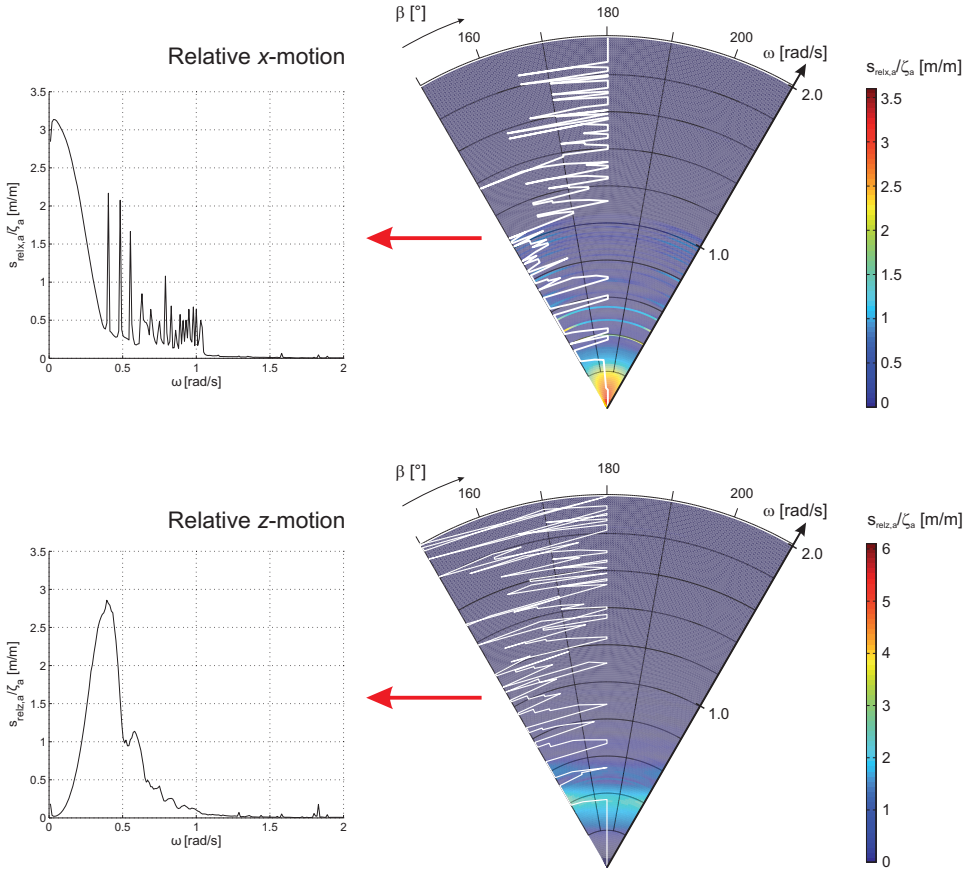


Figure 3.34: *Relative $x$- (top) and $z$-motion amplitudes (bottom) of the coupling points of the transfer pipe resulting from the worst case analysis with respect to the filling height and the incident wave angle within the weather vaning range ($150° \leq \beta \leq 210°$) during the transfer period.*

is generated, with zero-upcrossing periods ranging from 0.1 s $\leq T_0 \leq$ 15 s. These spectra are presented in the top region of Fig. 3.35. In order to clarify the following calculation steps, the spectrum for $T_0 = 6$ s is highlighted in green and the spectrum for $T_0 = 10$ s is highlighted in red. In the next step, the squared absolute values of the worst case relative $x$- and $z$-motion amplitudes of the coupling points are multiplied by each of the 150 JONSWAP spectra (cf. Eq. (2.31)), leading to 150 response spectra for each direction of motion, $S_{relx}$ and $S_{relz}$. Again, the spectra for $T_0 = 6$ s and $T_0 = 10$ s are highlighted in Fig. 3.35. For both, the relative $x$- as well as the relative $z$-motion, it can be observed that responses related to the JONSWAP spectrum with $T_0 = 10$ s are significantly higher than for $T_0 = 6$ s. Now, the area under each of the response spectra has to be determined in

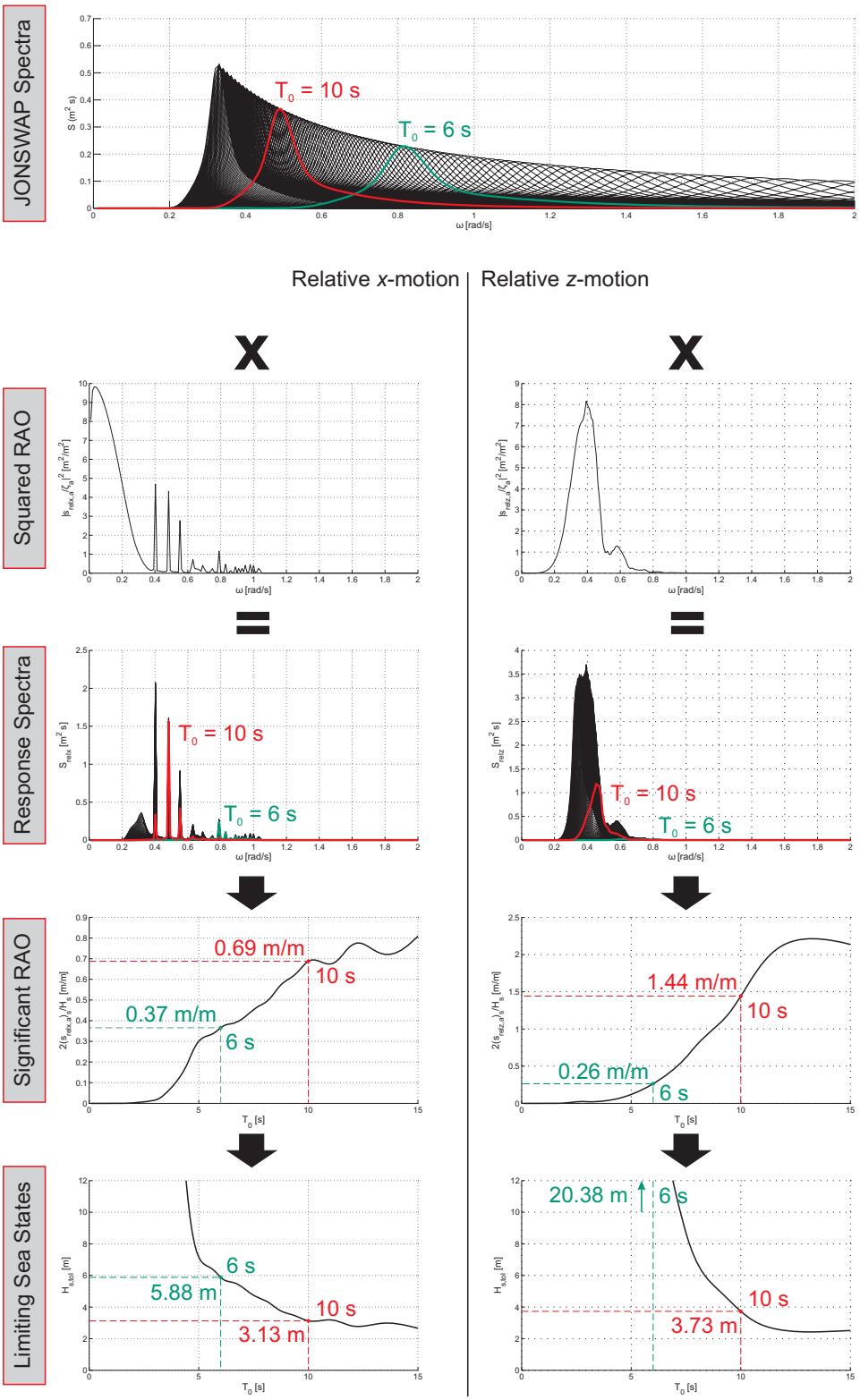


Figure 3.35: *Scheme for the determination of the tolerable sea states on the basis of 150 JONSWAP spectra (range of zero-upcrossing periods 0.1 s* $\leq T_0 \leq$ *15 s) for the worst case relative x-motion (left column) and worst case relative z-motion (right column). For exemplary illustration, results for* $T_0 = 6$ *s are highlighted in green and for* $T_0 = 10$ *s in red.*

order to obtain the significant RAOs $2(s_{relx,a})_s/H_s$ and $2(s_{relz,a})_s/H_s$ according to Eq. (2.32). After the integration over the wave frequency $\omega$, each response spectrum related to a specific zero-upcrossing period yields one significant double amplitude value, e.g. 0.37 m/m for $T_0 = 6$ s and 0.69 m/m for $T_0 = 10$ s for the relative $x$-motion and 0.26 m/m for $T_0 = 6$ s and 1.44 m/m for $T_0 = 10$ s for the relative $z$-motion. The reciprocal value of the significant RAOs in combination with tolerable significant relative motions of the pipe coupling points ($\pm 1.08$ m in $x$-direction and $\pm 2.69$ m in $z$-direction) yields the upper limit of tolerable sea states for offshore LNG transfer in the given configuration (cf. Eq. (2.33)). To comply with the maximum tolerable relative $x$-motion, a sea state with $T_0 = 6$ s must not be higher than $H_s = 5.88$ m, in seas with $T_0 = 10$ s significant wave heights have to be below $H_s = 3.13$ m in order to ensure safe operations. Limiting values for the same zero-upcrossing periods with respect to the maximum tolerable $z$-motion are higher: For seas with $T_0 = 6$ s wave heights have to be below $H_s = 20.38$ m (since this value is far above any measurements in this region, LNG transfer operations are generally safe from a stochastic point of view), for $T_0 = 10$ s significant wave heights up to $H_s = 3.73$ m are tolerable.

Separate assessment of both directions of relative motion does not allow general conclusions regarding the operational range. Therefore, the limiting tolerable sea states with respect to the maximum tolerable relative $x$- and $z$-motion are combined as shown in Fig. 3.36 (left). Apart from sea states with very long waves ($T_0 > 10$ s), the resulting limiting sea states are clearly dominated by the relative $x$-motion. On the right-hand side of Fig. 3.36, the sea states where LNG offloading is feasible are highlighted in green, while infeasible sea states are highlighted in red. This result is still independent from the location (apart from the water depth) and can finally be transferred to any given wave scatter diagram, which is a table that contains data from long term measurements at a certain location. Each cell of this table

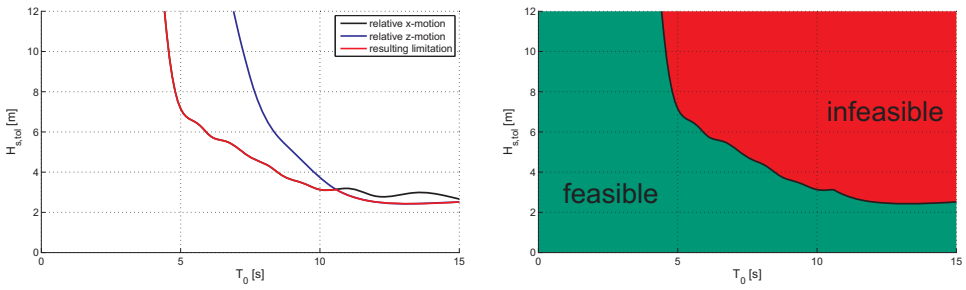


Figure 3.36: *Determination of the resulting limiting parameter combining the maximum tolerable relative $x$- and $z$-motions (left) and definition of sea states where LNG transfer is feasible or infeasible (right).*

contains the frequency of occurrence for a certain combination of significant wave height $H_s$ and usually either the peak period $T_p$ or the zero-upcrossing period $T_0$ within a specific observation period, which usually covers at least one year. The resulting limiting sea states for LNG offloading with the MPLS20 system are exemplarily transferred to a wave scatter diagram for the *Haltenbanken* region off Norway (cf. Mathisen and Bitner-Gregerson (1990)). This table contains a total of 16,834 sea state occurrences and for

| | | Zero-Upcrossing-Period $T_0$ [s] | | | | | | | | | | | | Sum |
|---|---|---|---|---|---|---|---|---|---|---|---|---|---|---|
| | | 0-4 | 4-5 | 5-6 | 6-7 | 7-8 | 8-9 | 9-10 | 10-11 | 11-12 | 12-13 | 13-14 | 14-15 | |
| significant wave height $H_s$ [m] | 11,5-12,0 | 0 | 0 | 0 | 0 | 0 | 0 | 0 | 0,006 | 0 | 0 | 0 | 0 | 0,006 |
| | 11,0-11,5 | 0 | 0 | 0 | 0 | 0 | 0 | 0 | 0,006 | 0 | 0 | 0 | 0 | 0,006 |
| | 10,5-11,0 | 0 | 0 | 0 | 0 | 0 | 0 | 0 | 0,012 | 0 | 0 | 0 | 0 | 0,012 |
| | 10,0-10,5 | 0 | 0 | 0 | 0 | 0 | 0 | 0 | 0,006 | 0 | 0 | 0 | 0 | 0,006 |
| | 9,5-10,0 | 0 | 0 | 0 | 0 | 0 | 0 | 0,012 | 0,018 | 0,006 | 0 | 0 | 0 | 0,036 |
| | 9,0-9,5 | 0 | 0 | 0 | 0 | 0 | 0 | 0,06 | 0,024 | 0,006 | 0 | 0 | 0 | 0,090 |
| | 8,5-9,0 | 0 | 0 | 0 | 0 | 0 | 0 | 0,078 | 0,03 | 0 | 0 | 0 | 0 | 0,108 |
| | 8,0-8,5 | 0 | 0 | 0 | 0 | 0 | 0 | 0,036 | 0,132 | 0,018 | 0 | 0 | 0 | 0,185 |
| | 7,5-8,0 | 0 | 0 | 0 | 0 | 0 | 0 | 0,114 | 0,161 | 0,03 | 0 | 0 | 0 | 0,305 |
| | 7,0-7,5 | 0 | 0 | 0 | 0 | 0,018 | 0,179 | 0,084 | 0,006 | 0 | 0 | 0 | 0 | 0,287 |
| | 6,5-7,0 | 0 | 0 | 0 | 0 | 0,048 | 0,365 | 0,096 | 0,006 | 0 | 0 | 0 | 0 | 0,514 |
| | 6,0-6,5 | 0 | 0 | 0 | 0 | 0,185 | 0,544 | 0,042 | 0,018 | 0 | 0 | 0 | 0 | 0,790 |
| | 5,5-6,0 | 0 | 0 | 0 | 0 | 0,7 | 0,544 | 0,084 | 0,006 | 0 | 0 | 0 | 0 | 1,334 |
| | 5,0-5,5 | 0 | 0 | 0 | 0,042 | 1,16 | 0,449 | 0,102 | 0 | 0 | 0 | 0 | 0 | 1,752 |
| | 4,5-5,0 | 0 | 0 | 0 | 0,473 | 1,531 | 0,514 | 0,096 | 0,006 | 0 | 0 | 0 | 0 | 2,620 |
| | 4,0-4,5 | 0 | 0 | 0,006 | 1,406 | 1,621 | 0,449 | 0,167 | 0,012 | 0 | 0 | 0 | 0 | 3,661 |
| | 3,5-4,0 | 0 | 0 | 0,197 | 2,434 | 1,573 | 0,604 | 0,054 | 0 | 0 | 0 | 0 | 0 | 4,863 |
| | 3,0-3,5 | 0 | 0 | 1,118 | 3,074 | 1,752 | 0,467 | 0,096 | 0 | 0 | 0 | 0 | 0 | 6,508 |
| | 2,5-3,0 | 0 | 0,096 | 3,828 | 3,84 | 1,818 | 0,58 | 0,09 | 0,012 | 0 | 0 | 0 | 0 | 10,264 |
| | 2,0-2,5 | 0 | 1,854 | 6,041 | 4,45 | 1,693 | 0,431 | 0,108 | 0,018 | 0 | 0 | 0 | 0 | 14,594 |
| | 1,5-2,0 | 0,496 | 6,884 | 6,579 | 2,991 | 1,184 | 0,233 | 0,042 | 0 | 0 | 0 | 0 | 0 | 18,410 |
| | 1,0-1,5 | 4,336 | 9,57 | 5,222 | 2,183 | 0,419 | 0,042 | 0,018 | 0 | 0 | 0 | 0 | 0 | 21,790 |
| | 0,5-1,0 | 4,36 | 4,516 | 1,962 | 0,586 | 0,114 | 0,018 | 0 | 0 | 0 | 0 | 0 | 0 | 11,556 |
| | 0,0-0,5 | 0,132 | 0,108 | 0,054 | 0,012 | 0 | 0 | 0 | 0 | 0 | 0 | 0 | 0 | 0,305 |
| Sum | | 9,325 | 23,028 | 25,007 | 21,491 | 13,817 | 5,419 | 1,376 | 0,478 | 0,060 | 0,000 | 0,000 | 0,000 | 100 |

annual downtime:

10,6% or 39 days

Figure 3.37: *Exemplary calculation of the annual downtime for LNG transfer with the MPLS20 system at the Haltenbanken region off Norway*

each sea state, the frequency of occurrence is given in percent of the total number of occurrences within the observation period (see Fig. 3.37). Again, cells highlighted in green indicate that the offloading operation is feasible for the respective combination of significant wave height and zero-upcrossing period, while it is infeasible for all combinations that are highlighted in green. By summing up all feasible sea states, the annual operational range is determined. For the investigated case at *Haltenbanken* offshore LNG transfer with the MPLS20 system is possible at 89.4% or 326 days per year, or in other words: 39 days a year, it is not safe to conduct the offloading operation at this location (downtime 10.6%).

## 3.6 Excursion I: Exemplary Variations

The previous investigations are exclusively related to the MPLS20 offshore LNG transfer system, i.e. fixed design and operation parameters. In order to widen the basis of investigations, an alternative tank type as well as the side-by-side loading configuration is exemplarily analyzed in the following subsections. Another important issue that should be incorporated in the design of FLNG systems is the mooring of the FLNG terminal. Therefore, in section 3.7 the turret-moored FLNG of the MPLS20 system is analyzed by applying the classical approach.

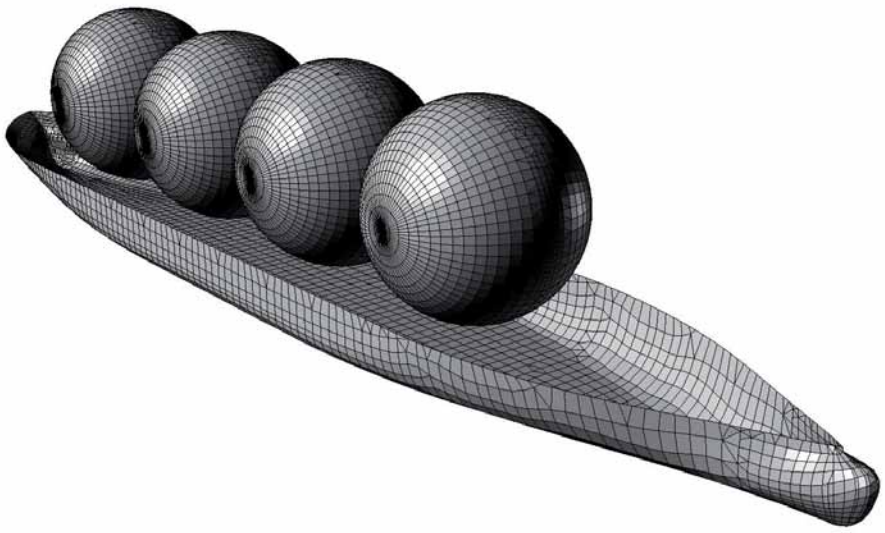

Figure 3.38: *Discretization of the LNGC with spherical MOSS type tanks*

### Tank Type Variation

Apart from prismatic tanks (such as the membrane types GT96 and TGZ Mark III of the French companies *Gaz Transport & Technigaz*), many LNGCs are equipped with spherical tanks (or 'MOSS' tanks — developed by the Norwegian company *Moss Maritime*, cf. section 1.4). The advantage of this type of tank is its self-supporting capability, but the drawbacks are higher fabrication costs compared to equivolumetric membrane type tanks as well as the less efficient utilization of the LNGC hull shape and thus more void space between cargo tanks and ballast tanks. With the successfully validated potential theory approach, the LNGC's motion characteristics are now exemplarily analyzed with four spherical tanks ($V_T$ = 33,470 m$^3$, diameter $D_T$ = 40 m) as illustrated in Fig. 3.38. Comparing the surge and roll motions of the LNGC hull described in Tabs. 1.2 and 1.3 equipped with equivolumetric prismatic and spherical tanks (equivolumetric filling 9,800 m$^3$) reveals differences in the tank resonance behavior. The surge motion RAO peak related to longitudinal tank sloshing (see Fig. 3.39, left) is significantly shifted towards higher frequencies and also lower in magnitude as compared to the resonance peak for prismatic tanks. A similar tendency can be observed for the roll motion RAO (see Fig. 3.39, right), where the low-frequency hull resonance peak appears at the same wave frequency for both cases, while the high-frequency transverse tank sloshing peak is shifted and decreased in magnitude.

Although further studies are necessary to draw general conclusions, this exemplary analysis already suggests the spherical tank's advantages with respect to the interaction of liquid sloshing and ship motions.

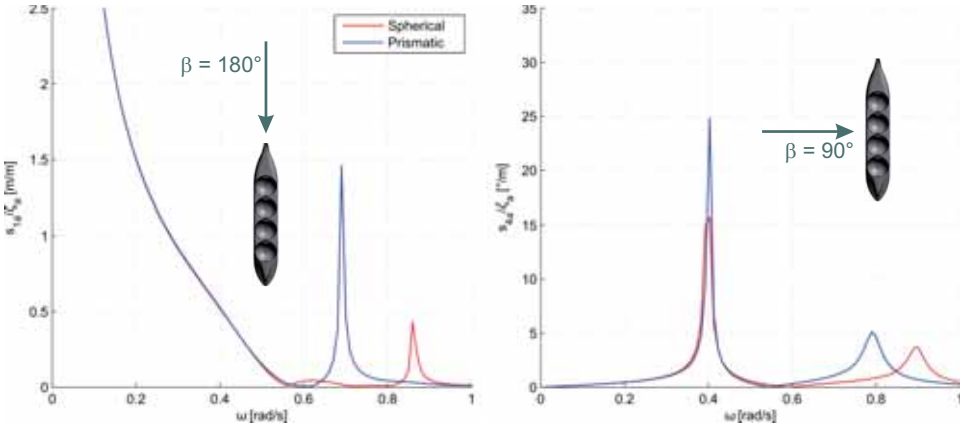


Figure 3.39: *Comparison of the LNGC's surge (β = 180°, left) and roll motion (β = 90°, right) RAOs for prismatic and spherical tanks of equivolumetric filling (9,800 m$^3$)*

### Side-By-Side Configuration

The majority of the planned offshore LNG transfer systems are designed for side-by-side configuration loading procedures (cf. section 1.2), although these concepts are limited to significant waves heights of $H_s = 1.5$ m in case of rigid loading arms, whereas tandem offloading is feasible in sea states up to $H_s = 5.5$ m. Due to manufacturing restrictions, today the maximum fender size sets the distance between FLNG terminal and LNGC to 4 m. Nevertheless, for exemplary numerical analyses, a gap width of 10 m between the two hulls is chosen. The coupling points for the transfer pipes are located at the side of the vessels' decks at the center of gravity in $x$-direction. The obvious advantage of this arrangement becomes clear from Fig. 3.40. Due to the very low influence of the pitch motion at this position, the magnitudes of the relative motions in the vertical direction are significantly decreased. The drawback of this arrangement is an increase of relative rotatory motions resulting in significant torsion on the cryogenic pipes.

For two floating bodies in side-by-side configuration, resonant wave motions inside the gap between the side walls of the two vessels have to be taken into account (cf. Eatock Taylor et al. (2010), Bunnik et al. (2009) and Pauw et al. (2007)). The assessment of this effect is crucial for the design of the mooring arrangement between the two vessels. In Fig. 3.41 (top), the relative surface elevation between FLNG terminal and LNGC (at the loca-

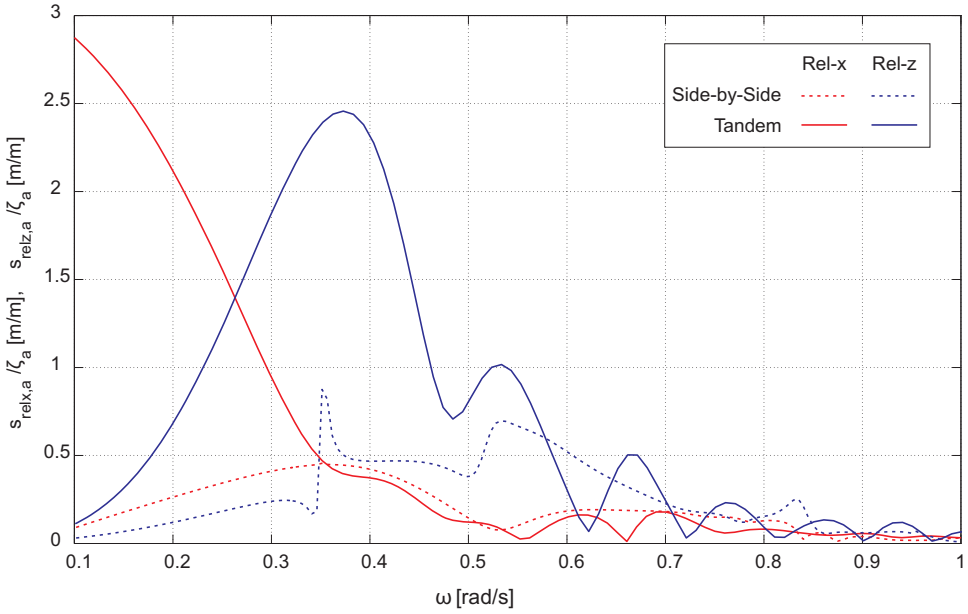


Figure 3.40: *Relative motions between the coupling points of the LNG transfer pipe for side-by-side and tandem configuration*

tion indicated by the red line in Fig. 3.41, bottom) is shown for a gap width of 10 m. In the frequency range $\omega < 0.6$ rad/s, the wave elevation in the gap is slightly lower than the surrounding sea. For 0.7 rad/s $< \omega <$ 0.85 rad/s, strong amplifications occur, leading to wave amplitudes more than 3.5 higher compared to the incident wave amplitudes. At $\omega = 0.8$ rad/s, the surface elevation is calculated numerically for different locations and time steps along the length of the gap. As illustrated in Fig. 3.41 (bottom), the wave gauge position meets the antinode of the central standing wave. A few meters to the left or right, or at the position of a node, the RAO would be completely different. Therefore, the wave field forming inside the gap has to be analyzed in detail with respect to the location, preferably in time domain as frequency domain analyses alone are not sufficient.

A Side-by-side offloading concept feasible to operate in wave significant wave heights up to $H_s = 2.5$ m was investigated in the framework of the European joint research project GIFT (Gas Floating Import Terminal), where a

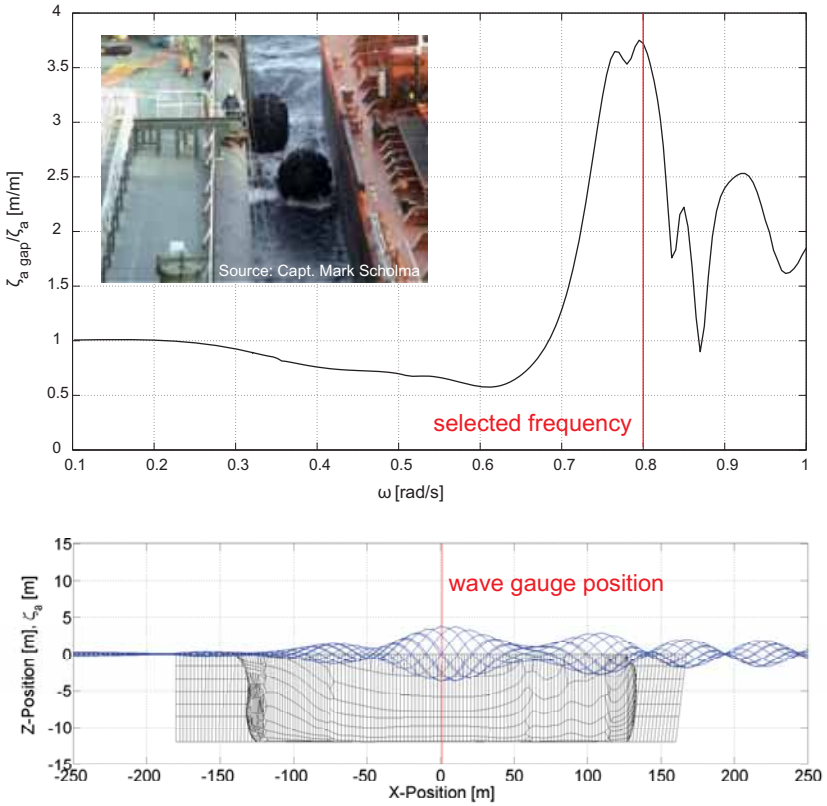


Figure 3.41: *Surface elevation in the gap (10 m) between FLNG terminal and LNGC ($\beta = 180°$, top), formation of a standing resonant wave in the gap at $\omega = 0.8$ rad/s (bottom)*

turret-moored import terminal was designed and optimized (cf. Boulougouris and Papanikolaou (2008)). As described by Claes et al. (2007), thrusters actively turn the FLNG terminal to experience oblique incident waves and create a calm lee side area which enables tug operations and mooring of the LNGC. During LNG transfer, the FLNG terminal is weather vaning freely.

In the current joint research project SOTLL (Sideways Offshore Transfer of LNG and LPG), side-by-side offloading is investigated by model test series as well as numerical calculations. Variable parameters of the system configuration include the relative position of the vessels in transverse (gap width) and longitudinal direction (position of transfer pipes) as well as the dimension of the involved vessels.

## 3.7 Excursion II: Mooring Analysis

The comprehensive investigation of an offshore LNG loading scenario where a LNGC is moored to FLNG terminal has to include the influence of the terminal's mooring on the motion characteristics as well. Since a detailed mooring analysis reaches beyond the scope of this work, a brief exemplary summary (see also Clauss et al. (2011)) of the classical approach with the turret-moored FLNG terminal as presented in Tab. 1.2 and Fig. 3.1 (top) is given in this section.

As illustrated in Fig. 3.42, the turret mooring system of the FLNG terminal consists of 12 identical mooring lines assembled in four groups of three lines, each of which is made of four segments with the characteristics given in Tab. 3.2. The center lines of the groups are arranged at an angular distance

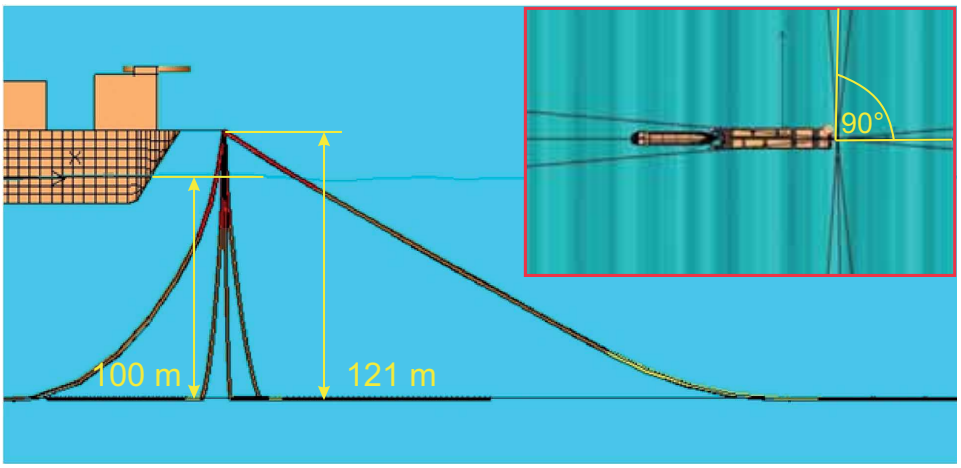


Figure 3.42: *Schematic illustration of the turret mooring design for the FLNG terminal*

Table 3.2: *Characteristics of the mooring line segments (numbered from bottom to top)*

| | Seg.1 | Seg.2 | Seg.3 | Seg.4 |
|---|---|---|---|---|
| Composition | Chain | Chain | Wire | Chain |
| Length, $L_S$ [m] | 900 | 100 | 150 | 50 |
| Diameter, $D_{eq}$ [m] | 0.184 | 0.25 | 0.087 | 0.13 |
| Mass in air, $m_S$ [kg/m] | 370 | 686 | 33.4 | 185 |
| Add. mass, $a_S$ [kg/m] | 27.27 | 50.3 | 6.1 | 13.6 |
| Sub. weight, $w$ [N/m] | 3157.8 | 5854.8 | 267.8 | 1579 |
| Elasticity, $EA$ [N] | 5.58E9 | 10.33E9 | 1.01E9 | 2.79E9 |

of 90° and the angular distance between each line within a group is 15°. The turret is located 192.5 m from the terminal's center of gravity in $x$-direction in the center plane ($y = 0$). The water depth is 100 m, whereas the distance of the fairleads to the sea bed is assumed to be 121 m (see Fig. 3.42).

The first step of the mooring analysis is the investigation of the behavior of a single line. The mooring analysis, that is presented in the following is concerned with the FLNG terminal alone, i.e. without having the LNGC connected to it. In Fig. 3.43, the static configuration of a single mooring line in the two-dimensional plane under various pretension forces in the range of

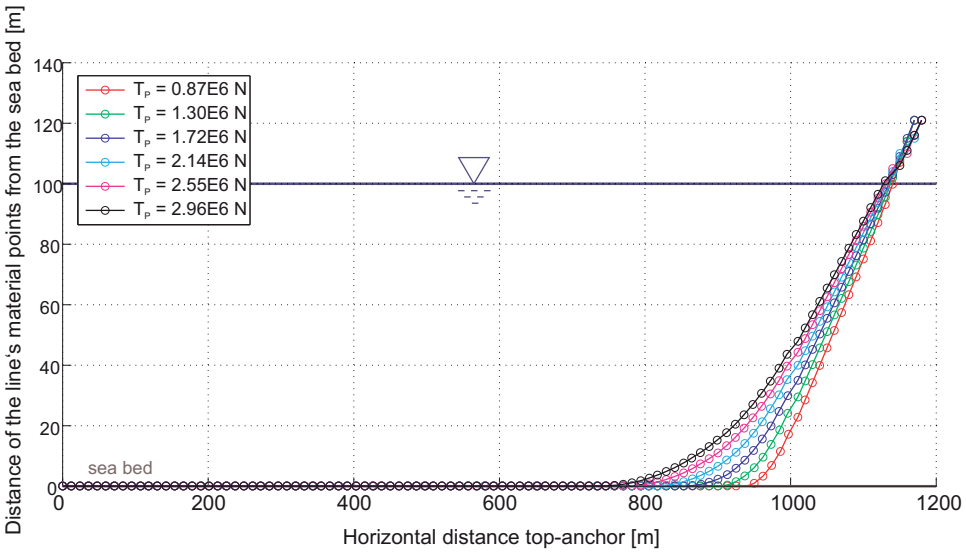


Figure 3.43: *Static configuration of a single line in the two-dimensional plane for various pretension forces $T_P$ applied at the fairlead*

0.87E06 N $\leq T_P \leq$ 2.96E06 N — applied at the fairlead — is presented. For three different pretension levels $T_P$, various external loads $F_{ex,H}$ are applied on the 12 turret lines. The resulting horizontal excursions of the vessel in $x$-direction are shown in Fig. 3.44 (left).

The stiffness of the mooring system in the horizontal plane $k_{xx}$ in dependency of the three selected pretension levels and the imposed external horizontal force is depicted in Fig. 3.44 (right). It can be observed that for a wide range of external loading, the stiffness of the mooring system remains almost constant. This range depends on the pretension level. With the determination of the mooring system stiffness, the complete system of governing equations that describe the static equilibrium of the extensible lines is solved separately for each line using the 4$^{\text{th}}$ order Runge-Kutta method for non-linear ordinary differential equations. The results are exemplarily superimposed to predict the final balancing position of the moored FLNG terminal under specified loading conditions in $x$-direction (surge drift motion) using an iteration process (see Chatjigeorgiou and Mavrakos (2003)). Furthermore, a quasi-static approach is applied for assessing the mean as well as the slowly-varying vessel motions (see Chatjigeorgiou et al. (2006)).

For the evaluation of the structure's mean excursion $\bar{x}_0^{(2)}$, the mean wave drift forces $\bar{F}_{x0}^{(2)}$ in irregular seas are required together with the mooring system stiffness, given in Fig. 3.44 (right). Wind and current effects have not been considered in this exemplary calculation. The slowly-varying vessel motions then are obtained by accounting for the restoring characteristics of the mooring system around the mean equilibrium position of the FLNG

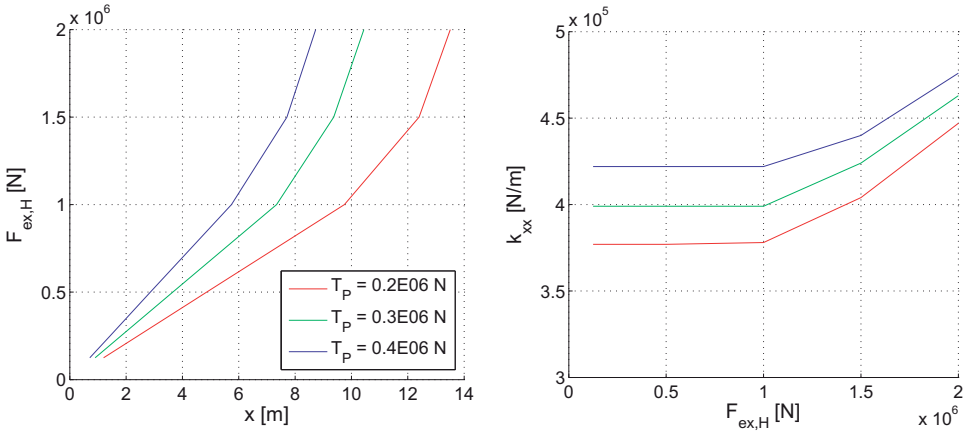


Figure 3.44: *Horizontal turret excursion versus horizontal exciting force for three pretension levels (left); mooring system stiffness coefficient in the horizontal direction depending on the pretension level and the external force (right)*

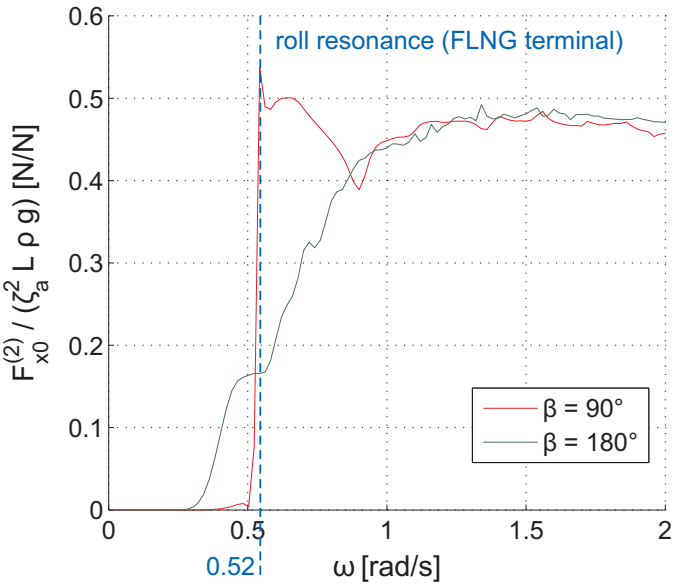


Figure 3.45: *Mean drift forces on the FLNG terminal in regular waves for incident angles $\beta = 90°$ and $\beta = 180°$*

terminal and the associated spectra of the low-frequency excitations (see Faltinsen (1990)):

$$\bar{F}_{x0}^{(2)} = 2 \int_0^\infty S(\omega) \frac{F_{x0}^{(2)}(\omega)}{\zeta_a^2} d\omega \tag{3.23}$$

A JONSWAP spectrum $S(\omega)$ with $H_s = 5.5$ m, $T_0 = 10$ s and $\gamma = 3.3$ is considered as the basis of the investigations. The mean drift forces $F_{x0}^{(2)}/\zeta_a^2$ in regular waves have been calculated using the potential theory solver WAMIT and the momentum conservation principle. The results for head seas ($\beta = 180°$) — and for comparative reasons also for beam seas ($\beta = 90°$) — are presented in Fig. 3.45. Note that the mean drift forces are normalized by the fluid density $\rho$, the gravitational acceleration $g$, the squared

Table 3.3: *Mean excursion and stiffness characteristics for the mean drift force on the FLNG terminal in head seas*

| Pretension $T_P$ [N] | Stiffness $k_{xx}$ [N/m] | Mean exc. $\bar{x}_0^{(2)}$ [m] |
|---:|---:|---:|
| 0.2E06 | 3.77E05 | 1.20 |
| 0.3E06 | 3.99E05 | 0.90 |
| 0.4E06 | 4.22E05 | 0.71 |

wave amplitude $\zeta_a^2$ and the respective characteristic length $L_i$ ($L_x = 65$ m, i.e. the breadth of the FLNG terminal, and $L_y = 400$ m, i.e. the vessel length). For these two forces and the given environmental conditions, the mean wave drift loads of $\bar{F}_{x0}^{(2)} = 1.2535\text{E}05$ N for head seas, and exemplarily also $\bar{F}_{y0}^{(2)} = 1.5216\text{E}06$ N for beam seas, are determined.

For the following calculations, head seas ($\beta = 180°$) are considered. The mean excursions for the mean drift force, defined by $\bar{x}_0^{(2)} = F_0^{(2)}/k_{xx}$ with the associated stiffness coefficients $k_{xx}$ for the three pretension levels are given in Tab. 3.3.

The slowly-varying response spectrum of the terminal motions in irregular seas is given by the relation (Faltinsen (1990)):

$$S_{\tilde{x}}(\mu) = S_F(\mu) \frac{1}{k_{xx}^2 \left\{ \left[ 1 - \left( \frac{\mu}{\mu_{0x}} \right)^2 \right]^2 + \left[ 2\, b\, \frac{\mu}{\mu_{0x}} \right]^2 \right\}} \tag{3.24}$$

where $S_F(\mu)$ is the spectrum of the slowly-varying second-order wave forces exerted on the structure, which by assuming Newman's approximation (Newman (1974)) is given by Pinkster (1975):

$$S_F(\mu) = 8 \int_0^\infty S_\zeta(\omega)\, S_\zeta(\omega + \mu)\, \frac{F_{x0}^{(2)}(\omega + \mu/2)}{\zeta_a^2}\, d\omega \tag{3.25}$$

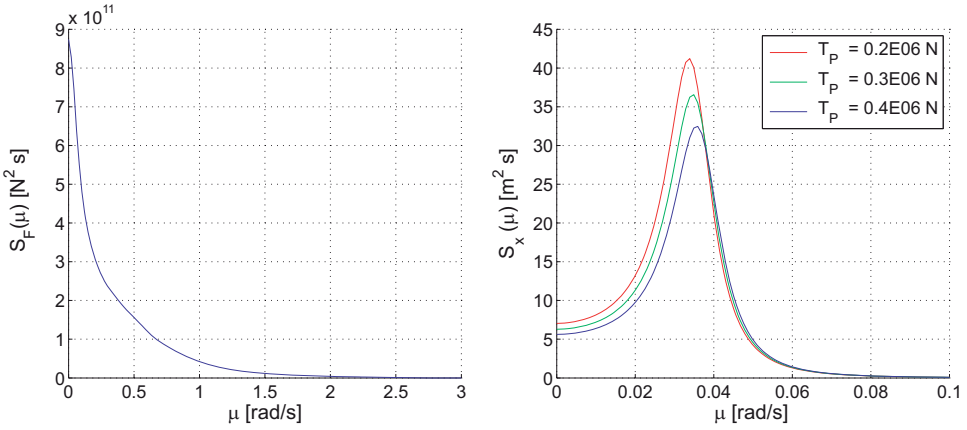


Figure 3.46: *Spectrum of the slowly-varying wave drift forces on the FLNG terminal ($\beta = 180°$, left) and spectrum of the slowly-varying surge drift motion of the FLNG terminal ($\beta = 180°$, right)*

$F_{x0}^{(2)}(\omega + \mu/2)$ is the mean drift force on the structure in $x$-direction, $\mu_{0x} = \sqrt{k_{xx}/\left(m + a_{11}\right)}$ is the natural frequency of the horizontal motion component due to the presence of the mooring system, with $a_{11}$ being the added mass of the FLNG terminal in $x$-direction, and $\delta$ the ratio of total to critical damping defined by the relation $b_{m,11} = 2\,\delta\,\mu_{0x}\,(m + a_{11})$. Its calculation presumes the evaluation of the three main damping components besides radiation damping: Damping related to the friction on the wetted part of the structure, to the second-order wave drift and mooring-induced damping. In the present analysis, the damping ratio is assumed to be $\delta = 0.2$.

Fig. 3.46 (left) shows the spectrum of the slow-drift excitation on the FLNG terminal in head seas ($\beta = 180°$), evaluated according to Eq. (3.25), while in Fig. 3.46 (right), the corresponding spectra for the slow-drift surge responses are given with respect to the three pretension levels. With the root mean square of these spectra

$$\tilde{x}_{RMS} = \sqrt{\int_0^\infty S_{\tilde{x}}(\mu) d\mu} \tag{3.26}$$

the significant $\tilde{x}_s = 2\,\tilde{x}_{RMS}$ and maximum $\tilde{x}_{max} = 1.86\ \tilde{x}_s$ expected slow surge drift amplitudes can be calculated by spectral analysis methods. The results of this analysis are shown in Tab. 3.4, in dependency of the pretension level in the mooring system.

Depending on the pretension in the lines, significant surge drift amplitudes of the turret-moored FLNG terminal are within the range of 1.72 m to 1.88 m, with associated maximum surge drift amplitudes of 3.19 m to 3.49 m.

Table 3.4: *Significant and maximum slow-drift excursions of the terminal in surge direction*

| Pretension $T_P$ [N] | Sign. exc. $\tilde{x}_s$ [m] | Max. exc. $\tilde{x}_{max}$ [m] |
|---:|---:|---:|
| 0.2E06 | 1.88 | 3.49 |
| 0.3E06 | 1.79 | 3.34 |
| 0.4E06 | 1.72 | 3.19 |

# Chapter 4

# Conclusions & Consequences

The assessment of offshore LNG transfer procedures requires profound knowledge on complex hydrodynamic issues such as multi-body interaction and bidirectional coupling effects of internal fluid motions and vessel responses in waves. As described in section 1.4, published methods are capable to capture individual aspects of these effects, but a closed-form solution of the entire process is not available so far. For multi-body analyses, reliable and validated methods such as potential theory or multiple-scattering theory for axisymmetric bodies are available. Known model tests and numerical studies were conducted under idealized conditions such as simplified geometries and pure beam seas. Although — implying certain assumptions — those simplified approaches were capable to reproduce coupling effects of internal fluid motions and the seakeeping behavior of a LNGC, two important effects have not been discovered and comprehensively studied so far:

- The deviation between the tank's first natural mode and the sloshing related response peak of the respective LNGC motions
- the occurrence of asymmetric internal fluid motions and vessel responses in pure beam seas

→ *without the knowledge on the complex chain of cause and effect in coupling of sloshing and ship motions, results from model tests and numerical analyses cannot be interpreted and consequently not extrapolated meaningfully to full scale offshore operations.*

→ *For the fist time, a comprehensive holistic analysis procedure for offshore LNG offloading operations including multi-body interactions and sloshing effects is provided in this thesis. The proposed four-dimensional worst-case analysis method takes into account varying tank filling heights, incident wave angles and sea state conditions for each degree of freedom. This allows straight-forward determination of operational ranges for offshore LNG transfer concepts.*

Apart from structural issues, linear theory proves to be the most efficient and elegant approach to assess the influence of sloshing on the seakeeping behavior of LNGCs and the consequences for the operational range of offshore LNG transfer systems.

In the following, the key findings and consequences resulting from the presented investigations are compiled:

- **Initial Stability**
  The presence of free fluid surfaces reduces the initial stability of a ship in terms of the metacentric height. The magnitude of reduction is related to area of the free surface, which in case of chamfered prismatic tanks depends on the filling height (cf. section 3.1).

- **Sloshing**
  Partially filled internal tanks contribute negative heave, roll and pitch restoring coefficients to the equation of motion — i.e. they reduce the effective waterplane area of the vessel. The added mass coefficients for the vertical motions heave, roll and pitch also require special attention because a 'fictitious hydrostatic contribution' has to be considered (cf. Eq. (2.26)).

  In section 3.2, detached rectangular and prismatic tanks are analyzed analytically and numerically. For the rectangular tank, analytically determined odd transverse and longitudinal resonant modes agree excellently with potential theory results (since they are not coupled with the ship motions, even sloshing modes cannot be reproduced by linear potential theory). The same applies for the prismatic tank. Except for the lower and upper chamfer regions, analytical and numerical resonance frequencies agree very well. The strong deviations in the top chamfer region, i.e. filling heights greater than 70%, is owed to the fact that the narrowing of the tank cross-section is not covered by the analytical approach. Here, the numerical results appear more trustworthy, while in the lower chamfer region (filling height less than 20%, which is covered by the analytical approach), only slight deviations are observable but results from both approaches should be considered with care in this region, since the effect of the tank bottom falling dry at low filling heights and resonant liquid motions (hydraulic jumps) is neglected. In general, the natural mode of a tank depends on the filling height as well as the characteristic length, e.g. the breadth of the tank. The related frequency increases with increasing filling height (following a parabola shaped curve) and decreasing length and vice versa.

- **Coupling of Sloshing and Ship Motions**
  For 30% fresh water filling in all four prismatic tanks, the numerical model is successfully validated by model test data in section 3.3. Rigid

body motions as well as internal fluid motions at selected wave gauge positions inside the tanks agree excellently, i.e. the linear potential theory approach captures all relevant effects to a sufficient extend.

Fluid motions in cargo tanks onboard a LNGC influence the seakeeping behavior in all degrees of freedom, except for the heave and the pitch motion, which remain largely unaltered. The roll motion RAO reveals the most dramatic impact: instead of one peak at the rigid body roll resonance frequency for solid filling (or ballast), the RAO for partially filled tanks features an additional secondary peak which is obviously sloshing-related. However, this peak is not located at the first transverse natural mode of the tank, but is shifted by $\Delta\omega$ towards higher frequencies. The internal surface elevations in beam seas yield another surprising phenomenon: The respective RAOs do not exclusively feature the two peaks as expected from the roll motion, but an additional third peak of intermediate frequency. Also, the absolute values of the surface elevation vary from tank to tank.

In-depth studies show that the peak shift $\Delta\omega$ is caused by the complex combination of the total masses due to motion coupling of sway, roll and yaw. The magnitude of $\Delta\omega$ depends on the the ratio of solid hull mass to added mass. The smaller the solid body mass, the larger the frequency deviation and vice versa. The same effect has to be taken into account when seakeeping with internal liquids of different density is compared.

→ *Results obtained by classical fresh water model tests cannot be directly transferred to full scale operations with LNG since $\Delta\omega$ for LNG is always smaller as for fresh water filling, implying identical vessels at constant draft.*

The heterogenous internal fluid responses as well as the occurrence of the third peak in the tank surface elevation RAOs are attributed to system asymmetries. In pure beam seas ($\beta = 90°$), the asymmetric bow-stern geometry of the submerged part of the LNGC hull as well as the eccentric lengthwise position of the four prismatic tanks lead to resonant longitudinal sloshing and responses in surge, pitch and yaw — perpendicular to the direction of excitation.

→ *The majority of studies published so far consider idealized 'two-dimensional' sloshing and do not mention asymmetric effects. But for offshore operations involving hazardous cargo and two vessels in close proximity, these simplifications pose a considerable risk. In order to ensure safety, fully three-dimensional studies and the awareness of asymmetric responses are inevitable prerequisites.*

- **Multi-Body Analysis**
  The exemplary analysis of the MPLS20 offloading procedure in sec-

tion 3.4 comprises four different phases, where the distance between LNGC and FLNG terminal is reduced from 100 m to 50 m and finally to 10 m, which is the transfer distance for the tandem configuration. During the approach phase, the seakeeping behavior of the FLNG terminal is not influenced by the presence of the LNGC, which is located downstream. The LNGC heave and pitch motions on the other hand are clearly decreased by the presence of the FLNG terminal, which is positioned upstream and shadows the carrier from the incident waves to some extend. For the transfer phase, the relative motion amplitudes of the coupling points of the cryogenic transfer pipe are calculated for a range of incident wave angles $0° < \beta < 360°$ and LNG filling heights are gradually increased from 5% to 95% in 19 steps, resulting in a four-dimensional data array.

- **Stochastic Analysis**
  Prior to the classical spectral analysis, the worst-case scenario to be expected for the offloading operation is determined by identifying the maximum relative motion amplitudes with respect to the tank filling height and the incident wave angle within the weather vaning range of the FLNG terminal ($150° \leq \beta \leq 210°$) for each wave frequency $\omega$ (cf. section 3.5). The resulting worst-case RAOs for each direction of relative motion are subsequently subjected to the stochastic analysis procedure and the operational range of the MPLS20 system is exemplarily determined for the *Haltenbanken* region off Norway. With maximum tolerable relative $x$-motion amplitudes of $\pm 2$ m and maximum tolerable relative motion amplitudes of $\pm 5$ m in $z$-direction, the annual downtime becomes 10.6% or 39 days. In other words, this concepts allows LNG transfer at 89.4% of the time or 326 days of the year in the exposed *Haltenbanken* region.

  → *With given system-specific maximum tolerable parameters such as relative motions, velocities, accelerations and first-order forces, the proposed four-dimensional worst-case analysis procedure allows straightforward determination of operational ranges for offshore LNG transfer concepts. All relevant hydrodynamic aspects are covered, ensuring safe operations at exposed locations.*

# Bibliography


Abramson, H. N. (1966). The Dynamic Behavior of Liquids in a Moving Container. Technical Report SP-106, NASA.

Boulougouris, E. K. and Papanikolaou, A. D. (2008). Multi-Objective Optimisation of a Floating LNG Terminal. *Journal of Ocean Engineering*, 35:787–811.

Bunnik, T., Pauw, W. H., and Voogt, A. (2009). Hydrodynamic Analysis for Side-by-Side Offloading. In *Proceedings of the 19$^{th}$ International Offshore and Polar Engineering Conference*, Osaka, Japan.

Bunnik, T. and Veldman, A. (2010). Modelling the Effect of Sloshing on Ship Motions. In *Proceedings of the 29$^{th}$ International Conference on Ocean, Offshore and Arctic Engineering*, Shanghai, China.

Chakrabarti, S. K. (1999). Response of Multiple Structures Including Interaction. In *Proceedings of the 3$^{rd}$ International Workshop on Very Large Floating Structures*, Honolulu, USA.

Chatjigeorgiou, I. K. and Mavrakos, S. A. (2003). Higher Order Restoring Forces for the Design of Multi-Leg Mooring Arrangements. In *Proceedings of the 8$^{th}$ International Marine Design Conference*, volume II, pages 343–352, Athens, Greece.

Chatjigeorgiou, I. K., Thanos, I., Bourma, P., Mazarakos, T., and Mavrakos, S. A. (2006). Mooring System and Motion Response Analysis of a Gas Import Floating Terminal in Operating and Survival Conditions. In *Proceedings of the 25$^{th}$ International Conference on Offshore Mechanics and Arctic Engineering*, Hamburg, Germany.

Chen, X.-B. (2005). Hydrodynamic Analysis for Offshore LNG Terminals. In *Proceedings of the 2$^{nd}$ Workshop on Applied Offshore Hydrodynamics*, Rio de Janeiro, Brazil.

Chen, X.-B., Rezende, F., Malenica, Š., and Fournier, J. R. (2007). Advanced Hydrodynamic Analysis of LNG Terminals. In *Proceedings of the*

*10th International Symposium on Practical Design of Ships and Other Floating Structures*, Houston, USA.

Claes, L., Messager, J.-C., Vaché, M., and Pépin-Lehalleur, J. (2007). GIFT (Gas Import Floating Terminal): A new Concept of Floating LNG Terminal. In *Proceedings of the Offshore Technology Conference*, Houston, Texas, USA.

Clauss, G. and Jacobsen, K. (2004). Hydrodynamic Interaction of Multi-Body Systems in Waves. In *98. Jahrbuch der Schiffbautechnischen Gesellschaft e.V.*, pages 389–409. Springer Verlag.

Clauss, G. and Kühnlein, W. (1997). A New Tool for Seakeeping Tests — Nonlinear Transient Wave Packets. In *Proceedings of the 8th International Conference on the Behaviour of Offshore Structures*, pages 269–285, Delft, The Netherlands.

Clauss, G., Lehmann, E., and Östergaard, C. (1992). *Offshore Structures*, volume 1: Conceptual Design and Hydrodynamics. Springer Verlag London.

Clauss, G., Mavrakos, S. A., Sprenger, F., Testa, D., and Dudek, M. (2011). Hydrodynamic Considerations for FLNG Concepts. In *Proceedings of the 30th International Conference on Ocean, Offshore and Arctic Engineering*, Rotterdam, The Netherlands.

Clauss, G., Sprenger, F., Dudek, M., and Testa, D. (2012). Sloshing: From Theory To Offshore Operations. In *Proceedings of the 31st International Conference on Ocean, Offshore and Arctic Engineering*, Rio de Janeiro, Brazil.

Clauss, G., Sprenger, F., and Testa, D. (2010a). Coupling Effects between Tank Sloshing and Motions of a LNG Carrier. In *Proceedings of the 29th International Conference on Ocean, Offshore and Arctic Engineering*, Shanghai, China.

Clauss, G., Sprenger, F., and Testa, D. (2010b). Dynamics of Offshore LNG Transfer Systems in Harsh Seas. In *104. Jahrbuch der Schiffbautechnischen Gesellschaft e.V.*, Hamburg, Germany.

Clauss, G., Sprenger, F., Testa, D., Hoog, S., and Huhn, R. (2009). Motion Behaviour of a New Offshore LNG Transfer System at Harsh Operational Conditions. In *Proceedings of the 28th International Conference on Ocean, Offshore and Arctic Engineering*, Honolulu, USA.

Cook, J. W. (2006). Gulf Gateway Energy Bridge — The First Year of Operations and the Commercial and Operational Advantages of the Energy

Bridge Technology. In *Proceedings of the Offshore Technology Conference*, Houston, Texas, USA.

Det Norske Veritas (2011). *DNV RP-H103: Modelling and Analysis of Marine Operations*.

Douglas Westwood Limited (2010). The World FLNG Market Report 2011-2017.

Eatock Taylor, R., Sun, L., and Taylor, P. H. (2010). First and Second Order Analysis of Resonant Waves between Adjacent Barges. *Journal of Fluids and Structures*, 26.

Faltinsen, O. M. (1990). *Sea Loads on Ships and Offshore Structures*. Ocean Technology. Cambridge University Press.

Faltinsen, O. M. and Timokha, A. (2009). *Sloshing*. Cambridge University Press.

Frohne, C., Harten, F., Schippl, K., Steen, K. E., Haakonsen, R., Eide, J., and Høvik, J. (2008). Innovative Pipe System for Offshore LNG Transfer. In *Proceedings of the Offshore Technology Conference*, Houston, USA.

Frohne, C., Hoog, S., Huhn, R., Koch, H., Homann, J., Clauss, G., Testa, D., and Sprenger, F. (2010). Maritime Pipe Loading System 20" (MPLS20) — Entwicklung eines innovativen Offshore LNG Transfersystems für raue Umweltbedingungen. In *Tagungsband der Statustagung des Bundesministeriums für Wirtschaft und Technologie*, pages 21–35, Warnemünde, Germany. Schriftenreihe Projektträger Jülich.

Gaillarde, G., Ledoux, A., and Lynch, M. (2004). Coupling Effects between Liquefied Gas and Vessel's Motion for Partially Filled Tanks: Effect on Seakeeping. In *Proceedings of the RINA Conference on Design and Operation of Gas Carriers*, London, United Kingdom.

Gilmour, N. and Deveney, D. (2010). Floating LNG: Shell's Recent History and Current Approach. In *Proceedings of the 16$^{th}$ International Conference on Liquefied Natural Gas*, Oran, Algeria.

Graczyk, M. and Moan, T. (2009). Structural Response to Sloshing Excitation in Membrane LNG Tank. In *Proceedings of the 28$^{th}$ International Conference on Ocean, Offshore and Arctic Engineering*, Honolulu, USA.

Hoog, S., Berger, J., Myland, J., Clauss, G., Testa, D., and Sprenger, F. (2012). The Mooring Bay Concept For LNG Loading In Harsh And Ice Conditions. In *Proceedings of the 31$^{st}$ International Conference on Ocean, Offshore and Arctic Engineering*, Rio de Janeiro, Brazil.

Hoog, S., Koch, H., Huhn, R., Frohne, C., Homann, J., Clauss, G., Sprenger, F., and Testa, D. (2009a). LNG Transfer in Harsh Environments — Introduction of a New Concept. In *Proceedings of the Offshore Technology Conference*, Houston, USA.

Hoog, S., Koch, H., Huhn, R., Frohne, C., Homann, J., Clauss, G., Sprenger, F., and Testa, D. (2009b). LNG Transfer in Harsh Environments — Introduction of a New Tandem Mooring Concept. In *Proceedings of the AIChE Spring Meeting — $9^{th}$ Topical Conference on Natural Gas Utilization*, Tampa, USA.

Houmb, O. and Overik, T. (1976). Parametrization of Wave Spectra and Long Term Joint Distribution of Wave Height and Period. In *Proceedings of the $1^{st}$ Conference on Behaviour of Offshore Structures*, Trondheim, Norway.

Huijsmans, R. H. M., Tritschler, G., Gaillarde, G., and Dallinga, R. P. D. (2004). Sloshing of Partially Filled LNG Carriers. In *Proceedings of the $14^{th}$ International Offshore and Polar Engineering Conference*, Toulon, France.

Ibrahim, R. A. (2005). *Liquid Sloshing Dynamics. Theory And Applications.* Cambridge University Press.

International Energy Agency (2010). World Energy Outlook 2010.

ITTC (2011). *Numerical Estimation of Roll Damping.* Specialist Committee on Stability in Waves, $26^{\text{th}}$ edition.

Kim, B. and Shin, Y. S. (2008). Coupled Seakeeping with Liquid Sloshing in Ship Tanks. In *Proceedings of the $27^{th}$ International Conference on Ocean, Offshore and Arctic Engineering*, Estoril, Portugal.

Kim, J. W., Kim, K., Kim, P. S., and Shin, Y. S. (2006). The Effects of LNG-tank Sloshing on the Roll Responses of LNG-Carriers. In *Proceedings of the $16^{th}$ International Offshore and Polar Engineering Conference*, San Francisco, USA.

Lee, S. J., Kim, M., Lee, D. H., Kim, J. W., Shin, Y. S., and Kim, Y. H. (2005). Sloshing-Ship Motion Coupling Effect for the Sloshing Impact Load on the LNG Containment System. In *Proceedings of the $15^{th}$ International Offshore and Polar Engineering Conference*, Seoul, South Korea.

Lee, S. J., Kim, M. H., Lee, D. H., and Shin, Y. S. (2007). The Effects of Tank Sloshing on LNG Vessel Responses. In *Proceedings of the $26^{th}$ International Conference on Ocean, Offshore and Arctic Engineering*, San Diego, USA.

Lee, S. J., Kim, M. H., Shin, Y. S., and Kim, B. K. (2008). The Effects of Tank Sloshing on the Coupled Responses of LNG Vessel and Floating Terminal. In *Proceedings of the 18$^{th}$ International Offshore and Polar Engineering Conference*, Vancouver, Canada.

Malenica, Š., Zalar, M., and Chen, X.-B. (2003). Dynamic Coupling of Seakeeping and Sloshing. In *Proceedings of the 13$^{th}$ International Offshore and Polar Engineering Conference*, Honolulu, USA.

Mathisen, J. and Bitner-Gregerson, E. (1990). Joint Distributions for Significant Wave Height and Wave Zero-Upcrossing Period. *Applied Ocean Research*, 12(2):93–103.

Molin, B., Remy, F., Ledoux, A., and Ruiz, N. (2008). Effect of Roof Impacts on Coupling between Wave Response and Sloshing in Tanks of LNG Carriers. In *Proceedings of the 27$^{th}$ International Conference on Ocean, Offshore and Arctic Engineering*, Estoril, Portugal.

Molin, B., Remy, F., Rigaud, S., and de Jouette, C. (2002). LNG-FPSO's: Frequency Domain, Coupled Analysis of Support and Liquid Cargo Motions. In *Proceedings of the 10$^{th}$ Congress of the International Maritime Association of the Mediterranean*, Crete, Greece.

Newman, J. N. (1974). Second-Order Slowly Varying Forces on Vessels in Irregular Waves. In *Proceedings of the International Symposium on Dynamics of Marine Vehicles and Structures in Waves*, London, United Kingdom.

Newman, J. N. (1977). *Marine Hydrodynamics*. The MIT Press, Cambridge, USA.

Newman, J. N. (2001). Wave Effects on Multiple Bodies. In *Hydrodynamics in Ship and Ocean Engineering*, pages 3–26, RIAM Kyushu University, Japan.

Newman, J. N. (2005). Wave Effects on Vessels with Internal Tanks. In *Proceedings of the 20$^{th}$ International Workshop on Water Waves and Floating Bodies*, Longyearbyen, Norway.

Ohkusu, M. (1976). Ship Motions in Vicinity of a Structure. In *Proceedings of the 1$^{st}$ International Conference on the Behaviour of Offshore Structures*, Trondheim, Norway.

Pastoor, W., Lund, K., and Tveitnes, T. (2009). The LNG Producer - A Generic Design with Great Adaptability. In *Proceedings of the Offshore Technology Conference*, Houston, USA.

Pauw, W. H., Huijsmans, R. H., and Voogt, A. (2007). Advances in the Hydrodynamics of Side-by-side Moored Vessels. In *Proceedings of the 26$^{th}$ International Conference on Ocean, Offshore and Arctic Engineering*, San Diego, USA.

Peric, M. and Zorn, T. (2005). Simulation of Sloshing Loads on Moving Tanks. In *Proceedings of the 24$^{th}$ International Conference on Offshore Mechanics and Arctic Engineering*, Halkidiki, Greece.

Peric, M., Zorn, T., el Moctar, O., Schellin, T., and Kim, Y.-S. (2007). Simulation of Sloshing in LNG-Tanks. In *Proceedings of the 26$^{th}$ International Conference on Offshore Mechanics and Arctic Engineering*, San Diego, USA.

Pierson, W. and Moskowitz, L. (1964). A Proposed Spectral Form for Fully Developed Wind Seas Based on the Similarity of S.A. Kitagorodskii. *Journal of Geophysical Research*, 96(2).

Pinkster, J. A. (1975). Low Frequency Phenomena Associated with Vessels Moored at Sea. *Society of Petroleum Engineers Journal*, pages 487–494.

Pákozdi, C. (2008). *A Smoothed Particle Hydrodynamics Study of Two-dimensional Nonlinear Sloshing in Rectangular Tanks*. PhD thesis, Norwegian University of Science and Technology, Trondheim, Norway.

Rafiee, A., Thiagarajan, K. P., and Monaghan, J. J. (2009). SPH Simulation of 2D Sloshing Flow in a Rectangular Tank. In *Proceedings of the 19$^{th}$ International Offshore and Polar Engineering Conference*, Osaka, Japan.

Rakshit, D., Repalle, N., Jagadeesh, P., and Thiagarajan, K. P. (2008). A Numerical Study on the Impact of Filling Level on Liquid Sloshing Pressures. In *Proceedings of the 27$^{th}$ International Conference on Ocean, Offshore and Arctic Engineering*, Estoril, Portugal.

Repalle, N., Pistani, F., and Thiagarajan, K. P. (2010a). Experimental Study of Evolution of Impact Pressure along Vertical Walls of a Sloshing Tank. In *Proceedings of the 20$^{th}$ International Offshore and Polar Engineering Conference*, Beijing, China.

Repalle, N., Truong, T., Thiagarajan, K. P., Roddier, D., Seah, R., and Finnigan, T. (2010b). The Effect of Sampling Rate on the Statistics of Impact Pressure. In *Proceedings of the 29$^{th}$ International Conference on Ocean, Offshore and Arctic Engineering*, Shanghai, China.

Rhee, S. H. (2004). A Validation Study for Tank Sloshing Using a Navier-Stokes Solver. In *Proceedings of the 23$^{rd}$ International Conference on Offshore Mechanics and Arctic Engineering*, Vancouver, Canada.

Rognebakke, O. F. and Faltinsen, O. M. (2001). Effect of Sloshing on Ship Motions. In *Proceedings of the 16$^{th}$ International Workshop on Water Waves and Floating Bodies*, Hiroshima, Japan.

Rognebakke, O. F. and Faltinsen, O. M. (2003). Coupling of Sloshing and Ship Motions. *Journal of Ship Research*, 47(3):208–221.

Sames, P. C., Marcouly, D., and Schellin, T. E. (2002). Sloshing in Rectangular and Cylindrical Tanks. *Journal of Ship Research*, 46(3).

Schreier, S., Godderidge, B., Paschen, M., Turnock, S., Tan, M., and Cowlan, N. (2009). Assessment of Transient Sloshing due to Encounter of an LNG Carrier with a Steep Wave. In *Proceedings of the 28$^{th}$ International Conference on Ocean, Offshore and Arctic Engineering*, Honolulu, USA.

Schreier, S. and Paschen, M. (2008). Sloshing in LNG Tanks – Assessment of High and Low Pressures. In *Proceedings of the 27$^{th}$ International Conference on Ocean, Offshore and Arctic Engineering*, Estoril, Portugal.

SNAME (1989a). *Principles of Naval Architecture*, volume 3 – Motions in Waves and Controllability. The Society of Naval Architects and Marine Engineers.

SNAME (1989b). *Principles of Naval Architecture*, volume 1 – Stability and Strength. The Society of Naval Architects and Marine Engineers.

Thamsen, P. U. and Siekmann, H. (2009). *Strömungslehre für den Maschinenbau*. Springer Verlag Heidelberg.

The California Energy Commission (2012). Liquefied Natural Gas Worldwide Homepage. http://www.energy.ca.gov/lng/international.html.

Thiagarajan, K. P., Rakshit, D., and Repalle, N. (2011). The Air-Water Sloshing Problem: Fundamental Analysis and Parametric Studies on Excitation and Fill Levels. *Journal of Ocean Engineering*, 38(2-3):498–508.

van Oortmerssen, G. (1979). Hydrodynamic Interaction between two Structures. In *Proceedings of the 2$^{nd}$ International Conference on the Behaviour of Offshore Structures*, London, United Kingdom.

WAMIT Inc. (2006). *WAMIT 6.4 User Manual*. The Massachusets Institute of Technology. Userguide.

Wemmehove, R., Luppes, R., Veldman, A., and Bunnik, T. (2007). Application of a VOF Method to Model Compressible Two-Phase Flow in Sloshing Tanks. In *Proceedings of the 27$^{th}$ International Conference on Offshore Mechanics and Arctic Engineering*, Estoril, Portugal.

Wichers, J. E. W. (1979). Some Aspects of Model Tests in Designing Mooring Systems in the Open Sea. In *Proceedings of the 2nd WEGEMT Graduate School*, Wageningen, The Netherlands.

Zalar, M., Diebold, L., Baudin, E., Henry, J., and Chen, X.-B. (2007). Sloshing Effects Accounting for Dynamic Coupling between Vessel and Tank Liquid Motion. In *Proceedings of the 26th International Conference on Ocean, Offshore and Arctic Engineering*, San Diego, USA.

Zalar, M., Malenica, Š., and Diebold, L. (2006). Selected Hydrodynamic Issues in Design of Large LNG Carriers. In *Proceedings of the RINA International Conference on Ship and Offshore Technology*, Busan, South Korea.

# Nomenclature

| | | |
|---|---|---|
| $(2s_{1,a})_{s,tol} \dots (2s_{3,a})_{s,tol}$ | Tolerable significant double amplitudes of translatory motions | $[m]$ |
| $(2s_{1,a})_s \dots (2s_{3,a})_s$ | Significant double amplitudes of translatory motions | $[m]$ |
| $(2s_{4,a})_{s,tol} \dots (2s_{6,a})_{s,tol}$ | Tolerable significant double amplitudes of rotatory motions | $[^\circ]$ |
| $(2s_{4,a})_s \dots (2s_{6,a})_s$ | Significant double amplitudes of rotatory motions | $[^\circ]$ |
| $2(s_{relx,a})_s$ | Significant double amplitudes of relative $x$-motions at specified points | $[m]$ |
| $2(s_{relz,a})_s$ | Significant double amplitudes of relative $z$-motions at specified points | $[m]$ |
| $A_{mean}$ | Mean logarithmic decrement | $[-]$ |
| $A_n$ | $\mathrm{n}^{th}$ Decay motion amplitude | |
| $B$ | Coefficient of the JONSWAP spectrum | $[-]$ |
| $B_T$ | Breadth of the tank | $[m]$ |
| $B_V$ | Breadth of the vessel | $[m]$ |
| $D$ | Characteristic dimension of the structure | $[m]$ |
| $D_T$ | Diameter of the spherical tank | $[m]$ |
| $D_V$ | Draft of the vessel | $[m]$ |
| $D_{eq}$ | Equivalent diameter of mooring line segment | $[m]$ |
| $EA$ | Elasticity of mooring line segment | $[\frac{kg\,m}{s^2}]$ |
| $F$ | Coefficient of the JONSWAP spectrum | $[-]$ |

| | | |
|---|---|---|
| $F_{ex,H}$ | External horizontal load on the mooring line | $[\frac{kg\,m}{s^2}]$ |
| $F_{x0}^{(2)}$, $F_{y0}^{(2)}$ | Mean wave drift force on the moored vessel in $x$- and $y$-direction | $[\frac{kg\,m}{s^2}]$ |
| $G$ | Green's function | $[m^{-1}]$ |
| $H$ | Wave height | $[m]$ |
| $H_{33}$ | Integration limit for the Rayleigh distribution | $[m]$ |
| $H_{RMS}$ | Root mean square of the wave height | $[m]$ |
| $H_T$ | Height of the tank | $[m]$ |
| $H_V$ | Molded depth of the vessel | $[m]$ |
| $H_{max}$ | Maximum wave height | $[m]$ |
| $H_{s,tol}$ | Tolerable significant wave height | $[^\circ]$ |
| $H_s$ | Significant wave height | $[m]$ |
| $I$ | Second moment of area | $[m^4]$ |
| $L$ | Wave length | $[m]$ |
| $L_x, L_y$ | Characteristic vessel length in $x$- and $y$-direction | $[m]$ |
| $L_{OA}$ | Length over all | $[m]$ |
| $L_S$ | Length of mooring line segment | $[m]$ |
| $L_T$ | Length of the tank | $[m]$ |
| $L_{pp}$ | Length between perpendiculars | $[m]$ |
| $P$ | Probability of exceedance | $[-]$ |
| $R$ | Radius of fluid domain | $[m]$ |
| $S$ | Energy density of the sea state | $[m^2\,s]$ |
| $S_1 \ldots S_3$ | Response spectra of translatory body motions | $[m^2 s]$ |
| $S_4 \ldots S_6$ | Response spectra of rotatory body motions | $[rad^2 s]$ |

| | | |
|---|---|---|
| $S_B$ | Surface area of the sea bed | $[m^2]$ |
| $S_F$ | Spectrum of the slowly-varying second-order wave forces | $[\frac{kg^2\,m^2}{s}]$ |
| $S_\infty$ | Surface area of the far field boundary | $[m^2]$ |
| $S_{\tilde{x}}$ | Slowly-varying response spectrum of the vessel motions in irregular seas | $[m^2 s]$ |
| $S_b$ | Surface area of the wetted body | $[m^2]$ |
| $S_f$ | Area of the free water surface | $[m^2]$ |
| $S_{relx}$ | Response spectrum of relative $x$-motions at specified points | $[m^2 s]$ |
| $S_{relz}$ | Response spectrum of relative $z$-motions at specified points | $[m^2 s]$ |
| $T_p$ | Peak period | $[s]$ |
| $T_0$ | Zero-upcrossing period | $[s]$ |
| $T_P$ | Pretension force on the mooring line | $[\frac{kg\,m}{s^2}]$ |
| $V$ | Volume of the fluid domain | $[m^3]$ |
| $V_L$ | Loading capacity of the vessel | $[m^3]$ |
| $V_T$ | Volume of the tank | $[m^3]$ |
| $\Delta$ | Laplace operator | |
| $\Delta\omega$ | Frequency shift | $[\frac{rad}{s}]$ |
| $\Phi$ | Flow potential | $[\frac{m^2}{s}]$ |
| $\Phi_0$ | Velocity potential of the incident wave field | $[\frac{m^2}{s}]$ |
| $\Phi_7$ | Velocity potential of the scattering wave field | $[\frac{m^2}{s}]$ |
| $\Phi_1 \ldots \Phi_3$ | Velocity potentials of the radiation wave fields due to translatory body motions | $[\frac{m^2}{s}]$ |
| $\Phi_4 \ldots \Phi_6$ | Velocity potentials of the radiation wave fields due to rotatory body motions | $[\frac{m^2}{s}]$ |
| $\Phi_R$ | Cumulative Rayleigh distribution function | $[-]$ |

| | | |
|---|---|---|
| $\bar{F}_{x0}^{(2)}$ | Mean wave drift force on the moored vessel in $x$-direction in irregular seas | $[\frac{kg\,m}{s^2}]$ |
| $\bar{x}_0^{(2)}$ | Mean excursion of the moored vessel in $x$-direction | $[m]$ |
| $\beta$ | Incident wave angle | $[^\circ]$ |
| $\underline{\ddot{s}}$ | Vector of body accelerations | |
| $\ddot{s}_1 \dots \ddot{s}_3$ | Translatory body accelerations | $[\frac{m}{s^2}]$ |
| $\ddot{s}_4 \dots \ddot{s}_6$ | Rotatory body accelerations | $[\frac{rad}{s^2}]$ |
| $\delta$ | Damping ratio | $[-]$ |
| $\delta_1$ | Breadth of the bottom chamfer of the tank | $[m]$ |
| $\delta_2$ | Height of the bottom chamfer of the tank | $[m]$ |
| $\delta_3$ | Breadth of the top chamfer of the tank | $[m]$ |
| $\delta_4$ | Height of the top chamfer of the tank | $[m]$ |
| $\underline{\dot{s}}$ | Vector of body velocities | |
| $\dot{s}_1 \dots \dot{s}_3$ | Translatory body velocties | $[\frac{m}{s}]$ |
| $\dot{s}_4 \dots \dot{s}_6$ | Rotatory body velocties | $[\frac{rad}{s}]$ |
| $\forall$ | Displacement of the vessel | $[m^3]$ |
| $\gamma$ | Coefficient of the spectral shape | $[-]$ |
| $\mu$ | Wave frequency for slowly-varying drift forces | $[rad/s]$ |
| $\mu_{0x}$ | Natural frequency of the horizontal motion component of the moored vessel | $[rad/s]$ |
| $\omega$ | Wave frequency | $[\frac{rad}{s}]$ |
| $\omega_p$ | Peak frequency | $[\frac{rad}{s}]$ |
| $\omega_{r,i}$ | Resonance frequency of the i$^{\text{th}}$ mode | $[\frac{rad}{s}]$ |
| $\omega'_{r,i}$ | Corrected resonance frequency of the i$^{\text{th}}$ mode | $[\frac{rad}{s}]$ |
| $\overline{B_0M_0}$ | Initial height of the metacentre above the center of buoyancy | $[m]$ |

| | | |
|---|---|---|
| $\overline{GG'}$ | Shift of the center of gravity | $[m]$ |
| $\overline{GM_0}$ | Initial metacentric height | $[m]$ |
| $\overline{GM_{0corr}}$ | Corrected initial metacentric height | $[m]$ |
| $\overline{GN_{\varphi corr}}$ | Metacentric height for larger inclination angles | $[m]$ |
| $\overline{KB_0}$ | Height of the center of buoyancy above keel | $[m]$ |
| $\overline{KG}$ | Height of the center of gravity above keel | $[m]$ |
| $\overline{M_0N_\varphi}$ | Stability term for larger inclination angles | $[m]$ |
| $\rho$ | Density of the fluid | $[\frac{kg}{m^3}]$ |
| $\rho_T$ | Density of the internal fluid | $[\frac{kg}{m^3}]$ |
| $\sigma$ | Coefficient of the JONSWAP spectrum | $[-]$ |
| $\theta$ | Wave phase angle | $[rad]$ |
| $\tilde{x}_{RMS}$ | Root mean square of the slow-drift surge excursions | $[m]$ |
| $\tilde{x}_{max}$ | Maximum slow-drift surge excursions | $[m]$ |
| $\tilde{x}_s$ | Significant slow-drift surge excursions | $[m]$ |
| $\underline{A}$ | Matrix of added masses | |
| $\underline{A}^*_{ij}$ | Minor of the added mass matrix | |
| $\underline{A}^{-1}$ | Inverse matrix of added masses | |
| $\underline{B}$ | Matrix of potential damping | |
| $\underline{B}_v$ | Matrix of viscous damping | |
| $\underline{C}$ | Vector of restoring coefficients | |
| $\underline{F}_{dyn}$ | Vector of hydrodynamic forces | |
| $\underline{F}_{ex}$ | Vector of excitation forces | |
| $\underline{F}_{int,dyn}$ | Vector of dynamic internal forces | |
| $\underline{F}_{int,stat}$ | Vector of static internal forces | |
| $\underline{F}_{int}$ | Vector of internal forces | |

| | | |
|---|---|---|
| $\underline{M}$ | Matrix of rigid body masses | |
| $\underline{\nabla}$ | Nabla operator | |
| $\underline{\xi}$ | Vector of source location | |
| $\underline{n}$ | Normal vector | |
| $\underline{r}$ | Position vector | |
| $\underline{s}$ | Vector of body motions | |
| $\underline{v}$ | Vector of wave particle velocities | |
| $\varepsilon$ | Phase shift between wave elevation and body motions | $[rad]$ |
| $\varphi$ | Inclination angle of the vessel | $[^\circ]$ |
| $\varphi_1 \dots \varphi_3$ | Local body potentials due to translatory body motions | $[m]$ |
| $\varphi_4 \dots \varphi_6$ | Local body potentials due to rotatory body motions | $[m^2]$ |
| $\varphi_{Hmax}$ | Probability density distribution of the maximum wave height | $[m^{-1}]$ |
| $\varphi_R$ | Rayleigh distribution | $[m^{-1}]$ |
| $\varphi_{dyn}$ | Dynamic capsize angle | $[^\circ]$ |
| $\varphi_{stat}$ | Static capsize angle | $[^\circ]$ |
| $\zeta_{a,TANK}$ | Wave amplitude of the internal fluid | $[m]$ |
| $\zeta_{a,gap}$ | Wave amplitude in the gap between two vessels | $[m]$ |
| $\zeta_a$ | Wave amplitude | $[m]$ |
| $a_S$ | Added mass per meter length of mooring line segment | $[\frac{kg}{m}]$ |
| $a_{ij,T}$ | Added mass coefficients of the internal tank | |
| $a_{ij}$ | Added mass coefficients | |
| $a_{ij}^{-1}$ | Inverse added mass coefficients | |
| $b_{c,ij}$ | Critical damping coefficients | |

| | | |
|---|---|---|
| $b_{ij}$ | Potential damping coefficients | |
| $b_{m,ij}$ | Total damping coefficients | |
| $b_{v,ij}$ | Viscous damping coefficients | |
| $c_{ij,T}$ | Restoring coefficients of the tank | |
| $c_{ij}$ | restoring coefficients | |
| $d$ | Water depth | $[m]$ |
| $f_{ex,1} \dots f_{ex,3}$ | Excitation forces | $[\frac{kg\,m}{s^2}]$ |
| $f_{ex,4} \dots f_{ex,6}$ | Excitation moments | $[\frac{kg\,m^2}{s^2}]$ |
| $f_{int,ij}$ | Internal forces and moments | |
| $f_{int,ij}^{-1}$ | Inverse internal forces and moments | |
| $g$ | Acceleration of gravity | $[\frac{m}{s^s}]$ |
| $h$ | Righting arm of the vessel | $[m]$ |
| $h_f$ | Filling height of the internal fluid | $[m]$ |
| $h_{corr}$ | Corrected righting arm of the vessel | $[m]$ |
| $k$ | Wave number | $[m^{-1}]$ |
| $k_{xx}$ | Stiffness of the mooring system in the horizontal plane | $[\frac{kg}{s^2}]$ |
| $m_S$ | Mass in air per meter length of mooring line segment | $[\frac{kg}{m}]$ |
| $m_{ij}$ | rigid mass coefficients | |
| $n_1 \dots n_3$ | Components of the normal vector | $[-]$ |
| $p_{dyn}$ | Hydrodynamic pressure | $[\frac{kg}{m\,s^2}]$ |
| $r_x, r_y, r_z$ | Distances from the origin of the coordinate system to specified points | $[m]$ |
| $s_1 \dots s_3$ | Translatory body motions | $[m]$ |
| $s_4 \dots s_6$ | Rotatory body motions | $[^\circ]$ |
| $s_\varphi, s_\vartheta, s_\psi$ | Absolute rotatory motions at specified points | $[^\circ]$ |

| | | |
|---|---|---|
| $s_{rel\varphi}, s_{rel\vartheta}, s_{rel\psi}$ | Relative rotatory motions at specified points | $[^\circ]$ |
| $s_{relx}, s_{rely}, s_{relz}$ | Relative translatory motions at specified points | $[m]$ |
| $s_x, s_y, s_z$ | Absolute translatory motions at specified points | $[m]$ |
| $t$ | Time | $[s]$ |
| $u, v, w$ | Wave particle velocities | $[\frac{m}{s}]$ |
| $w$ | Submerged weight per meter length of mooring line segment | $[\frac{kg}{s^2}]$ |
| $x, y, z$ | Cartesian coordinates | $[m]$ |
| $x_b, y_b, z_b$ | Coordinates of the center of buoyancy | $[m]$ |
| $x_g, y_g, z_g$ | Coordinates of the center of gravity | $[m]$ |

# Appendix A

# Input Data for Numerical Calculations

In the following, the relevant input data for all 107 numerical calculation runs is provided together with references to graphs and results presented in the main part of this thesis.

- The input for the calculation runs 1 to 19 with the **detached cuboid tank** is listed in Tab. A.1. Figs. 2.1, 2.2, 3.3 and 3.5 are based on these analyses with 19 discrete filling levels (5% to 95%). Here, the internal fluid density is denoted by $\rho_T$, the absolute and relative filling height from the bottom by $f_h$.

- Fig. 3.6 shows transverse and longitudinal modes of the **detached prismatic tank**. These results are based on runs 20 to 38, listed in Tab. A.2. The description of the input data is in compliance with the descriptions for Tab. A.1.

- Tab. A.3 contains the relevant input data for all **single-body calculations with the FLNG terminal and the LNGC**, respectively. Provided information encompass the density of the surrounding fluid $\rho$, the water depth $d$, the location of the vertical center of gravity $CG_z$ with respect to the origin of the body-fixed coordinate system, the rigid body mass of the vessel ($m$ refers to elements $m_{11}$, $m_{22}$ and $m_{33}$ of the mass matrix), the mass moments of inertia of the vessels (according to the elements of the mass matrix, the moment about the $x$-axis is denoted by $m_{44}$, the moment about the $y$-axis by $m_{55}$ and the $z$-axis related moment by $m_{66}$) with respect to the center of gravity as well as the experimentally determined viscous damping coefficients for the heave ($b_{v,33}$), roll ($b_{v,44}$) and pitch motion ($b_{v,55}$) of the vessel — if available. The damping coefficients for the LNGC with partially filled tanks are based on decay tests with 30% fresh water filling in all

four tanks. Furthermore, the density of the liquid inside the LNGC tanks, $\rho_T$ as well as the filling height inside the tanks is given. Runs 39 to 46 are **single-body calculations with the FLNG terminal** for mooring analysis. Results provided in Figs. 3.45, and 3.46 are based on these runs. The **solid filling condition for the LNGC** is calculated in run 47, with respective results appearing in Fig. 3.7. Input data for the **LNGC and filling height variations from 5% to 95% fresh water** ($\rho_T = 998.2$ kg/m$^3$) in all four tanks is labeled by run nos. 48 to 61. Results from these investigations, especially run no. 53 (standard filling case 30%) constitute the central part of this thesis and appear in Figs. 3.7, 3.10, 3.11, 3.12, 3.13, 3.14, 3.15, 3.16, 3.17, 3.18, 3.19, 3.20, 3.21 and 3.24. Another 19 runs (Nos. 62 to 80) have been conducted in order to investigate the seakeeping behavior of the **LNGC with 19 discrete LNG filling heights** ($\rho_T = 435$ kg/m$^3$). Data obtained from these calculations is presented in Figs. 3.17, 3.18 and 3.19. In the lower part of Tab. A.3, the input data for the **geometrical variation investigation with the LNGC** is provided, denoted by run nos. 81 to 83. The respective RAOs are shown in Fig. 3.23. Finally, run 84 is the exemplary analysis of the **LNGC equipped with four equivolumetric spherical tanks**. The surge and roll motions for this case are shown in Fig. 3.39

- In order to investigate the offloading procedure, a series of **multi-body calculations with the FLNG terminal and the LNGC** have been conducted. The relevant input data for each calculation run is given in Tab. A.4. Apart from the density of the surrounding fluid $\rho$ and the water depth $d$, the distance between the origin of body fixed coordinate systems of the FLNG terminal and LNGC are given in $x$- and $y$-direction. Since the input data for each vessel corresponds to single-body cases already listed in Tab. A.3, a reference to the respective run number is given instead of a repetition of the entire data set. The **approach phase from 100 m to 10 m distance** between the two vessels in tandem configuration has been calculated by run nos. 85 to 87 and results are compiled in Fig. 3.26. In run nos. 88 to 106, the **transfer phase** is investigated by taking into account 19 discrete LNG filling levels inside the tanks of the LNGC in presence of the FLNG terminal in tandem configuration (distance 10 m). Since a four-dimensional data array is obtained from these investigations, two different three-dimensional visualization types for selected cases are chosen, with results provided in Figs. 3.28, 3.29, 3.30 and 3.31. The data from these runs is also the basis for the stochastic procedure and respective results presented in section 3.5. Run 107 finally denotes the input for the exemplary side-by-side case illustrated in Figs. 3.40 and 3.41.

Table A.1: Input data for calculations with one detached cuboid tank

| Run No | $\rho_T$ [kg/m$^3$] | $f_h$ [m] | $f_h$ [%] |
|---|---|---|---|
| 01 | 435 | 1.305 | 05 |
| 02 | 435 | 2.610 | 10 |
| 03 | 435 | 3.915 | 15 |
| 04 | 435 | 5.220 | 20 |
| 05 | 435 | 6.525 | 25 |
| 06 | 435 | 7.830 | 30 |
| 07 | 435 | 9.135 | 35 |
| 08 | 435 | 10.440 | 40 |
| 09 | 435 | 11.745 | 45 |
| 10 | 435 | 13.050 | 50 |
| 11 | 435 | 14.355 | 55 |
| 12 | 435 | 15.660 | 60 |
| 13 | 435 | 16.965 | 65 |
| 14 | 435 | 18.270 | 70 |
| 15 | 435 | 19.575 | 75 |
| 16 | 435 | 20.880 | 80 |
| 17 | 435 | 22.185 | 85 |
| 18 | 435 | 23.490 | 90 |
| 19 | 435 | 24.795 | 95 |

Table A.2: Input data for calculations with one detached rectangular tank

| Run No | $\rho_T$ [kg/m$^3$] | $f_h$ [m] | $f_h$ [%] |
|---|---|---|---|
| 20 | 435 | 1.305 | 05 |
| 21 | 435 | 2.610 | 10 |
| 22 | 435 | 3.915 | 15 |
| 23 | 435 | 5.220 | 20 |
| 24 | 435 | 6.525 | 25 |
| 25 | 435 | 7.830 | 30 |
| 26 | 435 | 9.135 | 35 |
| 27 | 435 | 10.440 | 40 |
| 28 | 435 | 11.745 | 45 |
| 29 | 435 | 13.050 | 50 |
| 30 | 435 | 14.355 | 55 |
| 31 | 435 | 15.660 | 60 |
| 32 | 435 | 16.965 | 65 |
| 33 | 435 | 18.270 | 70 |
| 34 | 435 | 19.575 | 75 |
| 35 | 435 | 20.880 | 80 |
| 36 | 435 | 22.185 | 85 |
| 37 | 435 | 23.490 | 90 |
| 38 | 435 | 24.795 | 95 |

Table A.3: Input data for single-body calculations with the FLNG and LNGC

| Run No | $\rho$ [$\frac{kg}{m^3}$] | $d$ [m] | $CG_z$ [m] | $m$ [kg] | $m_{44}$ [kg m$^2$] | $m_{55}$ [kg m$^2$] | $m_{66}$ [kg m$^2$] | $b_{v,33}$ [$\frac{kg}{s}$] | $b_{v,44}$ [$\frac{kgm^2}{s}$] | $b_{v,55}$ [$\frac{kgm^2}{s}$] | $\rho_T$ [$\frac{kg}{m^3}$] | $f_h$ [m] | $f_h$ [%] |
|---|---|---|---|---|---|---|---|---|---|---|---|---|---|
| 39-46 | 998.2 | 100 | 1.190 | 2.677e08 | 1.306e11 | 1.974e12 | 2.057e12 | — | 2.020e09 | 1.610e11 | — | — | — |
| 47 | 998.2 | 100 | -3.130 | 1.038e08 | 1.719e10 | 5.408e11 | 5.533e11 | — | 1.620e08 | 4.000e10 | — | — | — |
| 48 | 998.2 | 100 | -2.086 | 9.814e07 | 2.054e10 | 5.779e11 | 5.845e11 | -3.524e06 | 5.518e08 | -5.081e10 | 998.2 | 1.305 | 05 |
| 49 | 998.2 | 100 | -2.076 | 9.198e07 | 1.926e10 | 5.416e11 | 5.479e11 | -3.524e06 | 5.518e08 | -5.081e10 | 998.2 | 2.610 | 10 |
| 50 | 998.2 | 100 | -2.056 | 8.533e07 | 1.786e10 | 5.025e11 | 5.082e11 | -3.524e06 | 5.518e08 | -5.081e10 | 998.2 | 3.915 | 15 |
| 51 | 998.2 | 100 | -2.020 | 7.819e07 | 1.637e10 | 4.604e11 | 4.657e11 | -3.524e06 | 5.518e08 | -5.081e10 | 998.2 | 5.220 | 20 |
| 52 | 998.2 | 100 | -1.967 | 7.087e07 | 1.484e10 | 4.173e11 | 4.221e11 | -3.524e06 | 5.518e08 | -5.081e10 | 998.2 | 6.525 | 25 |
| 53 | 998.2 | 100 | -1.891 | 6.358e07 | 1.331e10 | 3.744e11 | 3.787e11 | -3.524e06 | 5.518e08 | -5.081e10 | 998.2 | 7.830 | 30 |
| 54 | 998.2 | 100 | -1.753 | 5.625e07 | 1.177e10 | 3.312e11 | 3.350e11 | -3.524e06 | 5.518e08 | -5.081e10 | 998.2 | 9.135 | 35 |
| 55 | 998.2 | 100 | -1.570 | 4.893e07 | 1.024e10 | 2.882e11 | 2.915e11 | -3.524e06 | 5.518e08 | -5.081e10 | 998.2 | 10.440 | 40 |
| 56 | 998.2 | 100 | -1.326 | 4.162e07 | 8.713e09 | 2.451e11 | 2.479e11 | -3.524e06 | 5.518e08 | -5.081e10 | 998.2 | 11.745 | 45 |
| 57 | 998.2 | 100 | -0.996 | 3.431e07 | 7.182e09 | 2.020e11 | 2.043e11 | -3.524e06 | 5.518e08 | -5.081e10 | 998.2 | 13.050 | 50 |
| 58 | 998.2 | 100 | -0.532 | 2.699e07 | 5.651e09 | 1.590e11 | 1.608e11 | -3.524e06 | 5.518e08 | -5.081e10 | 998.2 | 14.355 | 55 |
| 59 | 998.2 | 100 | 0.165 | 1.968e07 | 4.120e09 | 1.159e11 | 1.172e11 | -3.524e06 | 5.518e08 | -5.081e10 | 998.2 | 15.660 | 60 |
| 60 | 998.2 | 100 | 1.371 | 1.237e07 | 2.589e09 | 7.283e10 | 7.366e10 | -3.524e06 | 5.518e08 | -5.081e10 | 998.2 | 16.965 | 65 |
| 61 | 998.2 | 100 | 4.557 | 5.057e06 | 1.059e09 | 2.978e10 | 3.012e10 | -3.524e06 | 5.518e08 | -5.081e10 | 998.2 | 18.270 | 70 |
| 62 | 998.2 | 100 | -2.558 | 1.014e08 | 2.123e10 | 5.970e11 | 6.039e11 | -3.524e06 | 5.518e08 | -5.081e10 | 435 | 1.305 | 05 |
| 63 | 998.2 | 100 | -2.554 | 9.877e07 | 2.068e10 | 5.816e11 | 5.883e11 | -3.524e06 | 5.518e08 | -5.081e10 | 435 | 2.610 | 10 |
| 64 | 998.2 | 100 | -2.546 | 9.594e07 | 2.008e10 | 5.649e11 | 5.714e11 | -3.524e06 | 5.518e08 | -5.081e10 | 435 | 3.915 | 15 |
| 65 | 998.2 | 100 | -2.533 | 9.290e07 | 1.945e10 | 5.470e11 | 5.533e11 | -3.524e06 | 5.518e08 | -5.081e10 | 435 | 5.220 | 20 |
| 66 | 998.2 | 100 | -2.514 | 8.978e07 | 1.880e10 | 5.287e11 | 5.348e11 | -3.524e06 | 5.518e08 | -5.081e10 | 435 | 6.525 | 25 |
| 67 | 998.2 | 100 | -2.488 | 8.667e07 | 1.814e10 | 5.104e11 | 5.162e11 | -3.524e06 | 5.518e08 | -5.081e10 | 435 | 7.830 | 30 |
| 68 | 998.2 | 100 | -2.456 | 8.356e07 | 1.749e10 | 4.920e11 | 4.977e11 | -3.524e06 | 5.518e08 | -5.081e10 | 435 | 9.135 | 35 |
| 69 | 998.2 | 100 | -2.416 | 8.044e07 | 1.684e10 | 4.737e11 | 4.791e11 | -3.524e06 | 5.518e08 | -5.081e10 | 435 | 10.440 | 40 |
| 70 | 998.2 | 100 | -2.369 | 7.733e07 | 1.619e10 | 4.554e11 | 4.606e11 | -3.524e06 | 5.518e08 | -5.081e10 | 435 | 11.745 | 45 |
| 71 | 998.2 | 100 | -2.313 | 7.421e07 | 1.554e10 | 4.370e11 | 4.420e11 | -3.524e06 | 5.518e08 | -5.081e10 | 435 | 13.050 | 50 |
| 72 | 998.2 | 100 | -2.248 | 7.110e07 | 1.488e10 | 4.187e11 | 4.235e11 | -3.524e06 | 5.518e08 | -5.081e10 | 435 | 14.355 | 55 |
| 73 | 998.2 | 100 | -2.173 | 6.799e07 | 1.423e10 | 4.004e11 | 4.050e11 | -3.524e06 | 5.518e08 | -5.081e10 | 435 | 15.660 | 60 |
| 74 | 998.2 | 100 | -2.087 | 6.487e07 | 1.358e10 | 3.820e11 | 3.864e11 | -3.524e06 | 5.518e08 | -5.081e10 | 435 | 16.965 | 65 |
| 75 | 998.2 | 100 | -1.989 | 6.176e07 | 1.293e10 | 3.637e11 | 3.679e11 | -3.524e06 | 5.518e08 | -5.081e10 | 435 | 18.270 | 70 |
| 76 | 998.2 | 100 | -1.878 | 5.873e07 | 1.230e10 | 3.459e11 | 3.498e11 | -3.524e06 | 5.518e08 | -5.081e10 | 435 | 19.575 | 75 |
| 77 | 998.2 | 100 | -1.753 | 5.583e07 | 1.169e10 | 3.288e11 | 3.326e11 | -3.524e06 | 5.518e08 | -5.081e10 | 435 | 20.880 | 80 |
| 78 | 998.2 | 100 | -1.597 | 5.307e07 | 1.111e10 | 3.125e11 | 3.161e11 | -3.524e06 | 5.518e08 | -5.081e10 | 435 | 22.185 | 85 |
| 79 | 998.2 | 100 | -1.425 | 5.043e07 | 1.056e10 | 2.970e11 | 3.004e11 | -3.524e06 | 5.518e08 | -5.081e10 | 435 | 23.490 | 90 |
| 80 | 998.2 | 100 | -1.234 | 4.793e07 | 1.003e10 | 2.822e11 | 2.855e11 | -3.524e06 | 5.518e08 | -5.081e10 | 435 | 24.795 | 95 |
| 81 | 998.2 | 100 | -1.890 | 6.358e07 | 1.331e10 | 3.744e11 | 3.787e11 | — | — | — | 998.2 | 7.830 | 30 |
| 82 | 998.2 | 100 | -1.890 | 9.949e07 | 1.681e10 | 5.923e11 | 6.067e11 | — | — | — | 998.2 | 7.830 | 30 |
| 83 | 998.2 | 100 | -1.890 | 9.949e07 | 1.681e10 | 5.923e11 | 6.067e11 | — | — | — | 998.2 | 7.830 | 30 |
| 84 | 998.2 | 100 | 0.500 | 8.666e07 | 1.800e10 | 5.700e11 | 5.80e11 | — | 1.620e08 | 4.000e10 | 435 | 12.510 | 30 |

Table A.4: Input data for multi-body calculations with the FLNG and LNGC

| Run No | $\rho$ [kg/m$^3$] | $d$ [m] | $x$-distance [m] | $y$-distance [m] | FLNG terminal data cf. run no. | LNGC data cf. run no. |
|---|---|---|---|---|---|---|
| 85 | 998.2 | 100 | 324.62 | — | 39-46 | 47 |
| 86 | 998.2 | 100 | 364.62 | — | 39-46 | 47 |
| 87 | 998.2 | 100 | 414.62 | — | 39-46 | 47 |
| 88 | 998.2 | 100 | 324.62 | — | 39-46 | 62 |
| 89 | 998.2 | 100 | 324.62 | — | 39-46 | 63 |
| 90 | 998.2 | 100 | 324.62 | — | 39-46 | 64 |
| 91 | 998.2 | 100 | 324.62 | — | 39-46 | 65 |
| 92 | 998.2 | 100 | 324.62 | — | 39-46 | 66 |
| 93 | 998.2 | 100 | 324.62 | — | 39-46 | 67 |
| 94 | 998.2 | 100 | 324.62 | — | 39-46 | 68 |
| 95 | 998.2 | 100 | 324.62 | — | 39-46 | 69 |
| 96 | 998.2 | 100 | 324.62 | — | 39-46 | 70 |
| 97 | 998.2 | 100 | 324.62 | — | 39-46 | 71 |
| 98 | 998.2 | 100 | 324.62 | — | 39-46 | 72 |
| 99 | 998.2 | 100 | 324.62 | — | 39-46 | 73 |
| 100 | 998.2 | 100 | 324.62 | — | 39-46 | 74 |
| 101 | 998.2 | 100 | 324.62 | — | 39-46 | 75 |
| 102 | 998.2 | 100 | 324.62 | — | 39-46 | 76 |
| 103 | 998.2 | 100 | 324.62 | — | 39-46 | 77 |
| 104 | 998.2 | 100 | 324.62 | — | 39-46 | 78 |
| 105 | 998.2 | 100 | 324.62 | — | 39-46 | 79 |
| 106 | 998.2 | 100 | 324.62 | — | 39-46 | 80 |
| 107 | 998.2 | 100 | — | 63.5 | 39-46 | 47 |

# Appendix B

# The Dynamic Magnification Factor

In section 3.3.2, the chain of cause and effects that lead to the occurrence of the frequency shift $\Delta\omega$ is systematically investigated, starting from the equation of motion (Eq. (3.6)). In order to simplify the subsequent analysis steps, the internal force matrix $\underline{F}_{int}$ is introduced:

$$\underline{F}_{int} = -\omega^2 \left(\underline{A} + \underline{M}\right) + i\omega \left(\underline{B} + \underline{B}_v\right) + \underline{C} \tag{B.1}$$

In the following, the relation between the newly introduced internal force and the well-known dynamic amplification factor is shown, exemplarily considering one degree of freedom. Starting from the equation of motion according to Newton's second law

$$\underbrace{(m+a)\,\ddot{s}(t)}_{\text{inertia force}} + \underbrace{b\,\dot{s}(t)}_{\text{damping force}} + \underbrace{c\,s(t)}_{\text{restoring force}} = \underbrace{F_{ex}(t)}_{\text{excitation force}} \tag{B.2}$$

a harmonic ansatz for excitation forces and motions is introduced

$$\begin{aligned} F_{ex}(t) &= f_{ex,a}\, e^{i\omega t} \\ s(t) &= s_a\, e^{i(\omega t+\epsilon)} \\ \dot{s}(t) &= i\omega\, s_a\, e^{i(\omega t+\epsilon)} = i\omega\, s(t) \\ \ddot{s}(t) &= -\omega^2\, s_a\, e^{i(\omega t+\epsilon)} = -\omega^2\, s(t) \end{aligned}$$

and division by $e^{i\omega t}$ eliminates the time dependence, finally leading to

$$s_a\, e^{i\epsilon} \left(-\omega^2 (m+a) + i\omega b + c\right) = f_{ex,a} \tag{B.3}$$

This expression is equivalent to the matrix formulation in Eq. (3.6), where the term inside the parentheses is referred to as internal force (Note, that

due to its units [N/m], the internal force is only a formal force, but not a force from a physical point of view.). Rearranging Eq. (B.3) and factoring out the restoring coefficient $c$ leads to

$$s_a\, e^{i\epsilon} = \frac{f_{ex,a}}{c}\, \frac{1}{1 - \omega^2\, \frac{m+a}{c} + i\omega \frac{b}{c}} \tag{B.4}$$

By substituting

$$\begin{aligned} \omega_r &= \sqrt{\frac{c}{m+a}} \\ b &= 2\delta(m+a)\omega_r \\ \Omega &= \frac{\omega}{\omega_r} \end{aligned}$$

finally the expression

$$s_a\, e^{i\epsilon} = \frac{f_{ex,a}}{c}\, \underbrace{\frac{1}{1 - \Omega^2 + i2\delta\Omega}}_{=V(\Omega,\delta)} = \frac{f_{ex,a}}{c}\, V(\Omega, \delta) \tag{B.5}$$

is obtained, defining the dynamic amplification factor $V(\Omega, \delta)$, which exclusively contains system parameters. The dynamic amplification factor can be transferred into the internal force by multiplication by the restoring coefficient $c$. Division of Eq. (B.5) by the wave amplitude $\zeta_a$ gives the complex response amplitude operator:

$$H(\omega) = \frac{s_a}{\zeta_a}\, e^{i\epsilon} = \frac{f_{ex,a}}{c\,\zeta_a}\, V(\Omega, \delta) \tag{B.6}$$